

1-1-2010

Beyond The Dvh - Spatial And Biological Radiotherapy Treatment Planning

Bo Zhao
Wayne State University

Follow this and additional works at: http://digitalcommons.wayne.edu/oa_dissertations



Part of the [Medical Biophysics Commons](#)

Recommended Citation

Zhao, Bo, "Beyond The Dvh - Spatial And Biological Radiotherapy Treatment Planning" (2010). *Wayne State University Dissertations*. Paper 39.

This Open Access Dissertation is brought to you for free and open access by DigitalCommons@WayneState. It has been accepted for inclusion in Wayne State University Dissertations by an authorized administrator of DigitalCommons@WayneState.

**BEYOND THE DVH
--- SPATIAL AND BIOLOGICAL
RADIOTHERAPY TREATMENT PLANNING**

by

BO ZHAO

DISSERTATION

Submitted to the Graduate School

of Wayne State University,

Detroit, Michigan

in partial fulfillment of the requirements

for the degree of

DOCTOR OF PHILOSOPHY

2010

MAJOR: MEDICAL PHYSICS

Advisor

Date

Co-Advisor

Date

ACKNOWLEDGMENTS

First and foremost I give my sincerest gratitude to my advisors Dr. Jay Burmeister and Dr. Michael C. Joiner for their excellent guidance on the research work and their persistent efforts in improving my abilities to work in academia. English language skills have been a barrier for me in writing manuscripts, conference proceedings and this thesis, but they have been patient and were always available. I find it valuable that they guided me, yet allowed me to work independently instead of specifically guiding each step of the project. I appreciate all the opportunities they brought to me which also have prepared me for my future career, such as national and international professional conferences, vendor research symposi, and local presentation opportunities.

I would also like to thank my dissertation committee members Dr. Colin Orton, Dr. Neb Duric and Dr. Howard Thames, without whom I wouldn't have been able to reach this point. Their comments and critiques have improved my manuscripts and they provided me with valuable suggestions on the software development.

In my daily work I have been blessed with a friendly and cheerful group of people. I thank Dr. Yimei Huang and Dr. Yixiang Liao for their pioneering work which helped facilitate this project. Mr. Yingjian Yu who has strong experience in Matlab programming gave lots of support in the beginning of this project. I had lots of discussions with Mr. Qiang Liu who helped me with the software algorithms. I own thanks to the instructors in the Medical Physics Graduate Program who provided excellent training in Medical Physics and all the physics staffs at the Karmanos Cancer Center who are always willing to help and answer my questions.

I received financial support from Wayne State University Graduate School in the first three years and later was supported by Varian Medical Systems (Palo Alto, CA) through the research grant “Biological Plan Evaluation and Optimization Tools for the Eclipse TPS” (Wayne State University SPA#: 420822; PI: Jay Burmeister).

Finally, I thank my wife Dongshu for her perpetual support during the past five years. She has been glad to listen to me talking about my work and amazingly she very often gives me inspirations.

TABLE OF CONTENTS

ACKNOWLEDGMENTS.....	ii
LIST OF FIGURES.....	vi
CHAPTER 1 Basics of Radiotherapy	1
1.1 Introduction	1
1.2 Development of Treatment Planning and Delivery.....	2
1.3 Limitations of Current Treatment Planning Systems.....	11
CHAPTER 2 Methods and Modeling.....	22
2.1 Retaining Spatial Information.....	22
2.1.1 Dose Convolution Filter	22
2.1.2 Spatial DVH.....	27
2.2 Biological Modeling.....	28
2.2.1 Fractionation sensitivity	28
2.2.2 Low-dose HyperRadioSensitivity (HRS)	31
2.2.3 Generalized Equivalent Uniform Dose (gEUD).....	33
2.2.4 Tumor Control Probability (TCP)	34
2.2.5 Normal Tissue Complication Probability (NTCP)	35
2.2.6 Complication-free Tumor Control Probability (P+)	37
2.3 SABER models	38
2.4 Work flow	39
2.5 Research materials	41
CHAPTER 3 SABER Software Demonstration	42
3.1 SABER Software Demonstration	42
CHAPTER 4 Discussion and Conclusions	61

CHAPTER 5 Future Work - Technology versus Biology	73
5.1 Dose distribution capability	74
5.2 Delivery mechanism	76
5.3 Reliability of Technology	77
5.4 Technology versus Biology	78
5.5 Future Work	82
5.5.1 LQ-L; LQC	83
5.5.2 Time parameter	85
5.5.3 Validation of Models with Clinical Data	86
5.5.4 Spatial and Biological Optimization	87
APPENDIX Introduction to DICOM RT	89
a) DICOM RT Dose	89
b) DICOM RT Structure Set	91
c) DICOM RT Plan	93
REFERENCES	94
ABSTRACT	112
AUTOBIOGRAPHICAL STATEMENT	114

LIST OF FIGURES

Figure 1: Illustration of relative locations of structures that are relevant in a prostate cancer radiotherapy treatment. Red structure: target which includes prostate, possible sub-clinical disease extensions and necessary margins; yellow structure: bladder; Brown structure: rectum; white structures: femoral heads. Field 1 and Field 2 are two beams that completely avoid the normal structures.	3
Figure 2: Illustration of relative locations of structures that are relevant in a prostate cancer radiotherapy treatment. Red structure: target which includes prostate, possible sub-clinical disease extensions and necessary margins; yellow structure: bladder; Brown structure: rectum; white structures: femoral heads. Field A and Field B are two probable beams that can enclose the target volume.	4
Figure 3: Illustration of intensity modulation.	5
Figure 4: Optimization screenshot in Eclipse treatment planning system. Planner defines a set of constraints for relevant structures.	7
Figure 5: Multi-leaf collimator (MLC). Top: a simple illustration. Bottom: MLC in a Varian linear accelerator.	8
Figure 6: Dose Volume Histograms (DVH) in Eclipse treatment planning system.	13
Figure 7: Radiosensitivity varies between different cell lines (Ref. 44).	15
Figure 8: Rat spinal cord showed strong volume effect (Ref. 45)	16
Figure 9: Rat spinal cord response curve shifts in the <i>split-field irradiation</i> experiment reported by H.P. Bijl <i>et al</i> (Ref. 27).	16
Figure 10: Increased radioresistance from A to B induced by hypoxia (Ref. 44).	17
Figure 11: one dimensional continuous Gaussian filter	23
Figure 12: An 8x10 matrix convolves with 2D 3x3 Gaussian filters	25
Figure 13: Effect of the filter parameters (size and σ).	26
Figure 14: The sDVH concept and a typical result.	27
Figure 15: Isoeffects of different fractionation schemes for a variety of normal tissues (Ref. 44).	28
Figure 16: Linear-quadratic (LQ) model (Ref. 44).	30

Figure 17: HRS experimental data (asynchronous T98G human glioma cells) fitted with LQ model and IR model (Ref. 76). The parameter α_r is the same as the linear component factor in the LQ model.	32
Figure 18: The character of the parameter a in gEUD calculation.	34
Figure 19: Tumor control probability (TCP, green line), normal tissue complication probability (NTCP, red line) and complication-free tumor control (P+, blue line).	37
Figure 20: SABER software main graphical user interface. On the left are the function panels. The four figures as shown are: top left isodose lines; top right, iso-EQD2 lines; bottom left: cumulative DVHs; bottom right: cumulative eqDVH (DVH normalized to 2Gy fractions). The dotted lines represent the DCF-fitted DVHs. The vertical dashed line is the prescription dose (on DVH figure) or prescription dose normalized to 2Gy fractions (on eqDVH figure).	42
Figure 21: SABER main graphical user interface. Colorwash dose map and differential DVH are displayed.	44
Figure 22: SABER main graphical user interface. Isodose lines in absolute values.	45
Figure 23: Window for changing α/β values.	45
Figure 24: Select/change isodose levels to display	46
Figure 25: SABER main graphical user interface. The four figures are on white background which is more suitable for printouts.	47
Figure 26: Typical sDVH. Top: differential sDVH; bottom: cumulative sDVH.	50
Figure 27: Typical sDVH. Top: differential sDVH; bottom: cumulative sDVH.	51
Figure 28: Excel BioEval function demonstration. The Excel workbook is created in several second by the SABER software. All equations are programmed by SABER. For example, the α/β value for spinal cord was changed from 5 to 3. All results were instantly updated.	52
Figure 29: SABER's "Biological Evaluation" module. The screenshots shown here are just three examples of different combinations of existing TCP and NTCP models.	53
Figure 30: Parameter input window for low dose hypersensitivity (HRS) using the IR model, which replaces the LQ model for converting physical dose to EQD ₂	54
Figure 31: Example of using the dose profile function. The profile can be measured from a physical dose colorwash figure or an EQD2 colorwash figure.	55

- Figure 32: Window for changing DCF preference – isotropic DCF or anisotropic DCF. User is able to define/change filter size and σ value.....56
- Figure 33: Multi-variable TCP figures. Color scale represents TCP values. A) Logistic TCP as a function of D_{50} and α/β for a 2Gy/fraction treatment. TCP values do not change with respect to α/β values. B) Logistic TCP as a function of D_{50} and α/β for a hypo-fractionated treatment ($>2\text{Gy/fraction}$). C) Poisson TCP as a function of SF2 and α/β for the same treatment as in B. D) Voxel-by-voxel Poisson TCP as a function of SF2 and α/β for the same treatment as in B.57
- Figure 34: Multi-variable NTCP figures. Color scale represents NTCP values. A) Logistic NTCP as a function of D_{50} and α/β . B) LKB NTCP as a function of D_{50} and n . C) LKB NTCP as a function of D_{50} and α/β . D) relative seriality NTCP as a function of D_{50} and s . E) relative seriality NTCP as a function of D_{50} and α/β . All figures are generated from one hypo-fractionated prostate treatment plan.....58
- Figure 35: Multi-variable P+ figures. Color scale represents P+ values. As shown are examples of P+ as a result of A) Logistic NTCP (α/β) and logistic TCP (α/β); B) Logistic NTCP (α/β) and Poisson TCP (α/β); C) LKB NTCP (n) and logistic TCP (α/β); D) LKB NTCP (n) and Poisson TCP (α/β); E) relative seriality NTCP (α/β) and voxel-by-voxel Poisson TCP (α/β); F) relative seriality NTCP (s) and voxel-by-voxel Poisson TCP (α/β).....59
- Figure 36: "Bio Plan Comparion" module. By default, only SABER Model 3 is selected for simplicity. Absolute NTCP, TCP and P+ values for the base plan are provided at the bottom.60
- Figure 37: Illustration of DCF effect on different static dose distributions. The dotted white boxes are the target contours. Inside the contour, dose is 100% except the under-dosed regions. Outside, dose is 50%. The σ is chosen as one pixel. (a) Volume effect: cold spots have same level of dose but different volume (b) Dose level effect: cold spots have same volume but different level of dose. DCF could lower a target's gEUD if the dose falls sharply at the edges of the target.68
- Figure 38: Illustration of DCF effect on static dose. Top: on the left are static doses with the same DVH but different spatial dose distribution; on the right are DCF filtered dose distributions. Bottom: DVHs of the original dose distribution and the filtered dose distributions.....69
- Figure 39: Two treatment plans from a prostate case. Top: DVHs. Two treatment plans have virtually identical target DVHs and very close OAR DVHs. Bottom: Dose distribution comparison.....70
- Figure 40: The sDVH for the two prostate treatment plans (Figure 39). Top: differential sDVH and cumulative sDVH for Plan 3. Bottom: differential sDVH and cumulative sDVH for Plan 4.71

Figure 41: “Bio Plan Comparison module”: Top: DCF is OFF; bottom: DCF is ON. All three SABER models are selected. Base values in each SABER model are the absolute NTCP/TCP/P+ values of the first plan, i.e. the “UWHypo” as in this example. In this example, the plan rankings based on NTCP are different from the three models, and application of DCF also alters the plan rankings.	72
Figure 42: Experimental data showing that the LQ model over-estimates the cell survival at higher doses (Ref. 127).	83
Figure 43: Linear-quadratic (LQ) versus linear-quadratic-cubic (LQC) model (Ref. 44). ..	84
Figure 44: Architecture of DICOM RT dose grid.	90
Figure 45: DICOM RT structure set contours.	92

CHAPTER 1

Basics of Radiotherapy

1.1 Introduction

Radiotherapy is a type of cancer treatment that uses ionizing radiation to control malignant cells for either curative or palliative purpose. The root of radiotherapy can be traced back to more than 100 years ago shortly after x-ray was discovered. In the first few decades radioactive isotopes were used as the source of radiation in radiotherapy. The limitation of using radioactive isotopes is that the energy is too low and thus the depth of penetration is shallow.¹ In order to treat deep tumors without surgery, source of high energy x-rays became a demand. In the 1950s, the first megavoltage medical linear accelerator was build at Stanford University which opened the new era of radiotherapy.² Over the past half century, multiple technologic revolutions in radiotherapy have resulted in better treatment outcomes and fewer side effects. In 2000, one in every two cured cancer patient are treated or partially treated with radiotherapy.² Radiotherapy has become one of the most effective and widely used methods for cancer treatment.

In modern radiotherapy, the process starts from computerized tomography (CT) simulation, where volumetric CT data of the patient is acquired. Magnetic resonance images (MRI) are also commonly used, especially for brain tumors. Based on the images, commercial treatment planning system (TPS) is used to create a radiotherapy treatment plan. Once the plan is approved and verified, the radiotherapy treatment of the patient can be initiated. The total prescription dose is usually divided into many fractions and the patient normally gets one fraction per day, so the entire treatment course may take weeks.

Two primary components of radiotherapy are planning and delivery. If a plan can achieve very good tumor coverage and spare normal organs, but the delivery system is unable to deliver the plan to patient, the beautiful plan becomes useless. On the other hand, if the delivery system is very robust but the TPS is very limited and unable to generate an acceptable plan, the robust delivery system is a waste. Thus the development of both planning systems and delivery systems is of paramount importance and the development of both systems is often intertwined.

1.2 Development of Treatment Planning and Delivery

Since radiation can damage both malignant cells in tumors and also normal tissue cells, careful treatment planning and appropriate treatment techniques are required to minimize damage to normal tissue while eradicating tumor cells. Before the era of three dimensional conformal radiotherapy, two dimensional x-ray images were used to align radiation beams to the target. The precision of treatment was relatively poor due to the fact that the target shape was not fully visualized. Because the planning was based on our guess of the target shape, large margins had to be added to assure that the entire tumor was in the radiation field, and therefore significant doses were delivered to normal tissues. In order to prevent significant complications, the prescription dose was limited.

After the invention of 3D imaging such as CT and MRI, 3D digitally reconstructed radiographs were introduced into the radiotherapy treatment planning process. These digitally reconstructed radiographs are obtained in the form of closed spaced transverse images and can be processed to reconstruct anatomy in any plane. Thus the most significant improvement over 2D planning was that any structure could be reconstructed and viewed in any direction. Radiation beams could then be shaped at selectable angles

using beam eye's view such that the tumors received radiation dose and organs-at-risk (OAR) are spared. This is called 3D conformal radiotherapy (3D CRT). Because we can see the shape of the target, the margins can be reduced. Compared to 2D planning, 3D CRT is much more precise and generally reduces radiation dose to critical organs that surround the target.

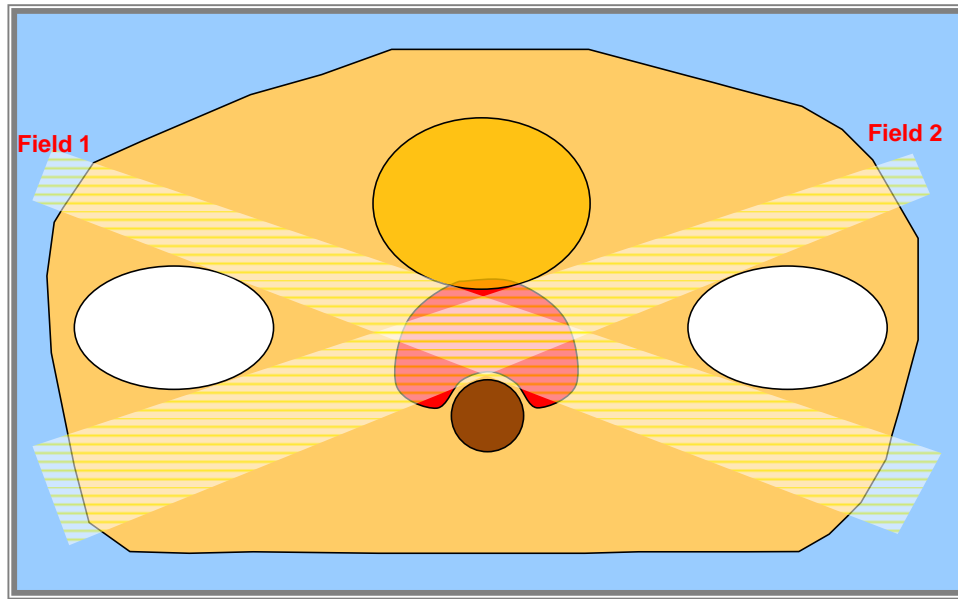


Figure 1: Illustration of relative locations of structures that are relevant in a prostate cancer radiotherapy treatment. Red structure: target which includes prostate, possible sub-clinical disease extensions and necessary margins; yellow structure: bladder; Brown structure: rectum; white structures: femoral heads. Field 1 and Field 2 are two beams that completely avoid the normal structures.

Although digitally reconstructed radiographs allow us to view anatomy in any plane and at any angle, there are still obstacles that prevent us from limiting dose to critical organs or increasing dose to target structures. Take prostate cancer treatment for example. The organ contours and their relative locations are illustrated in Figure 1. Field 1 and Field 2 are two possible beam directions that avoid normal organs. As shown in the figure, it is impossible to deliver radiation dose to the entire target without irradiating normal organs.

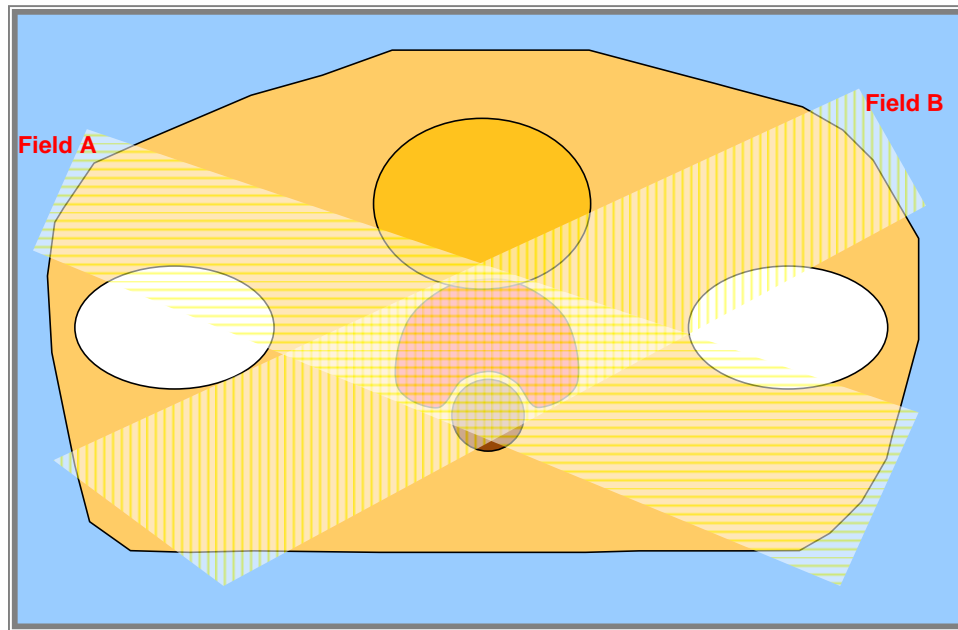


Figure 2: Illustration of relative locations of structures that are relevant in a prostate cancer radiotherapy treatment. Red structure: target which includes prostate, possible sub-clinical disease extensions and necessary margins; yellow structure: bladder; Brown structure: rectum; white structures: femoral heads. Field A and Field B are two probable beams that can enclose the target volume.

So we have to pass radiation beams through normal organs (Figure 2). But we must ensure that the doses to normal organs are minimized and below their tolerance so that the treatment won't cause significant normal tissue complication. In 3D CRT, radiation fields that are aligned to the shape of target are open during the treatment. The output (intensity) from the linear accelerator is roughly constant across the field. If we neglect attenuation differences inside the patient's body, the dose to the normal organs would be the same as the dose to the target that sits at the same depth. In this prostate case, significant doses would be delivered to rectum. In order to reduce the dose to rectum, one can reduce the radiation intensity in the portion of the field where the rectum sits. The intensity from another field can then be increased in this region to compensate for this reduction in dose from the first field. This leads to the concept of intensity modulation and Intensity-

Modulated Radiotherapy (IMRT). Figure 3 is a simple sketch that illustrates such intensity modulation. In real radiotherapy planning, the modulation is much more complex because of numerous dose-volume constraints for multiple structures.

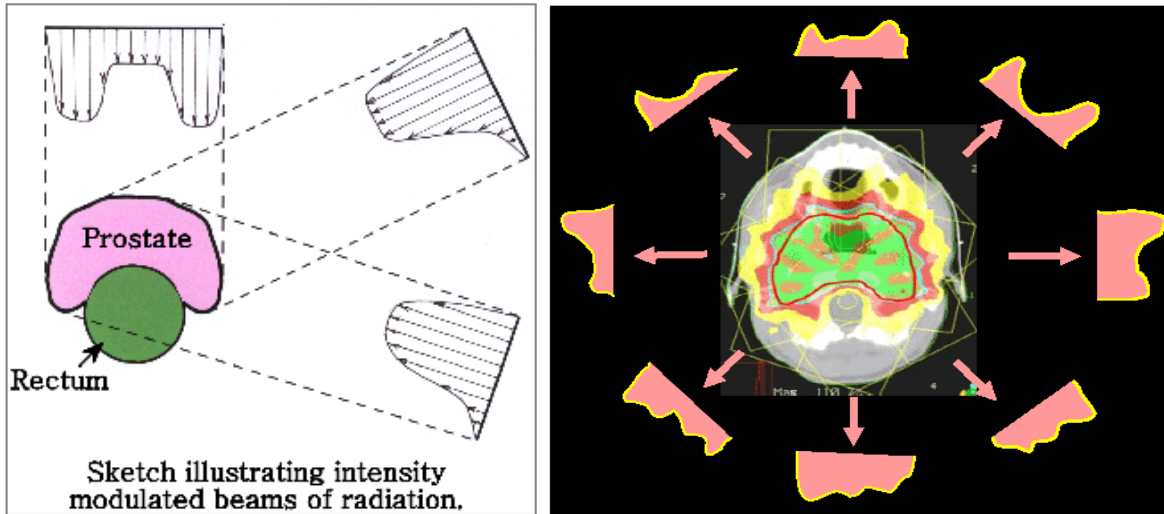


Figure 3: Illustration of intensity modulation.

IMRT is a major technologic development over conventional radiotherapy. It is arguably the most important revolution in radiation oncology. The first use of IMRT appeared in the beginning of 1990s and it became popular from the mid 1990s. The implementation of IMRT delivery techniques has resulted in significant reduction in absorbed dose to OARs compared to 3D CRT ³⁻⁶, and this leads to lower normal tissue complication probability (NTCP).⁷⁻¹⁰ Alternatively, this increased conformity can be exploited by escalating the dose to the target to achieve higher tumor control probability (TCP) while maintaining OAR doses below their tolerance.¹¹⁻¹³ It should also be noted that changes in the delivery technique can significantly change the absorbed dose throughout the patient, and not just in the vicinity of the target structure(s). For example, in the study

reported by D.B. Mansur *et al*¹⁴, the authors found that compared to 3D CRT, IMRT treatment resulted in lower peripheral dose in regions closer to the target. However, at distant points, IMRT deposited more dose than 3D CRT presumably due to IMRT's higher monitor units and increased head leakage.

One of the most important components commonly employed for IMRT is the inverse planning system. Conventionally in forward planning, one would subjectively define or design the direction and the number of fields, the shape of each field, the margins that need to add to target, the relative weighting of the fields, the use of wedges or compensators, etc. After dose calculation, the user then evaluates the planning results and decides what changes are needed in order to achieve the desired planning goals. It is an iterative process performed until the planning results are satisfactory. In inverse planning systems, the planner defines the number and the angles of the fields and then starts from the planning goals. For each structure, a set of constraints are defined. These constraints limit the dose levels to certain percentages of the structure volume (Figure 4). Then the computerized optimizer will find a solution that satisfies the constraints (planning goals) to the maximum extent possible. Each field can be viewed as consisting of many beamlets. Intensity modulation is achieved by varying the individual intensities of each beamlet. The Multi-Leaf Collimator (MLC) is a device commonly used for shaping radiation fields and is most often the method used to modulate the beamlet intensities during delivery of IMRT (Figure 5).

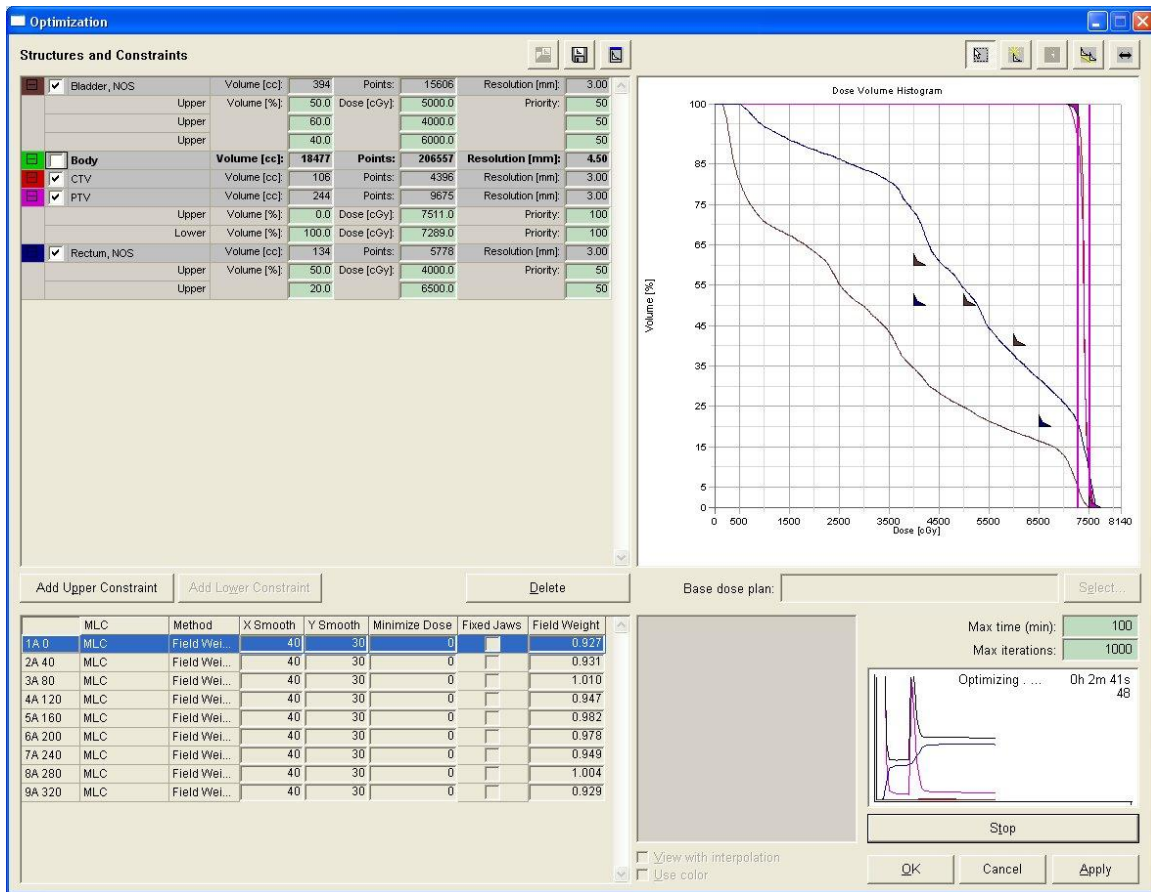


Figure 4: Optimization screenshot in Eclipse treatment planning system. Planner defines a set of constraints for relevant structures.

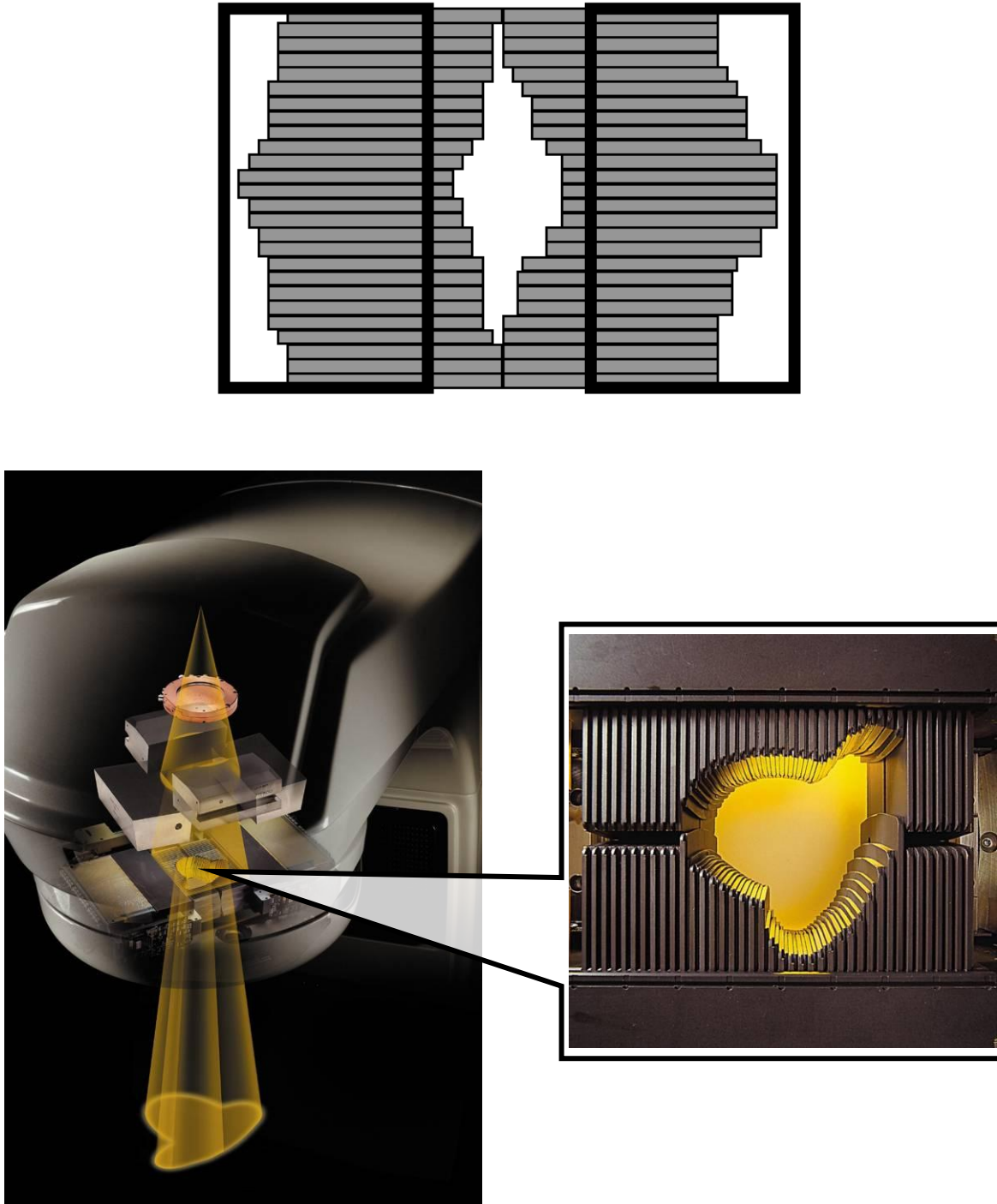


Figure 5: Multi-leaf collimator (MLC). Top: a simple illustration. Bottom: MLC in a Varian linear accelerator.

As mentioned earlier, development of technologies results in lower dose to critical organs, smaller margins added to tumor site, and dose escalation to target. All these advancements require that the dose be accurately delivered to the right location. In radiotherapy, the prescription dose is usually delivered in multiple days with the exception of stereotactic radiosurgery in which the dose is delivered in one fraction. Each treatment is called one fraction. The entire treatment course may take up to 8 or 9 weeks. If the setup is perfect everyday and the structures and/or cells do not migrate, the job of predicting the effect of radiation dose would be easier. However, those are not true. Not only is the day-to-day setup not perfect, but also the organs move during a fraction (intra-fraction motion) and in between fractions (inter-fraction motion).¹⁵⁻¹⁹ In the work by B. Kihlbn *et al*¹⁵, treatment variations were studied for various cancer sites. Notable errors of 9mm were found for esophagus, followed by 7mm for breast and ovaries. Prostate is also an organ that is known to move around and could displace by over 10mm.²⁰⁻²¹ In lung tumor treatment, respiratory motion is usually an issue that needs to be taken into account during planning.²²⁻²³ All these facts suggest that we need to track the inter-fraction and intra-fraction movements of organs during the delivery of radiation. This led to the development of Image-Guided Radiotherapy (IGRT).

IGRT enables us to see the location of the target or organs right before the treatment or during the treatment, which prevents large deviations in the planned dose. Better image guidance technology allows clinicians to potentially reduce PTV margins which then provides increased latitude within which to capitalize on the more conformal dose distributions offered by more sophisticated delivery techniques. However, reduced margins result in the potential hazard of a geographical miss if the capabilities of image

guidance and immobilization are overestimated.²⁴ In such cases, the target dose may be significantly reduced which may also be accompanied by a significant increase in OAR doses.

In addition, IGRT techniques involving ionizing radiation introduce additional patient dose from the imaging technique prior, during, or after treatment.²⁵ The additional dose introduced is typically at the order of a few centi-grays (cGy) for one fraction of treatment. Compared to the therapeutic dose which is on the order of a few grays (Gy) (1Gy = 100cGy), this is a very small amount and the effect is usually neglected. But since the entire treatment course could be composed of more than 40 fractions, the total imaging dose could become significant in comparison to the therapeutic fraction dose if daily imaging guidance employed.²⁵ Several studies have shown that the administration of low doses prior to radiation therapy may result in a detrimental effect by accelerating tumor cell proliferation and increasing tumor radioresistance.²⁵⁻²⁶ Furthermore, an experiment by H.P. Bijl *et al*²⁷ showed unexpected organ tolerance dose changes due to a low background bath dose, providing an additional indication that relatively small imaging doses before or during treatment might have deleterious effects to normal tissues. So the dose introduced by IGRT might bring double-trouble to radiotherapy treatment: 1) it may increase the tumor's resistance to radiation, and 2) it may decrease the normal tissue's tolerance to radiation. Therefore, when administering ionizing radiation for image guidance, the biological effect of the imaging dose needs to be considered and investigated.

Another fact that limits the precision of depositing dose to a designated location is that cells could migrate. The study by R. Franklin *et al* reported a 2mm migration of remyelinating cells.²⁸ Such a 2mm movement could be extremely important for

stereotactic radiosurgery which aims at achieving sub-millimeter accuracy.²⁹⁻³¹ This distance is also comparable to the reported accuracy of modern IGRT techniques.³²⁻³³ The effect of cell migration is an effective smearing of dose distributions. The effects of this smearing has been presented by Y. Huang *et al.*³⁴ In some important aspects, we are approaching the physical limits of our ability to make radiotherapy dose distributions more conformal. We must also begin to consider the biological effects of new radiotherapy technologies and the associated uncertainties in these biological effects as these may become significant and could potentially offset some gains made by physical and technical advantages.

1.3 Limitations of Current Treatment Planning Systems

Inverse planning systems were developed to optimize and evaluate treatment plans based on physical dose-volume constraints. Before this work was started, the only commercial treatment planning system that incorporated some biological information in the optimization process was the P³IMRT[®] TPS by Philips. In this system, plan optimization is performed using generalized equivalent uniform dose (gEUD, will be discussed later) constraints and objective functions originally derived for the ORBIT[®] system.³⁵ Eclipse (Varian Medical Systems, Inc.) is another commonly used treatment planning system. For convenience, this work has been developed and tested with the Eclipse system since this system is available in our department. But the application of this work is not limited to the Eclipse system.

The optimization in the Eclipse system is done inversely by selecting a limited set of dose-volume constraints input by the treatment planner as show in Figure 4. The planner chooses appropriate upper and lower limits for different structures and set

preferred priorities and other parameters. Then the Eclipse TPS tries to calculate an optimum plan that satisfies the planner's objectives. The fact is that the solution to the optimization objective function is not unique and the final plan created by the planning system is just a single possibility from a tremendously large set of possible solutions. The question remains as to what makes this the "optimum" plan for this patient and what information is utilized in making such a decision. Treatment plans are evaluated mainly based on dose-volume histograms (DVHs) (Figure 6). Ideally, a perfect plan would deliver the full prescription dose to the planning target volume (PTV) and no dose to the OARs. That is, as shown in Figure 6, to push the PTV curve (the purple line) to the upper right corner and the OAR curves (blue, brown and green lines) to the lower left corner as much as possible.

The term "optimization" is in fact inappropriate for the current state of inverse-planned IMRT, as it implies both that we know what the optimum plan is, and that we are actually capable of achieving that plan.³⁶ A treatment plan should not be characterized as "optimized" as a result of the minimization of an objective function using a limited set of parameters input by the treatment planner. This is particularly true if these objectives are based solely on physical dose. The vast majority of IMRT treatment plans currently delivered to patients (and termed "optimized") takes only physical dose information into account. Not considering biological information clearly prohibits any effort to create truly "optimized" plans in terms of patient outcome.

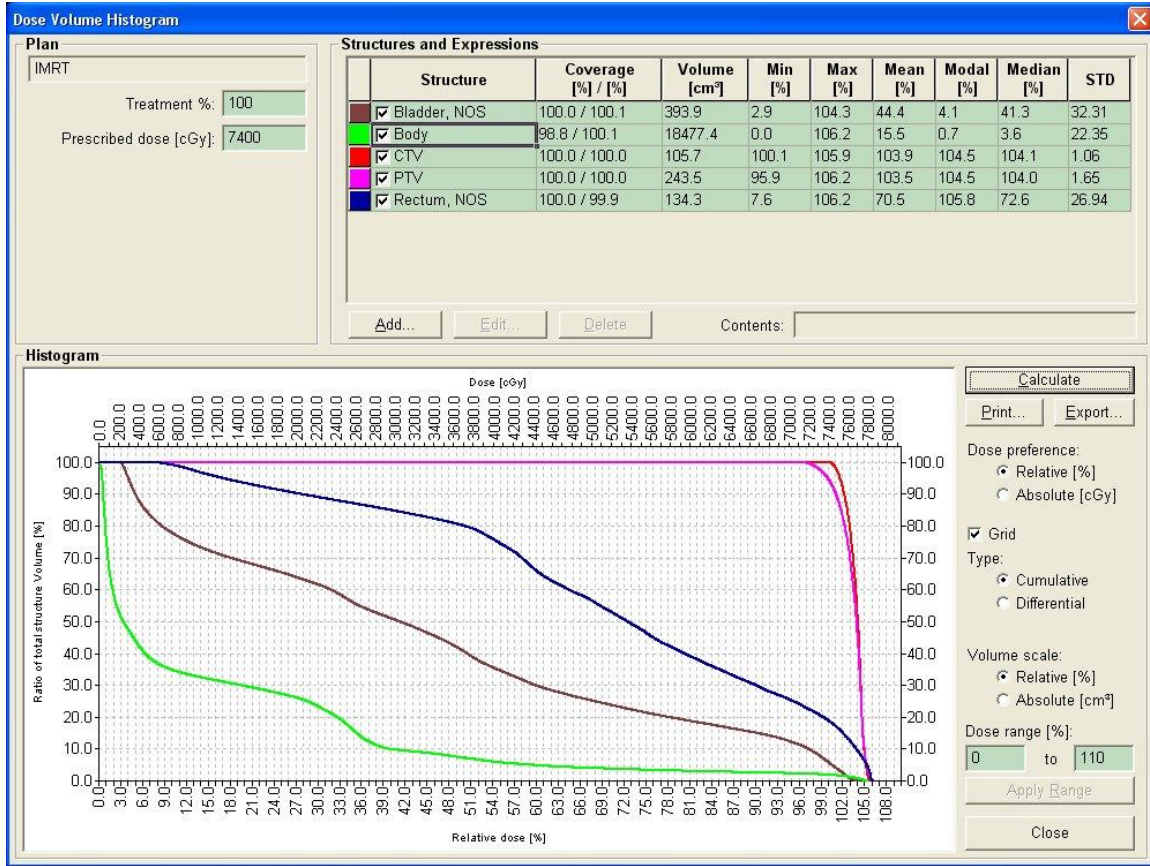


Figure 6: Dose Volume Histograms (DVH) in Eclipse treatment planning system.

Treatment plans in Eclipse are currently evaluated based on DVHs, which essentially eliminates all spatial information associated with the dose distribution. In IMRT planning, as plan complexity increases, the dose heterogeneity can be significant. Thus the spatial dose distribution inside a structure becomes important, especially when "cold" spots (under-dosed regions) or "hot" spots (over-dosed regions) are present.³⁷⁻³⁹ The DVH provides simple dose volume coverage information in a single plot and is widely used as an indicator of plan quality.⁴⁰⁻⁴¹ However, IMRT optimization based on aspects of the DVH does not tell the planning system where in a given structure to allow or prevent the "cold" or "hot" spots. Thus, if significant "cold" spots are located in the center of the gross disease, a plan with sharper fall-off in the target DVH might not be better than a plan

with shallower fall-off DVH. Similarly, different distributions of “hot” spots may also lead to different outcomes.³⁹ As a result, the clinician still must review the 3D dose distribution during the plan evaluation process since the DVH contains no spatial information.

The 3D dose distribution information can only be viewed in one 2D plane at a time making it more difficult for the observer to objectively quantify plan quality. Moreover, it is only a static snapshot of what the delivered plan would look like on the CT data acquired at the time of simulation. However, in a real radiotherapy treatment process, the presence of setup uncertainties⁴², interfraction and intrafraction motion²¹, and underlying cell migration⁴³ will mean that the dose to any individual component of tissue in the patient will differ from the static dose observed in the treatment planning system. Ideally, the effects of these should be included in the plan evaluation process prior to selecting the desired treatment plan and attempting to estimate its effects.

Furthermore, fractionation sensitivity (quantified by the α/β ratio) varies among cells from site to site and/or from patient to patient.⁴⁴ Therefore, not only will the static dose distribution viewed within the treatment planning system differs from the absorbed dose distribution received by the patient throughout the course of radiotherapy, but the physical dose distribution may not be the best representation of the plan quality since it does not contain any of the biological information which is important in determining the outcome of treatment. Biological parameters need to be included when evaluating or optimizing a radiotherapy plan. Cells may react to radiation differently (Figure 7).⁴⁴ In other words, a physical dose of 2Gy would not cause the same level of cell killing for different cells or organs. An effective or equivalent dose that takes the sensitivity into account is desirable.

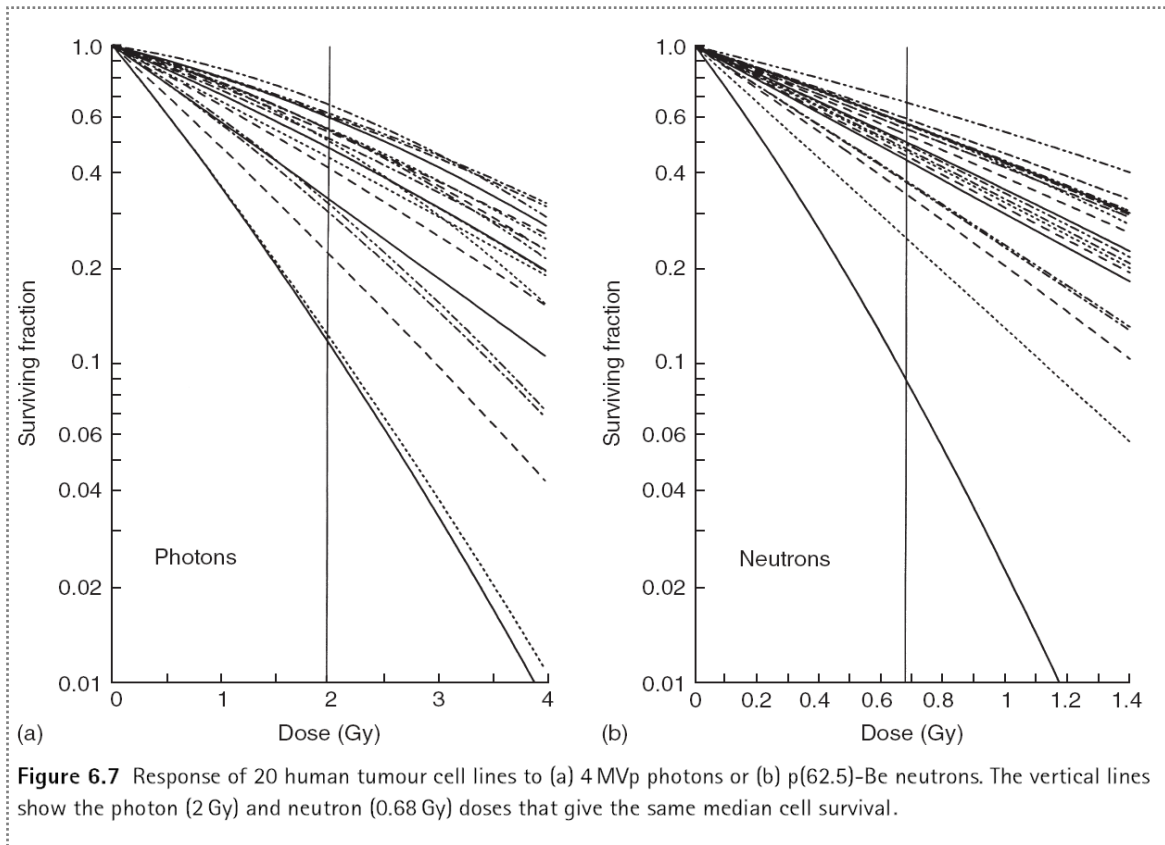


Figure 7: Radiosensitivity varies between different cell lines (Ref. 44).

Experimental results show that many organs have a strong volume effect.⁴⁵ Such organs will have different tolerance doses when differing amounts of the organ are irradiated. In Figure 8, the four curves from left to right are response curves for 20mm, 8mm, 4mm and 2mm of rat cervical spinal cord after proton irradiation, respectively.⁴⁵ By decreasing the irradiated length from 20mm to 2mm, the 50% responder dose increased from about 20 Gy to nearly 90 Gy, which is over 4 times higher. Moreover, this group did further research and found that the distribution of the doses has significant influence on radiation response of rat cervical cord (Figure 9).²⁷ The two 4mm segments irradiated has much higher tolerance dose than a single 8mm segment. These facts confirm that the spatial information for a radiotherapy plan must be taken into account when assessing a radiotherapy treatment plan.

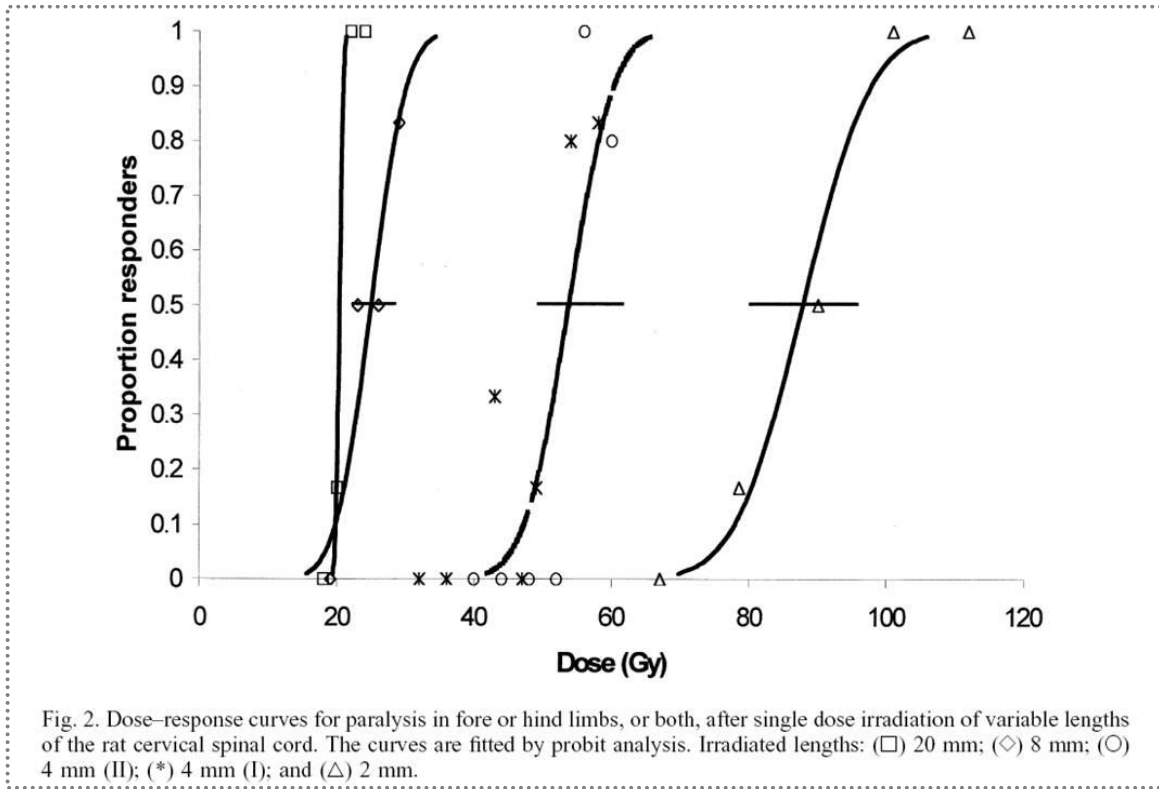


Figure 8: Rat spinal cord showed strong volume effect (Ref. 45)

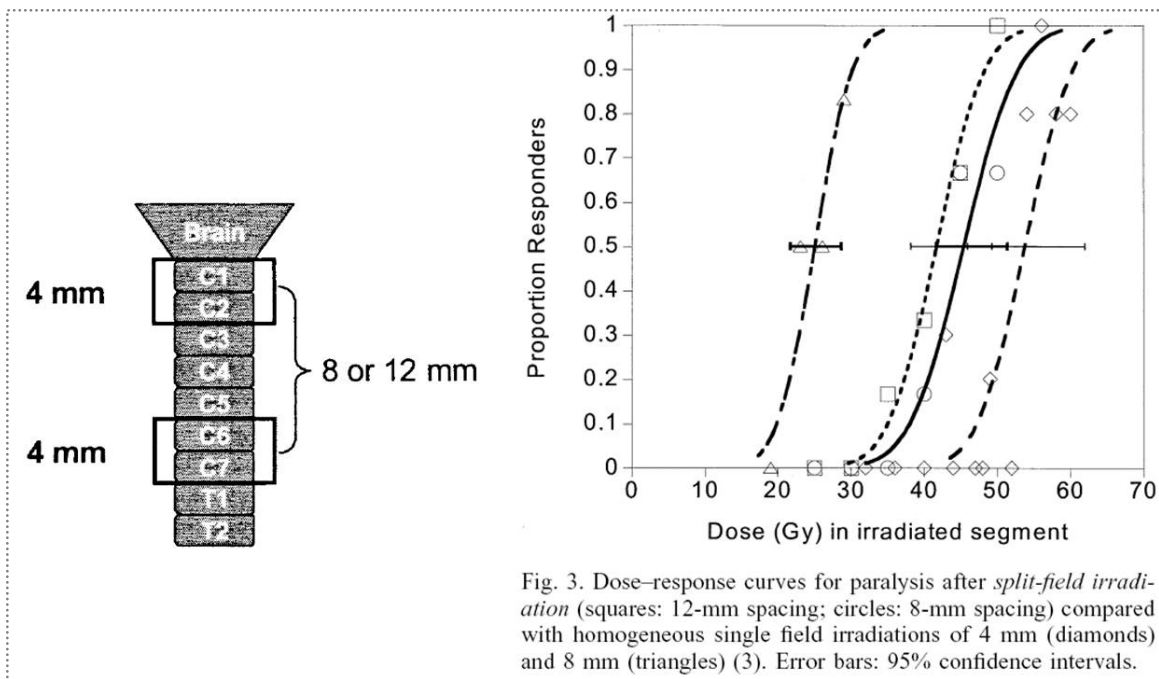


Figure 9: Rat spinal cord response curve shifts in the *split-field irradiation* experiment reported by H.P. Bijl *et al* (Ref. 27).

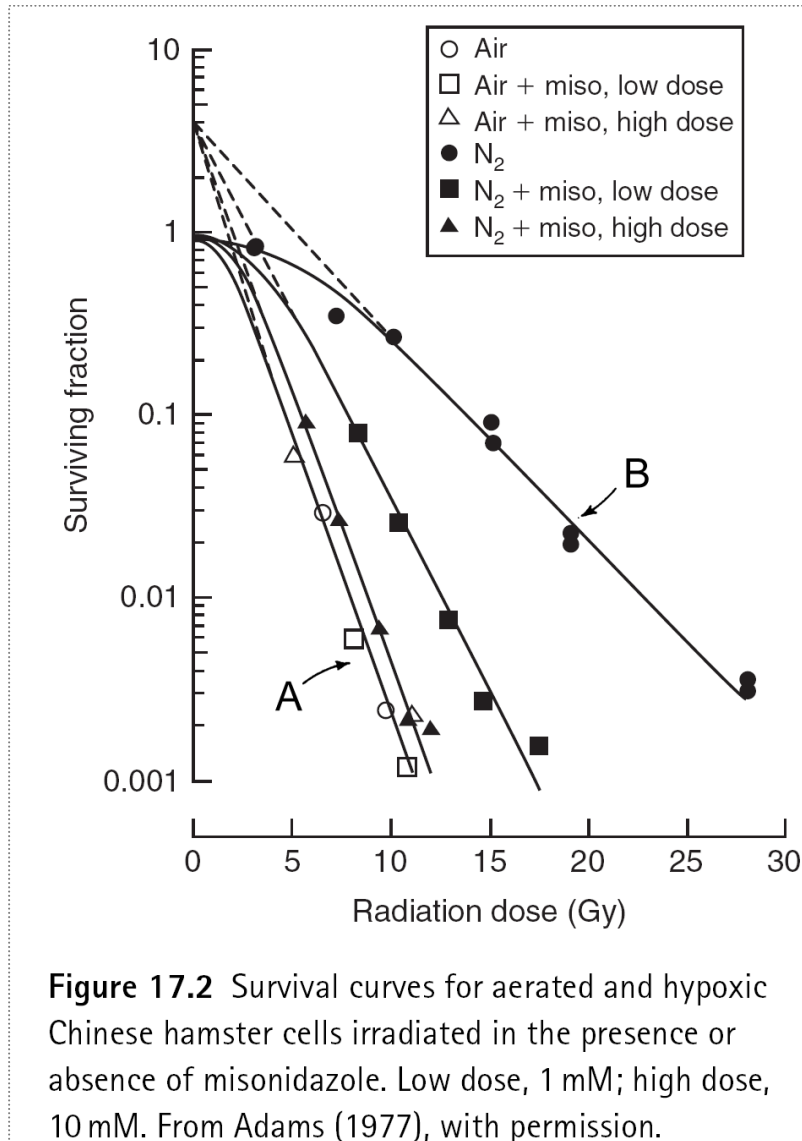


Figure 10: Increased radioresistance from A to B induced by hypoxia (Ref. 44).

Hypoxia is another important factor that may introduce great uncertainty in predicting the outcomes of a radiotherapy plan. It is assumed that the more severe the hypoxia is in a tumor, the more radioresistant the tumor will be. For example in Figure 10, from line A to B, the concentration of oxygen is reduced by replacing air with nitrogen. The dose required to induce a survival fraction of 0.1 for B is about three times higher than that for A.⁴⁴ Thus, knowledge of whether hypoxia is present in a tumor and its extent

becomes critical to a radiotherapy treatment.

Tumor cell proliferation also needs to be taken into consideration because IMRT radiotherapy treatment course may take up to 8 or 9 weeks. Many studies about tumor repopulation during the course of radiotherapy have been published.⁴⁶⁻⁵² For a head-neck cancer treatment that takes longer than four weeks, the effect of cell proliferation is equivalent to a loss of radiation dose of about 0.6 Gy/day.⁴⁶ The article by R. Tarnawski *et al* concludes that accelerated repopulation could start after two weeks of treatment, and during treatment gap there is effectively 0.75 Gy/day loss while during irradiated days the loss is 0.2 Gy/day.⁴⁷ A clinical study for cervical cancer was reported by J.Z. Wang *et al*.⁴⁸ They found the predicted onset time for cell repopulation for cervical cancer was 19 days. *In vivo* experiments performed by R.E. Durand *et al* indicates that tumor cell proliferation may start after only a few fractions of radiation exposure in human tumor xenografts.⁴⁹ Additionally, their results suggest that pretreatment potential doubling time values may underestimate the actual re-growth rate. For non-small-cell lung cancers, an association between overall treatment time and outcomes is found on the multivariate analysis and survival outcomes are better with shorter treatment time.⁵⁰ For treatments beyond six weeks, a notable loss of survival rate of 1.6% per day is observed, which corresponds to a time-dose tradeoff of 0.6-0.8 Gy/day at 2 Gy fraction size.⁵¹ Although prostate cancer is considered a slow growing tumor and the influence of tumor repopulation is not as significant as the aforementioned sites, a correlation is found between the overall treatment time and the treatment outcomes by D.J. D'Ambrosio *et al*.⁵² In their study, the non-treatment day ratio (NTDR), which is defined as the number of non-treatment days divided by the total elapsed days of treatment, is found to be a statistically significant predictor of

biochemical failure for low-risk prostate cancer patients who mostly had local-only diseases. Proliferation of prostate tumor begins at some time less than 52 days and the dose required to offset the extended treatment is about 0.24Gy/day.⁵³ These studies indicate that dose escalation would be needed to compensate for the dose loss due to the accelerated tumor cell proliferation. However, dose escalation would also increase the dose to normal tissues which could result in higher complication rate.

TCP (tumor control probability) and NTCP (normal tissue complication probability) are commonly calculated to evaluate treatment plans in addition to static dose and DVHs.⁵⁴⁻⁵⁸ The aim of such calculations is to incorporate some radiobiological parameters and distill the 3D dose information into a single metric or a handful of metrics to be used for plan evaluation and comparison. Generalized equivalent uniform dose (gEUD)⁵⁹⁻⁶⁰ is a common approach which incorporates certain tissue specific parameters and attempts to account for volume effects^{39, 45} in radiotherapy. Unfortunately, most studies or tools calculate gEUD and then TCP or NTCP from DVH data distilled from static dose distributions.^{37, 61-65} As discussed previously, the dose distribution calculated by the treatment planning system is in general not a true representation of the actual absorbed dose distribution or the biologically effective dose distribution, and the use of the DVH inherently eliminates all spatial dose information.

To compensate for the lack of spatial information within the DVH, supplemental methods of representation have been proposed.⁶⁶⁻⁶⁷ C.W. Cheng *et al* developed zDVH which is defined as a differential dose–volume histogram with respect to a CT slice position.⁶⁶ Instead of using one dose-volume curve for a 3D target in the current format of DVH, they decompose it into multiple curves with each representing one isodose level.

Thus they are able to incorporate the axial spatial information by plotting percentage volume with respect to the CT slice location for each isodose level. But within each slice, "cold" or "hot" spot locations are still unknown. Later, K.S. Chao *et al* introduced a conceptual method to integrate spatial dose information into dose-volume scoring-function histograms (DVSH).⁶⁷ A scoring function which represents the distance from the gross tumor volume (GTV) edge to the clinical target volume (CTV) edge is used. DVSH plots the dose (vertical scale) and the volume (on a color scale) against the score (horizontal scale). Thus at each score (a spatial location), one can read the dose range and the volume that each dose level occupies. However, DVSH not only looks totally different from DVH format but also uses a color scale for the volume size, which makes it less intuitive than the simple DVH concept.

In conclusion of all the aforementioned discussions, the spatial and biological information should also be taken into account in treatment evaluation and optimization process. Many software tools have been developed to incorporate biological information into the radiotherapy treatment planning and/or evaluation process.^{61, 63-65, 68-71} And during the years of developing this work, other commercial planning systems such as Eclipse and Monaco (Elekta, Stockholm, Sweden) also added biological optimization and evaluation modules. Although each of these tools or systems offers different and useful features for plan analysis, most of them do not retain biological information at the voxel level which limits their ability to preserve the spatial information. In fact, none of them provides computerized algorithms to optimize spatial dose distributions within a specific structure. Here I present a new treatment plan evaluation tool called SABER (**S**patial **A**nd **B**iological **E**valuation for **R**adiotherapy) which not only provides standard biological plan evaluation

but also transforms physical doses at the voxel level and incorporates both HRS and spatial information. In addition, the software can incorporate hyperradiosensitivity (HRS, will be discussed later) into the plan evaluation. In the next session, I will outline the methods and models we used for the project.

CHAPTER 2

Methods and Modeling

Both spatial and biological information are necessary in order to perform true optimization of a treatment plan and for predicting clinical outcome. The SABER software system overcomes some limitations of the current commercial planning systems. It provides spatial and biological plan evaluation. It incorporates hyperradiosensitivity using the induced-repair model and applies the new concept of Dose Convolution Filter to simulate dose wash-out effects due to cell migration, bystander effect, and tissue motion during treatment. Further, Spatial DVH (sDVH) is introduced to evaluate the spatial dose distribution in the target volume. Finally, generalized equivalent uniform dose is derived from both physical dose distribution (gEUD) and EQD₂ distribution (gEUD₂), and the software provides three models for calculation of TCP, NTCP, and Complication-free TCP (P+).

2.1 Retaining Spatial Information

2.1.1 Dose Convolution Filter

When inhomogeneous doses are present, any relative change in the location of a particular volume element of tissue with respect to the delivered dose distribution will result in changes to the dose received by that volume element. Tissue in a higher dose region in one fraction may reside in a lower dose region in another fraction. The concept of PTV is developed to compensate for uncertainties in the location of a structure by adding a margin to the clinical target volume (CTV). However, applying the PTV in the planning process still creates a static dose distribution delivering the prescription dose but

to a larger target volume than CTV. It cannot predict or estimate the difference between the planned and the delivered dose distributions.

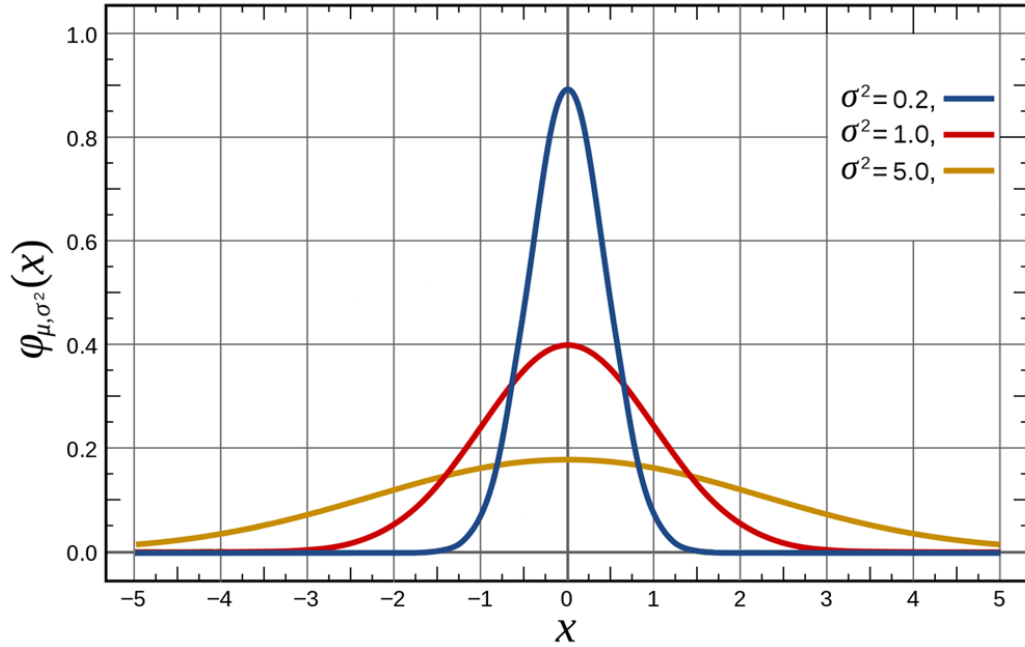


Figure 11: one dimensional continuous Gaussian filter

To retain the spatial information, a Dose Convolution Filter (DCF) is used. DCF was initially developed by Y. Huang *et al* to incorporate spatial dose information into tissue modeling.^{34, 45} Tissue response was calculated by the relative-seriality NTCP model with DCF-filtered dose distribution as input. The parameter σ was determined from published data. After applying the DCF, the NTCP model successfully fitted the experimental data with a predicted value of $\sigma = 2.6 \pm 0.5 \text{ mm}$, which is consistent with 2mm migration distances of remyelinating cells. This proves that outcome can be predicted more accurately using DCF-filtered dose distribution than that from static dose distribution.³⁴ A similar concept has been reported independently by M. Adamus-Gorka *et al.* by assuming an effective size of functional sub-units.⁷² In its original format, DCF was a one dimensional Gaussian filter (Figure 11) which was applied to the beam profile along the spinal cord. We have applied the DCF concept here and in addition to its originally

proposed use to predict the effects of cell migration and bystander effects, DCF is applied to also simulate the effect of random setup uncertainties and organ movements.⁷³ Furthermore, DCF is expanded to three dimensions. The degree of smoothing in each dimension can be defined independently to help simulate real situations. DCF may help provide a more accurate prediction of tumor control and tissue response by incorporating the fact that individual volume elements do not exist at the same location within the dose distribution at every fraction and that cells may migrate from one volume element to another.

In this work, two types of three dimensional DCF are provided: isotropic DCF and anisotropic DCF. In isotropic DCF, the three dimensions have the same degree of smoothing. In anisotropic DCF, the three dimensions can be controlled independently. The size of DCF is defined by the number of voxels. Voxel size is obtained from DICOM RT files exported from Eclipse. For example, a two dimensional filter of size 3x3 is shown in Figure 12. The values in the filter matrix (discrete probability density) are determined by the parameter σ in the Gaussian function. The edges of the original matrix are padded with zeros for convolution purpose (Figure 12).

The degree of smoothing is defined by both the size of DCF and the parameter σ . The size indicates how distant a voxel is affected by its surrounding voxels, while the σ determines how a voxel is weighted inside a region of the filter size. As in Figure 12, the filter with $\sigma^2 = 0.5$ is more center-weighted than the filter with $\sigma^2 = 2$. One can imagine, as σ gets bigger and bigger, the convolution result for each individual voxel approaches the mean value of the convolving voxels. On the other hand, as σ gets smaller and smaller, the convolution result for each individual voxel approaches its own value. Figure 13 shows an

example of 2D smoothing. The original data is a 20x20 matrix with random values. The data were convolved with filters of different sizes and different σ values from which we can see the effect of the parameters. It is worth to point out that when σ value is small (e.g. $\sigma^2 = 0.5$), the size of the filter has little impact on the degree of smoothing.

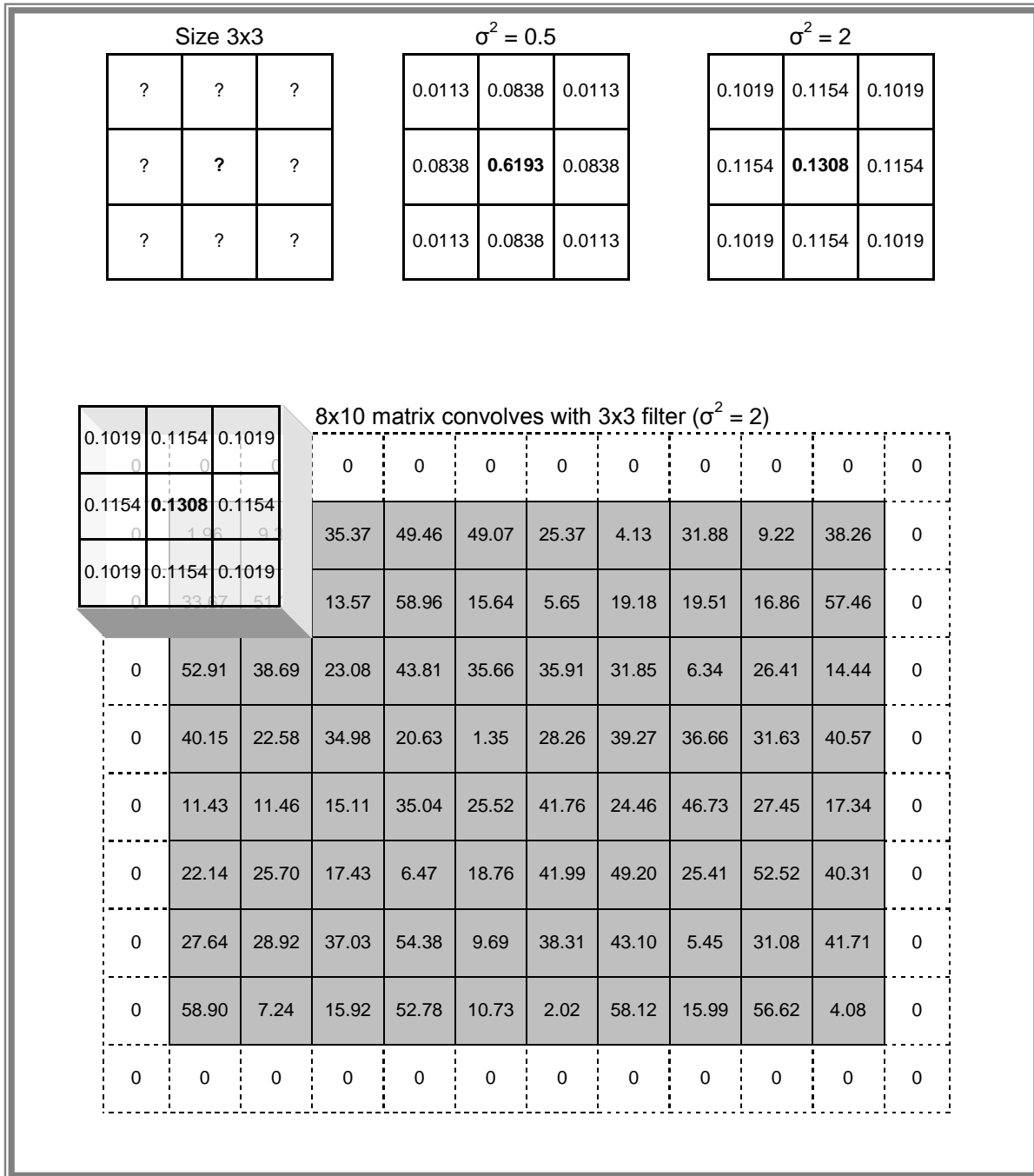


Figure 12: An 8x10 matrix convolves with 2D 3x3 Gaussian filters

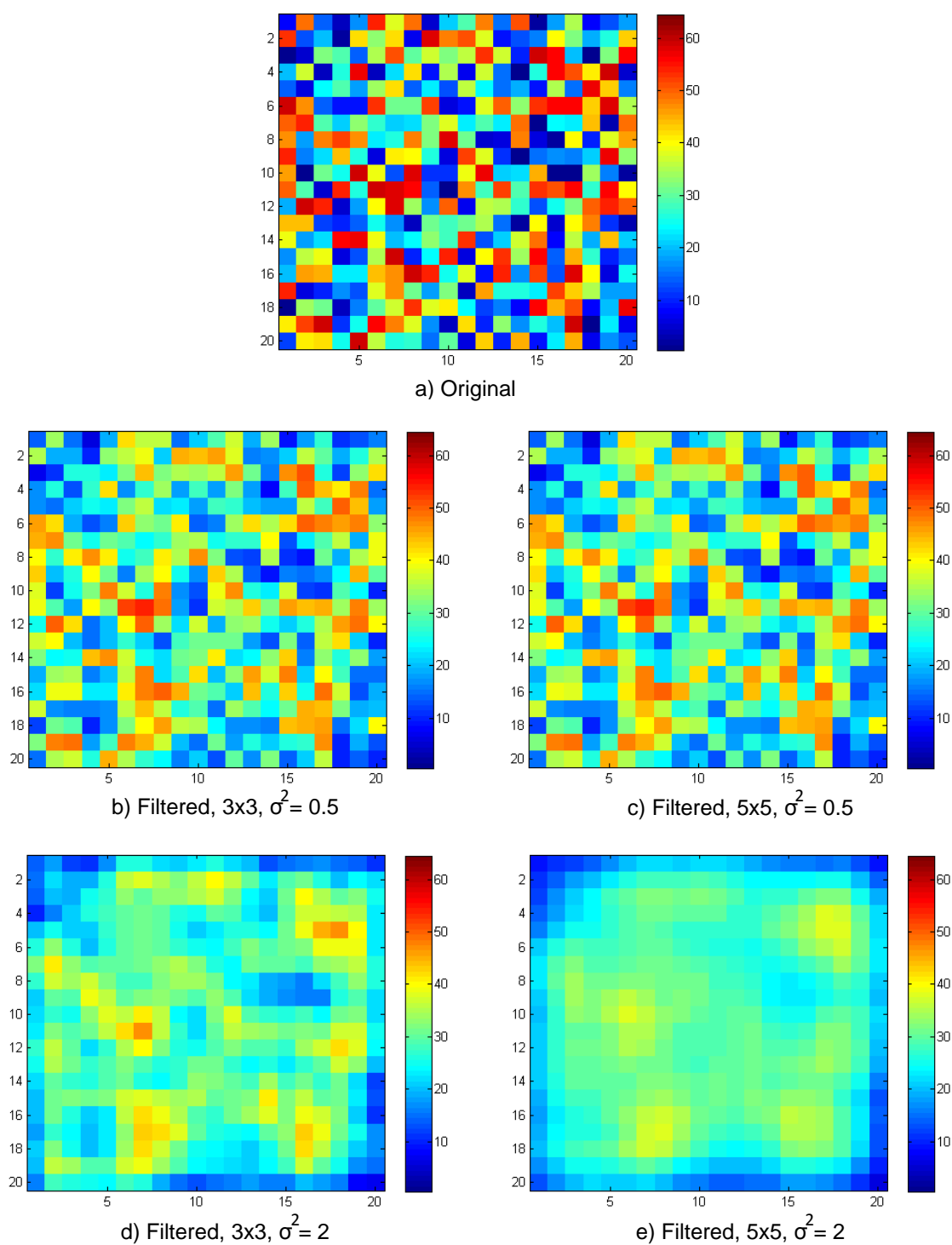


Figure 13: Effect of the filter parameters (size and σ).

2.1.2 Spatial DVH

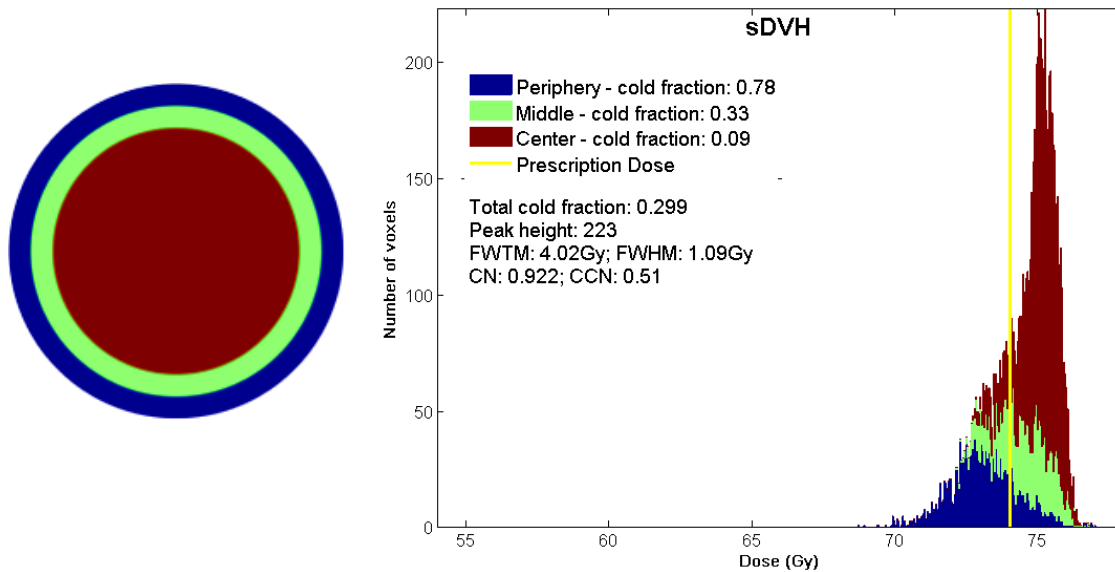


Figure 14: The sDVH concept and a typical result.

To restore the spatial information to DVH format, we divide the target volume into sub-volumes and assign one color to each sub-volume. So the colors represent the spatial locations. Then we color-code the spatial information on the original DVH. The division of the target volume is computerized and can be made based on the known clonogen density distribution or the metabolic or biochemical activity distribution provided by functional imaging such as PET-CT (Positron Emission Tomography – Computed Tomography) images. For the examples presented in this work, we arbitrarily choose three regions for illustration purpose: center, middle, and periphery (Figure 14, additional regions can be defined as desired). Dose voxels in the different regions are color-coded in the cumulative or differential DVH (Figure 14). Thus a measure of spatial information is restored to the DVH in a format we call the spatial dose-volume histogram (sDVH). Statistics for "cold" spots, characteristics for differential sDVH peak (peak height, full-

width at half maximum (FWHM) and full-width at tenth maximum (FWTM)), and conformity information are also presented on the differential sDVH figure as they have proven useful in quantifying relative plan quality.

2.2 Biological Modeling

2.2.1 Fractionation sensitivity

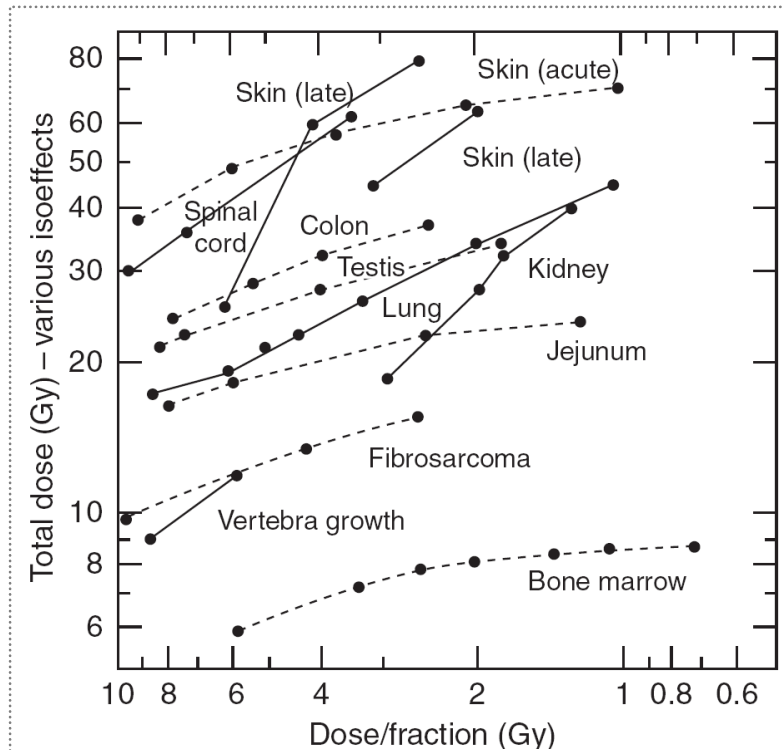


Figure 8.1 Relationship between total dose and dose per fraction for a variety of normal tissues in experimental animals. The results for late-responding tissues (unbroken lines) are systematically steeper than those for early-responding tissues (broken lines). From Thames *et al.* (1982), with permission.

Figure 15: Isoeffects of different fractionation schemes for a variety of normal tissues (Ref. 44).

As mentioned in the first chapter, radiotherapy is commonly delivered in multiple fractions with the exception of stereotactic radiosurgery in which the dose is delivered in one fraction. Fractionation schemes may vary depending on the tumor site, the tumor stage, and the institution's protocol, etc. Design of a fractionation scheme involves an understanding of dose response behavior of both the tumor and normal tissues and the total prescription dose is dependent upon the fraction size. For example, a prescription dose of 70Gy delivered in 35 fractions is not biologically equivalent to the dose of 70Gy delivered in 10 fractions, i.e. $2\text{Gy/fraction} \times 35\text{fractions} \neq 7\text{Gy/fraction} \times 10\text{fractions}$. This is because different organs or tumors react to fractionation differently (Figure 15⁷⁴). In radiobiology, this is usually termed the fractionation sensitivity. Optimization of a fractionation scheme requires knowledge of the relationships between total dose and dose per fraction for late-responding tissues, acutely responding tissues and tumors.⁴⁴

Models have been developed to describe the fractionation sensitivity, among which the linear-quadratic (LQ) model is the most popular (Figure 16). The LQ model is a mathematical fit to the cell survival curves but also carries physical meanings. The linear term α describes the lethal component of cell killing (DNA double strand breaks) induced by radiation. And the quadratic term β describes the sub-lethal damages where cells can repair (DNA single strand break). We chose to use the LQ model because it is widely accepted, simple and elegant and carries good explanation to the underlying reactions. Assuming there is fully repair between fractions, the cell survival fraction (SF) after irradiation predicted by the LQ model is:

$$SF = \exp(-\alpha D - \beta D^2)$$

where α is the parameter for the linear component and β is the parameter for the quadratic

term. D is the total prescription dose and d is the single fraction dose.

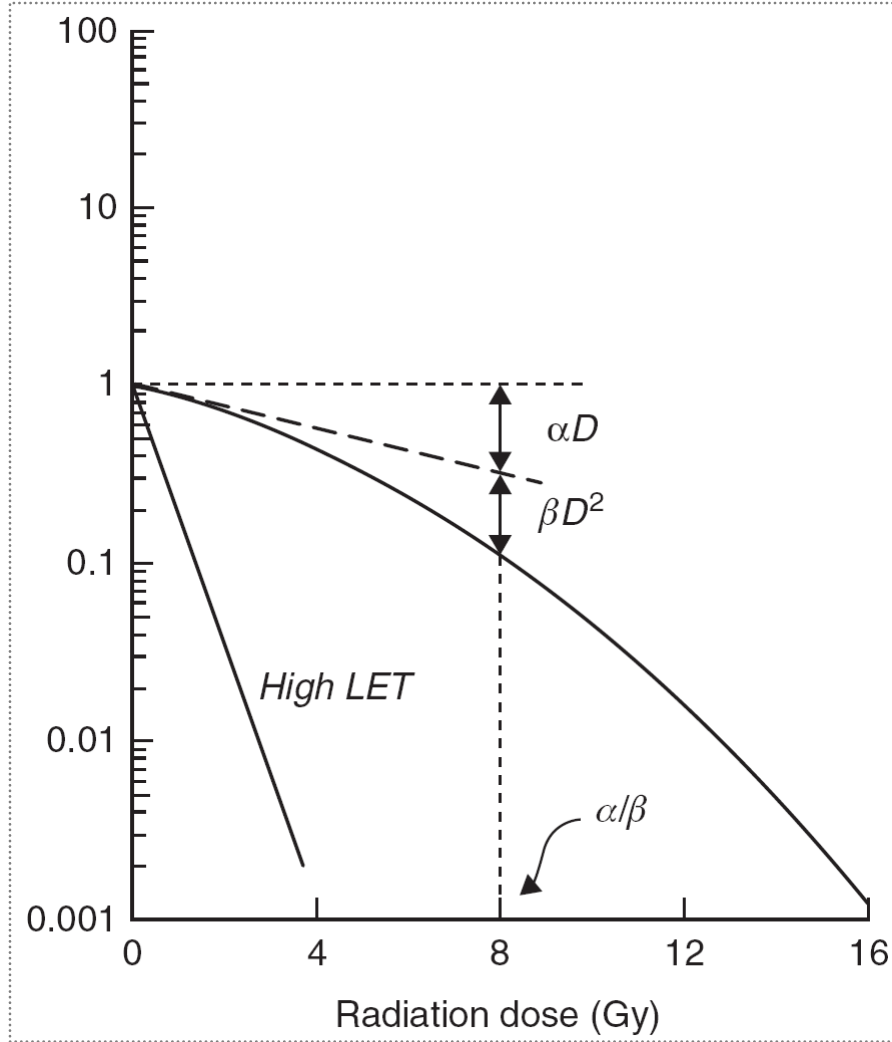


Figure 16: Linear-quadratic (LQ) model (Ref. 44).

On the other hand, in order to evaluate treatment plans created in different fractionation schemes for the same patient, a conversion of effective dose from one scheme to another is desired. This conversion incorporates fractionation sensitivity which is described by the α/β value. Based on the LQ model, the conversion can be expressed as:

$$D_{\text{ref}} = D \left(\frac{d + \alpha/\beta}{d_{\text{ref}} + \alpha/\beta} \right)$$

where d is the physical fraction dose and D is the total dose. D_{ref} is the total dose normalized to a reference fraction scheme incorporating fractionation sensitivity. d_{ref} is the reference dose per fraction used for the calculations. It is commonly chosen as 2Gy.

$$EQD_2 = D \left(\frac{d + \alpha/\beta}{2 + \alpha/\beta} \right)$$

2.2.2 Low-dose HyperRadioSensitivity (HRS)

The LQ model works very well in most clinical cases. But when doses are below 1Gy, the LQ model may underestimate the effect of radiation due to the fact that tumor cells may exhibit low-dose hyperradiosensitivity which is known as HRS.⁴⁴ As shown in Figure 17, the dotted line is fitted by the LQ model. But for doses less than 0.3Gy, the cells exhibit much higher sensitivity than that predicted by the LQ model. A possible reason is that at such low dose, the cell repair mechanism is not activated. As the dose increases from 0.3 to 1Gy, cells have increased radioresistance (IRR) presumably due to induced repair.⁴⁴ So the overall cell killing below 1Gy is under-estimated by the LQ model. A correction to the LQ model is needed for such low doses. In this work, we employed the Induced Repair (IR) model⁷⁵⁻⁷⁷:

$$SF = \exp \left[-\alpha d \left(1 + (\alpha_s/\alpha - 1)e^{-d/d_c} \right) - \beta d^2 \right]$$

To convert the physical dose to EQD2, we include the HRS factor into the α/β .

$$EQD_2 = D \left(\frac{d + \left(\alpha/\beta \right)_{HRS}}{2 + \left(\alpha/\beta \right)_{HRS}} \right)$$

and

$$\left(\frac{\alpha}{\beta}\right)_{\text{HRS}} = \frac{\alpha}{\beta} (1 + (\alpha_s/\alpha - 1)e^{-d/d_c})$$

where α_s is the larger α at very low doses approaching zero; d is the single fraction dose; d_c is the constant at which induction of repair is 63% complete.

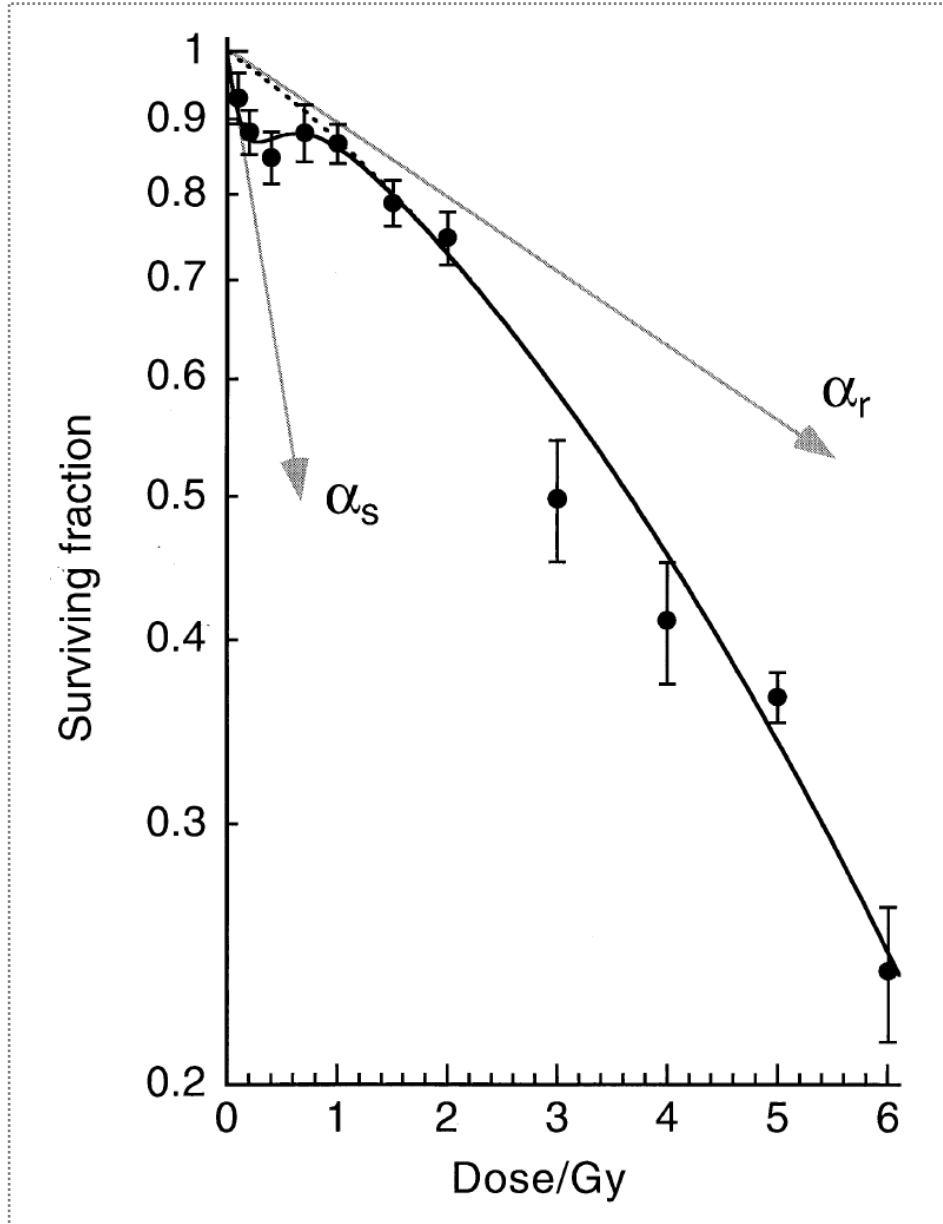


Figure 17: HRS experimental data (asynchronous T98G human glioma cells) fitted with LQ model and IR model (Ref. 76). The parameter α_r is the same as the linear component factor in the LQ model.

2.2.3 Generalized Equivalent Uniform Dose (gEUD)

Dose distributions in radiotherapy are usually non-uniform, especially in IMRT. A natural question is how much dose an entire structure will receive from a specific treatment plan. In other words, what is the Equivalent Uniform Dose (EUD) to the structure? EUD was introduced as the biological equivalent dose that, if delivered uniformly to the entire structure, results in the same cell killing as the non-uniform dose distribution would. EUD was initially defined for targets only.⁵⁹ The concept was later expanded to include normal tissues as well and is termed as generalized EUD (gEUD).^{60, 78} The equation is

$$gEUD = \left(\frac{1}{N} \sum_{i=1}^N d_i^a \right)^{1/a}$$

where d_i is the dose in voxel i ; N is the total number of voxels; a is the volume parameter which indicates the relevance of the non-uniformity of dose distributions. For targets, $a < 0$. For normal organs, $a > 0$. As a approaches $-\infty$, gEUD equals the minimum voxel dose which means the low dose in the target dominates. Similarly, as a approaches $+\infty$, gEUD equals the maximum voxel dose which means the high dose in the normal organ dominates. For example, in Figure 18 the average value of the table data is 3. If we set the a value to 5, the gEUD would be 3.6. If the a value is 100 instead, the gEUD will become 4.9 which is approaching the maximum value 5. When $a = 1$, gEUD becomes the arithmetic mean.

The gEUD often needs to be normalized to 2Gy fractions ($gEUD_2$).⁷⁹ This can be done either before or after calculation of gEUD. We will discuss this in more detail in section 2.3.

2	3	4			
2	3	5	a=1	a=5	a=100
4	2	2	gEUD=3	gEUD=3.6	gEUD=4.9

Figure 18: The character of the parameter a in gEUD calculation.

2.2.4 Tumor Control Probability (TCP)

TCP is a very common term in the field and is used mostly by researchers to predict the local control at a defined time. The shape of TCP curves follows the cumulative function of the continuous normal distribution (Figure 19). In this work, we deployed both logistic and Poisson TCP models.⁸⁰⁻⁸¹

The logistic TCP model is a phenomenological model.⁸⁰ The equation can be expressed as:

$$TCP = \frac{1}{1 + \left(\frac{D_{50}}{gEUD_2} \right)^{1/4\gamma}}$$

where D_{50} is the dose at 2Gy/fraction that results in 50% of tumor control; γ is the slope parameter of the TCP function at D_{50} .

The Poisson TCP model is based on Poisson statistics and describes the probability of no surviving clonogens.⁸¹ If we assume there are total N clonogenic cells and the survival fraction (SF) of clonogenic cells of a given dose D is SF_D , the Poisson TCP is

$$TCP = \exp(-N \cdot SF_D)$$

Now let us apply the LQ model to include fractionation sensitivity. Recall that

$$SF = \exp(-\alpha D - \beta Dd)$$

The Poisson TCP based on the LQ model becomes

$$TCP = \exp(-N \cdot \exp(-\alpha D - \beta Dd))$$

A common parameter in using the Poisson TCP model is $SF2$ which is the surviving fraction after a single 2Gy dose. If we convert physical dose to dose in 2Gy fractions (i.e. EQD_2 or $gEUD_2$), the Poisson TCP model can be express in $SF2$ and EQD_2 or $gEUD_2$:

$$TCP = \exp(-N \cdot SF2^{gEUD_2/2})$$

or

$$TCP = \exp(-N \cdot SF2^{EQD_2/2})$$

The first form is used in SABER Model 1 and 2. The second form can be applied to individual voxels, which forms the voxel-by-voxel Poisson TCP model assuming any surviving clonogenic cell can repopulate the tumor:⁸¹

$$TCP = \prod_{i=1}^n \exp(-N_i \cdot SF2^{EQD_{2,i}/2})$$

where N_i is the initial number of clonogen cells in voxel i ; $EQD_{2,i}$ is the EQD_2 in voxel i ; and n is the total number of voxels. If we assume uniform clonogen density, $N_i = N/n$.

2.2.5 Normal Tissue Complication Probability (NTCP)

Similar to TCP, NTCP is another frequently used term which describes the complication rate of a normal organ at a specific end point. The NTCP curve also follows the sigmoid shape like TCP (Figure 19). We adopted three NTCP models in this work.

The first one is logistic NTCP model.⁸⁰ It has the same form as the logistic TCP and it is purely a phenomenological model.

$$\text{NTCP} = \frac{1}{1 + \left(\frac{D_{50}}{g\text{EUD}_2} \right)^{1/4\gamma}}$$

where D_{50} is the dose at 2Gy/fraction that causes 50% of complication; γ is the slope parameter of the NTCP curve at D_{50} .

The second one is the so-called LKB model and was named in honor of the three authors – J.T. Lyman, G.J. Kutcher and C. Burman.⁵⁷⁻⁵⁸

$$\text{NTCP} = \frac{1}{\sqrt{2\pi}} \int_{-\infty}^t e^{-\frac{x^2}{2}} dx, \quad \text{where } t = \frac{g\text{EUD}_2 - D_{50}}{m \cdot D_{50}}$$

D_{50} is the dose at 2Gy/fraction that causes 50% of complication; m is the slope parameter of the NTCP curve at D_{50} .

The third model we included in the SABER software is the relative seriality NTCP model.⁵⁴ The model is derived based on the architecture of tissues (parallel, serial, and/or cross-linked functional subunits). The equation is:

$$\text{NTCP} = \left[1 - \prod_{i=1}^n (1 - P(D_i)^s)^{1/n} \right]^{\frac{1}{s}}$$

$$\text{and } P(D_i) = \left[1 + \left(\frac{D_{50}}{g\text{EUD}_{2,i}} \right)^{4\gamma} \right]^{-1}$$

where D_{50} is the dose that would cause 50% complication; γ is the slope of dose response curve at D_{50} ; s is the fitted relative seriality parameter of the tissue; n is the total number of voxels.

2.2.6 Complication-free Tumor Control Probability (P+)

Complication-free tumor control probability or tumor control without normal tissue complications (P+) is another term that combines TCP and NTCP and is commonly used to predict treatment outcomes. It gives a single value that takes into account the predicted tumor control and predicted normal tissue complications for a treatment plan. In general, P+ can be calculated as:⁸²

$$\begin{aligned} P+ &= TCP - TCP \cdot NTCP \\ &= TCP - NTCP + \delta \cdot (1 - TCP) \cdot NTCP \end{aligned}$$

where δ specifies the fraction of patients with statistically independent TCP and NTCP.

The approximate value of δ is 0.2.^{54, 82}

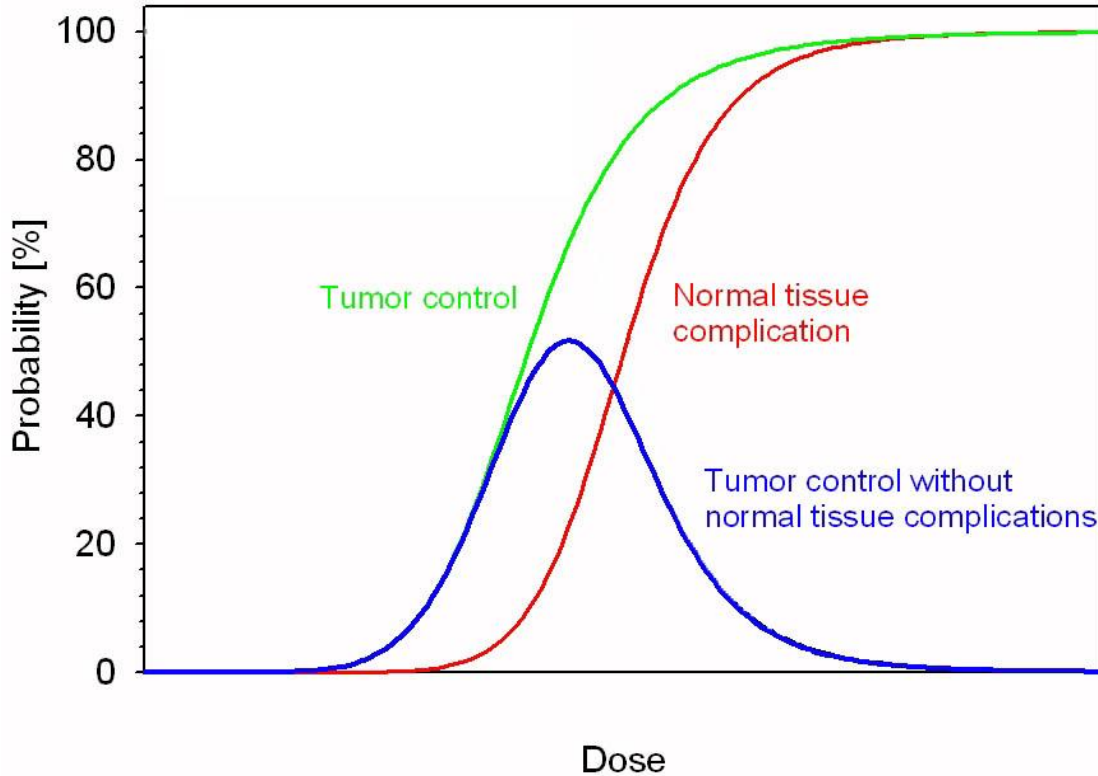


Figure 19: Tumor control probability (TCP, green line), normal tissue complication probability (NTCP, red line) and complication-free tumor control (P+, blue line).

2.3 SABER models

We provide three models to predict TCP and NTCP. Let us begin with TCP.

Model 1:

Voxel dose $d_i \rightarrow$ structure gEUD \rightarrow structure gEUD₂ \rightarrow structure TCP

We start from voxel doses to calculate gEUD. Then convert it to gEUD₂ which is the gEUD normalized to 2Gy per fraction. Equations are:

$$\text{gEUD}_2 = \text{gEUD} \left(\frac{\text{gEUD} + \alpha/\beta}{2 + \alpha/\beta} \right), \quad \text{where } \text{gEUD} = \frac{\text{gEUD}}{\# \text{ of fractions}}$$

TCP is calculated based on gEUD₂.

In this model, the only parameter that can be varied spatially is the α value as the 3D dose matrix is converted to a single number (gEUD) in the first step. By nature, the parameter α is the fitted value that makes the effect of a uniform dose distribution the same as the effect of a non-uniform dose distribution. So theoretically the parameter α is a constant for a specific region of interest.

Model 2:

Voxel dose $d_i \rightarrow$ voxel EQD_{2,i} \rightarrow structure gEUD₂ \rightarrow structure TCP

We start from voxel doses and convert the physical dose matrix to EQD₂ matrix. The gEUD₂ is directly derived from the EQD₂ matrix. Then TCP is calculated from gEUD₂.

In this model, the EQD₂ is converted from physical dose voxel by voxel. So the fractionation sensitivity (α/β) could vary spatially. Currently a constant value is used for each structure. As we obtain such information in the future, the variation could be easily incorporated.

Model 1 and Model 2 would yield different values of structure gEUD₂ and thus different TCPs. We will discuss this in detail in the later chapter.

Model 3:

Voxel $d_i \rightarrow$ voxel EQD_{2,i} \rightarrow voxel TCP_i \rightarrow structure TCP

We also start from the actual voxel doses and convert the physical dose matrix to EQD₂ matrix. After that, TCP is calculated for each individual voxel (TCP_i). The overall TCP is then derived from TCP_i.

The significant difference between Model 2 and Model 3 is that in Model 3 no gEUD formulism is used. So we could vary not only the fractionation sensitivity (α/β), but also the clonogen density and the radiosensitivity if such information is available.

Similarly, we provide three models for NTCP.

Model 1:

Voxel dose $d_i \rightarrow$ structure gEUD \rightarrow structure gEUD₂ \rightarrow structure NTCP

Model 2:

Voxel dose $d_i \rightarrow$ voxel EQD_{2,i} \rightarrow structure gEUD₂ \rightarrow structure NTCP

Model 3:

Voxel $d_i \rightarrow$ voxel EQD_{2,i} \rightarrow structure NTCP

In Model 1 and Model 2, both logistic NTCP model and LKB NTCP model are available. In Model 3, NTCP is calculated using the relative seriality NTCP model.⁵⁴

2.4 Work flow

Treatment plans are created in the Eclipse treatment planning system. DICOM RT files (dose, structure set, and plan) are exported without CT images, thus anatomy information is not used in the SABER software. For each treatment plan, three DICOM

RT files (dose, structure set, and plan) are imported into the SABER software.

A 3D dose matrix is constructed from the DICOM RT dose file. In the DICOM RT dose file, the dose values stored for each voxel are not actual doses in Gy or cGy, but very large unsigned integers. There is an attribute in the DICOM RT file called “DoseGridScaling” which is the factor to convert the large integers to actual values in Gy or cGy. In this work, the scaling factor is used when constructing the 3D dose matrix. The 3D physical dose is then converted to EQD₂ using the LQ model.⁴⁴ We also provide an option to convert to EQD₂ using the IR model which takes into account HRS.⁸³⁻⁸⁴ The conversion from physical dose to EQD₂ takes place at different steps depending on the selected SABER model. Both the original 3D physical dose and the new 3D EQD₂ are retained and can be displayed by the software.

To approximate the effective delivered dose distribution from the static dose distribution, we apply a 3D DCF to the 3D physical dose and the 3D EQD₂ distributions.^{34, 73} In this software, we create two formats for the application of DCF: a) isotropic DCF in which the degree of smoothing is the same for all directions; b) anisotropic DCF in which the degree of smoothing can be different for all three dimensions. In both formats, the user is able to define the degree of smoothing (the size of the filter and Gaussian σ). Both the original and the DCF-filtered dose distributions are retained and can be displayed by the software.

Structure contour points and coordinate information are gathered from the DICOM RT files. The software categorizes target dose voxels by their locations within the PTV. For the examples presented in this work, we arbitrarily choose three regions for categorization: center, middle, and periphery (Figure 14, additional regions can be defined

as desired). The periphery contains voxels within the most outer shell of the PTV. The shell of voxels next to the periphery is defined here as middle, and the remainder of the PTV is categorized as center. The thickness of the periphery and the middle can be modified individually as desired. For the examples in this study, the thickness of each region is chosen as one voxel dimension. Voxel size is determined by the Calculation Grid Size and the Calculation Model settings within the Eclipse TPS. Dose voxels in the different regions are color-coded in the cumulative or differential DVH (Figure 14). Thus the sDVH is created.

From the 3D physical dose distribution, $gEUD^{59}$ is calculated and normalized to 2Gy fractions. Similarly, from the 3D EQD_2 distribution, $gEUD_2^{79}$ is derived. To predict treatment outcome, we develop a “Biological Evaluation” module which provides the three SABER models using existing TCP models (Poisson^{79, 81}, logistic⁸⁰, and voxel-by-voxel Poisson), NTCP models (logistic⁸⁰, Lyman–Kutcher–Burman⁵⁷⁻⁵⁸, and voxel-by-voxel relative seriality⁵⁴) and P_+ ⁵⁴. A simplified function called “Excel BioEval” is also provided for simple and quick biological plan evaluation. The function generates a programmed Excel workbook in a few seconds which includes $gEUD$, TCP, and NTCP for all structures.

2.5 Research materials

Eclipse TPS v8.1 (Varian Medical Systems Inc., Palo Alto, CA).

Post-treatment anonymous CT images (in Eclipse TPS).

Exported DICOM RT files (dose, structure set, and plan only. No anatomy information).

Matlab v7.9 (The Mathworks, Inc., Natick, MA).

CHAPTER 3

SABER Software Demonstration

3.1 SABER Software Demonstration

In this chapter, I will present the detailed features of the SABER software including software screenshots and examples of using the software.

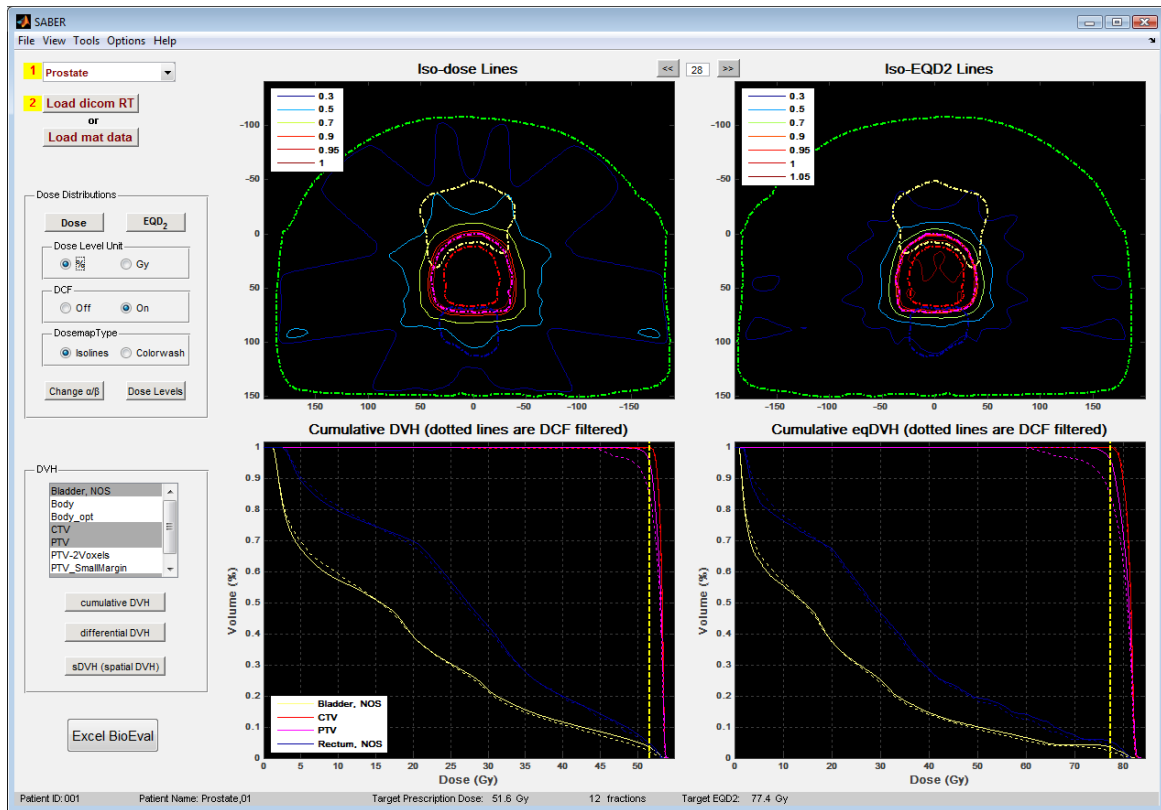


Figure 20: SABER software main graphical user interface. On the left are the function panels. The four figures as shown are: top left isodose lines; top right, iso-EQD2 lines; bottom left: cumulative DVHs; bottom right: cumulative eqDVH (DVH normalized to 2Gy fractions). The dotted lines represent the DCF-fitted DVHs. The vertical dashed line is the prescription dose (on DVH figure) or prescription dose normalized to 2Gy fractions (on eqDVH figure).

Figure 20 is a screenshot of the main graphical user interface of the SABER software. The four figure windows have black background which is similar to Eclipse TPS and is more comfortable to look at on a computer screen. White background is also

available which is more suitable for printouts (Figure 25). On the left side are the function panels. Users can choose a tumor site and load plans exported in DICOM RT format or Matlab format previously saved using this software (Currently only a few tumor sites are included in the selection. The selection is used to read the parameters values stored in the build-in library. If the tumor site studied is not included in the list, user is still able to use the SABER software. But in such cases, the user has to provide all the parameters).

Functions provided here are:

- 1) view doses in percentages or absolute values (Gy) (Figure 20 vs Figure 22);
- 2) display isodose and iso-EQD₂ lines or color wash map (Figure 20 vs Figure 21);
- 3) turn DCF on or off;
- 4) change structures' α/β values (Figure 23);
- 5) select isodose levels to display on isodose and iso-EQD₂ plots (Figure 24);
- 6) plot cumulative DVH for selected structures (Figure 20);
- 7) plot differential DVH for selected structures (Figure 21);
- 8) plot sDVH (both differential and cumulative) (Figure 26, Figure 27);
- 9) execute "Excel BioEval" which performs simple and quick biological evaluation and returns the output in Excel format (Figure 28).

Additional functions can be found in the "Tools" and "Options" menu at the top of the main graphical user interface. Additional functions include:

- 1) execute "Biological Evaluation" module (Figure 29);
- 2) execute "Bio Plan Comparison" module (Figure 36);
- 3) use the IR model for EQD₂ conversion instead of the LQ model (Figure 30);
- 4) measure dose profile from color wash dose map (Figure 31);

5) switch between isotropic DCF and anisotropic DCF and modify DCF parameters (size of filter and σ of Gaussian) (Figure 32). Reloading of DICOM RT files is required for this function to take effect.

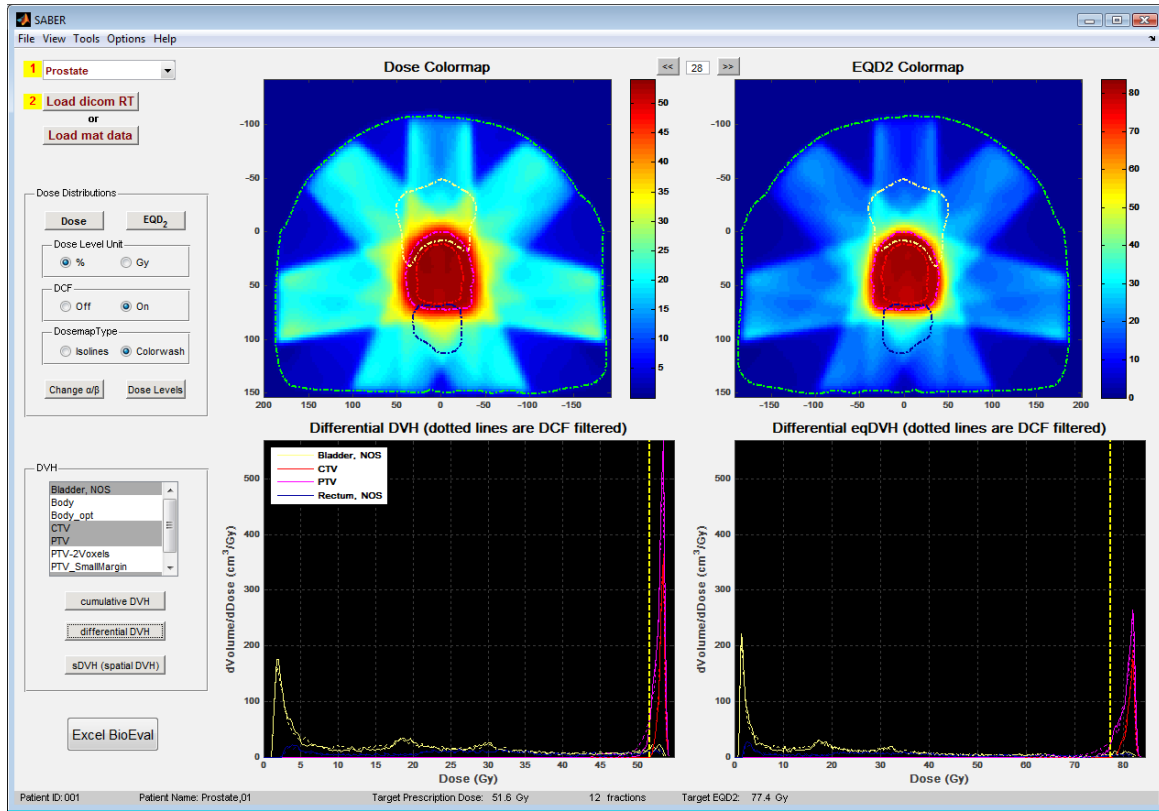


Figure 21: SABER main graphical user interface. Colorwash dose map and differential DVH are displayed.

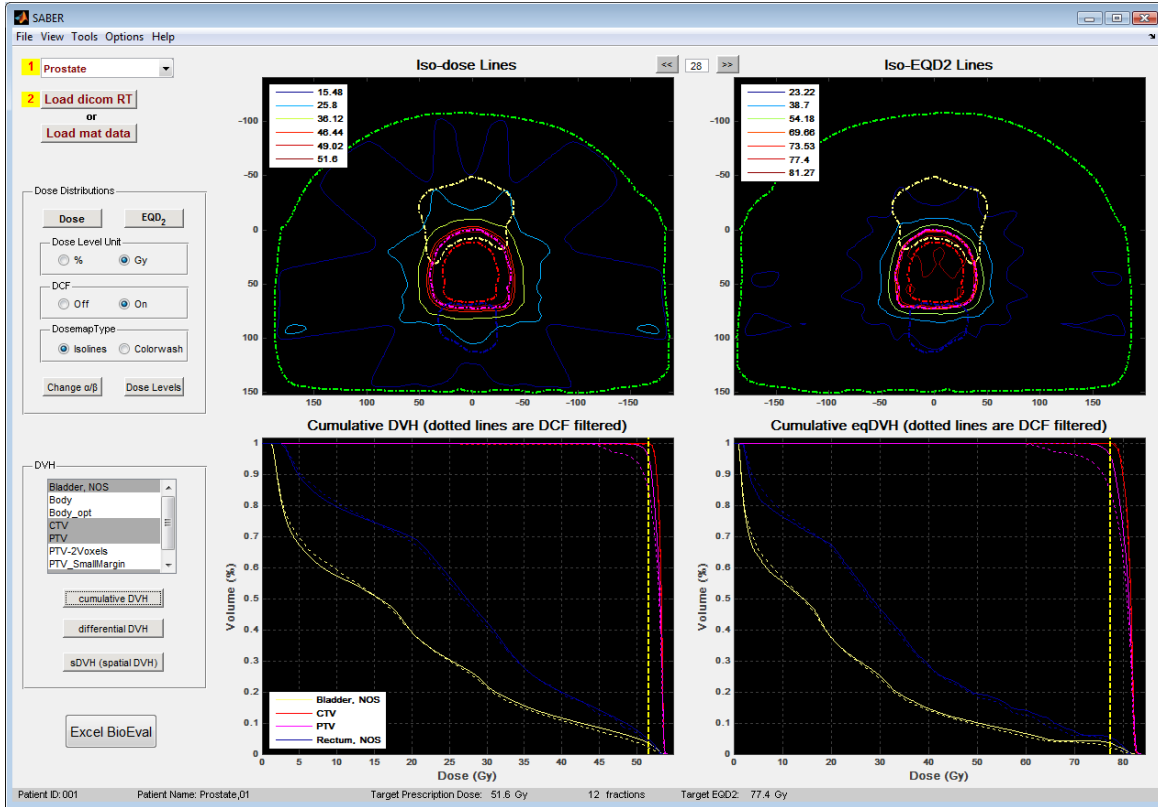


Figure 22: SABER main graphical user interface. Isodose lines in absolute values.

The window titled 'Figure 2: Alpha/beta for structures of interest' contains a table for selecting structures and providing their α/β values. The table has columns for 'Select', 'Structure', and ' α/β '. The structures listed are Bladder, NOS; Body; Body_opt; CTV; PTV; PTV-2Voxels; PTV_SmallMargin; and Rectum, NOS. The α/β values are 6 for Bladder, NOS; 2.6 for CTV and PTV; and 4 for Rectum, NOS. A note at the bottom states: 'NOTE: structures that are not selected will be assumed as body'. An 'OK' button is located to the right of the table.

	Select	Structure	α/β
1	<input checked="" type="checkbox"/>	Bladder, NOS	6
2	<input type="checkbox"/>	Body	
3	<input type="checkbox"/>	Body_opt	
4	<input checked="" type="checkbox"/>	CTV	2.6
5	<input checked="" type="checkbox"/>	PTV	2.6
6	<input type="checkbox"/>	PTV-2Voxels	
7	<input type="checkbox"/>	PTV_SmallMargin	
8	<input checked="" type="checkbox"/>	Rectum, NOS	4

NOTE: structures that are not selected will be assumed as body

Figure 23: Window for changing α/β values.

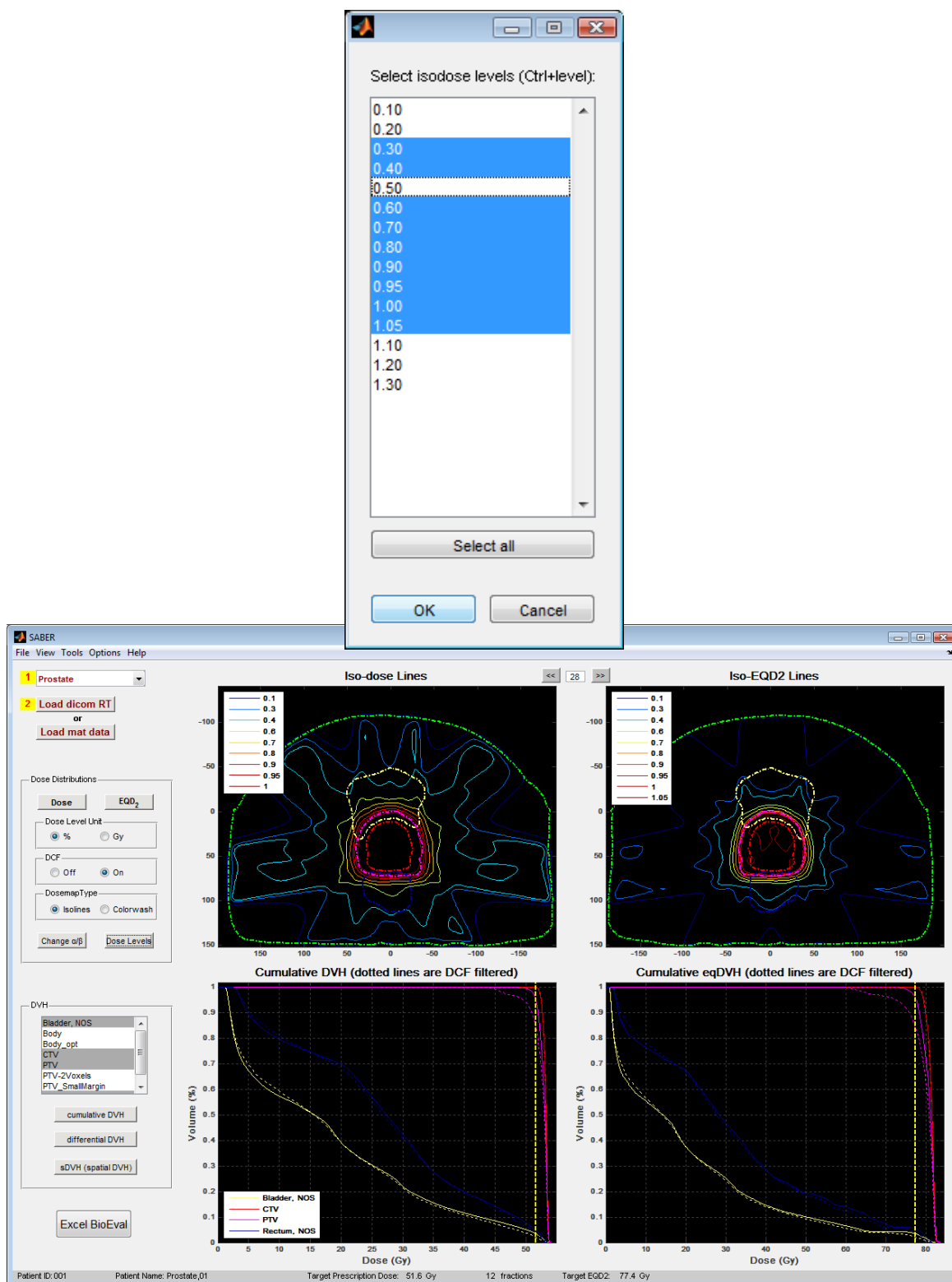


Figure 24: Select/change isodose levels to display

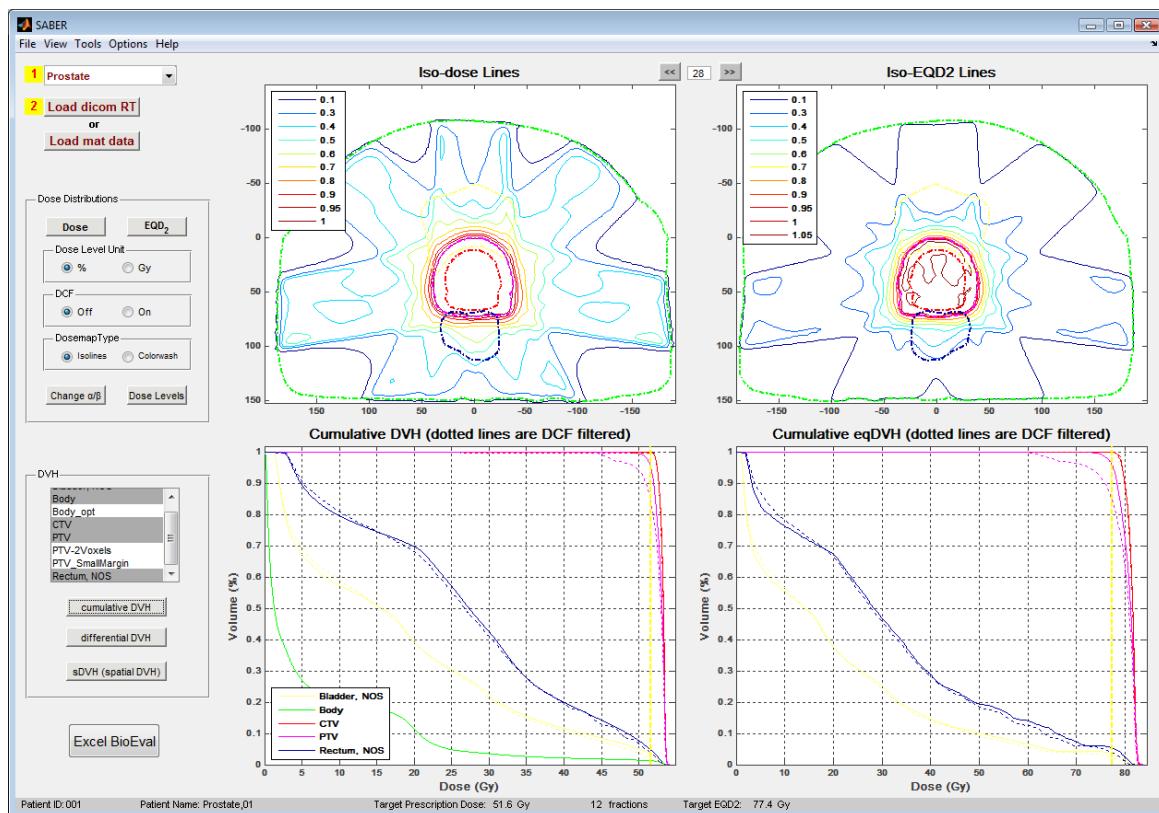


Figure 25: SABER main graphical user interface. The four figures are on white background which is more suitable for printouts.

SABER not only plots physical DVH and eqDVH (DVH normalized to 2Gy fractions), but also plots DVH and eqDVH from DCF-filtered dose distributions on the same figure. The dotted lines represent DCF-filtered DVHs, which we can compare with the original DVH to see the effect of the DCF application.

The SABER software provides sDVH in both cumulative and differential formats. A typical output from the sDVH module is shown in Figure 26. On sDVH plots, the numeric fraction volume of cold spots of each defined spatial location is also shown in the legend area. Each bin height in the differential sDVH figure is the absolute number of voxels at that dose level. The total colored area is the target volume. The cumulative format, on the other hand, has two parts separated by the prescription dose. On the left side are the under-dosed volumes; while on the right side are volumes that receive doses equal to or higher than the prescription dose. The color bars on the left side of the prescription dose are the cumulative summation of under-dosed voxel volumes from the lower end. In Figure 26, the sDVH results are from the original static physical dose distributions. We could also generate sDVH from EQD2 dose distributions (if it proves to be useful) or DCF-filtered distributions (Figure 27).

The “Excel BioEval” function, which only takes a few seconds to generate a programmed Excel workbook, is for simple and quick biological evaluation. As shown in Figure 28, all structures are included in the Excel file with one structure on each worksheet. Original DVH data are extracted from the DICOM RT dose file (DICOM attribute “DVHSequence”). All cells are filled and programmed automatically by the SABER software and it is extremely convenient for users to change the parameter values and immediately see the corresponding results.

The “Biological Evaluation” module (Figure 29) within the SABER software performs more comprehensive biological evaluation based on the three SABER models. This module supports the three NTCP models and three TCP models. The first two models of each group are based on $gEUD_2$ and the third one is voxel-based. Parameter values are filled automatically if the SABER software finds a match in its built-in library. The user is free to modify any parameter including whether to apply the DCF (a simple click on the checkbox to turn on or off). To assist in justifying the prescribed dose, a figure with TCP curve, NTCP curve, and P+ curve as a function of prescription dose is provided (Figure 29). Though there are high uncertainties associated with the biological parameters and the numeric values should not be considered as absolute, the relative magnitudes of these values are valuable for plan comparison purposes. Hence the “Bio Plan Comparison” module is provided to compare plans to a base plan (Figure 36). For the same reason, we also present multi-variable TCP, NTCP, and P+ figures as functions of their own parameters to cover large possible ranges for these values (Figure 33, Figure 34, Figure 35)

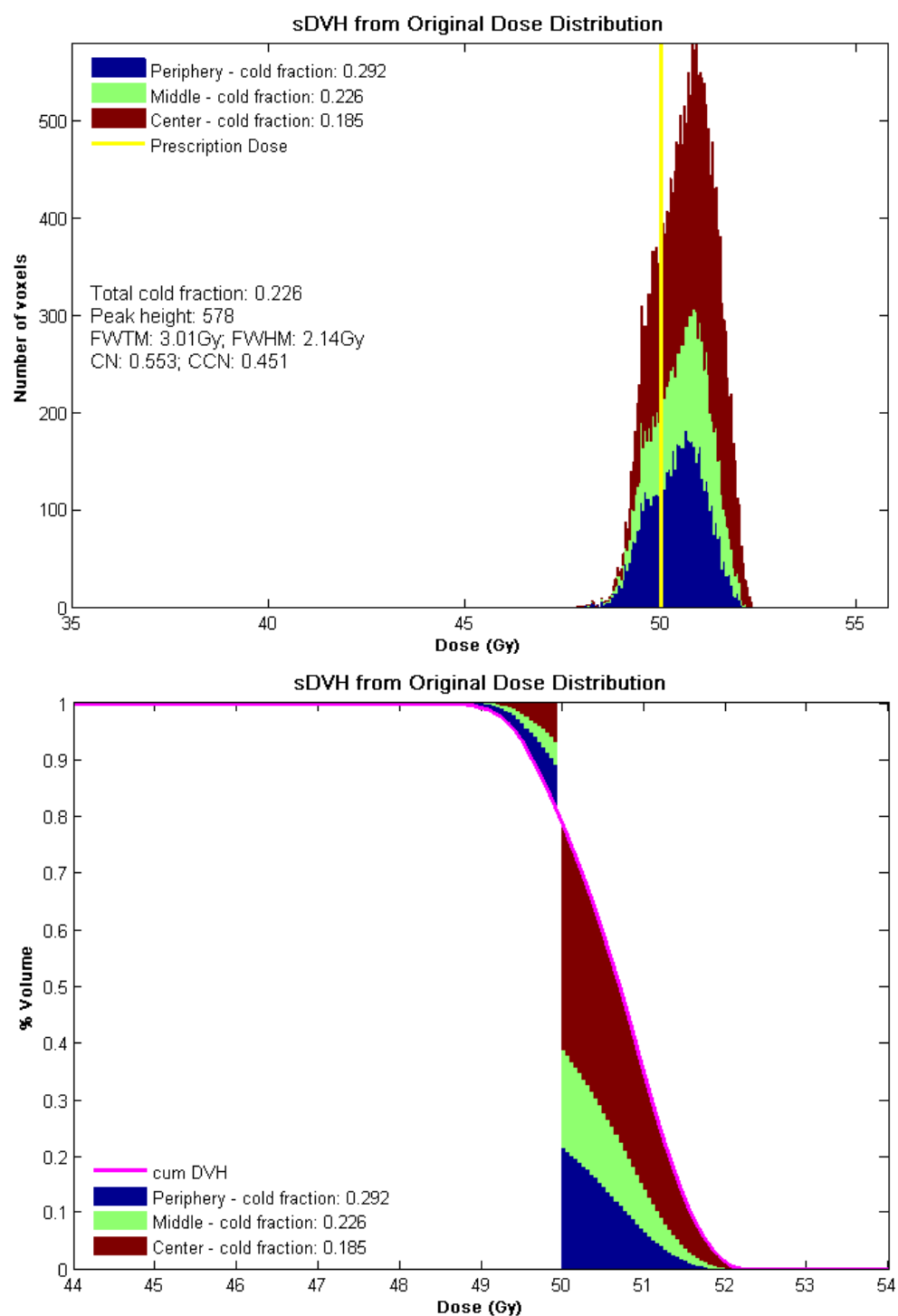


Figure 26: Typical sDVH. Top: differential sDVH; bottom: cumulative sDVH.

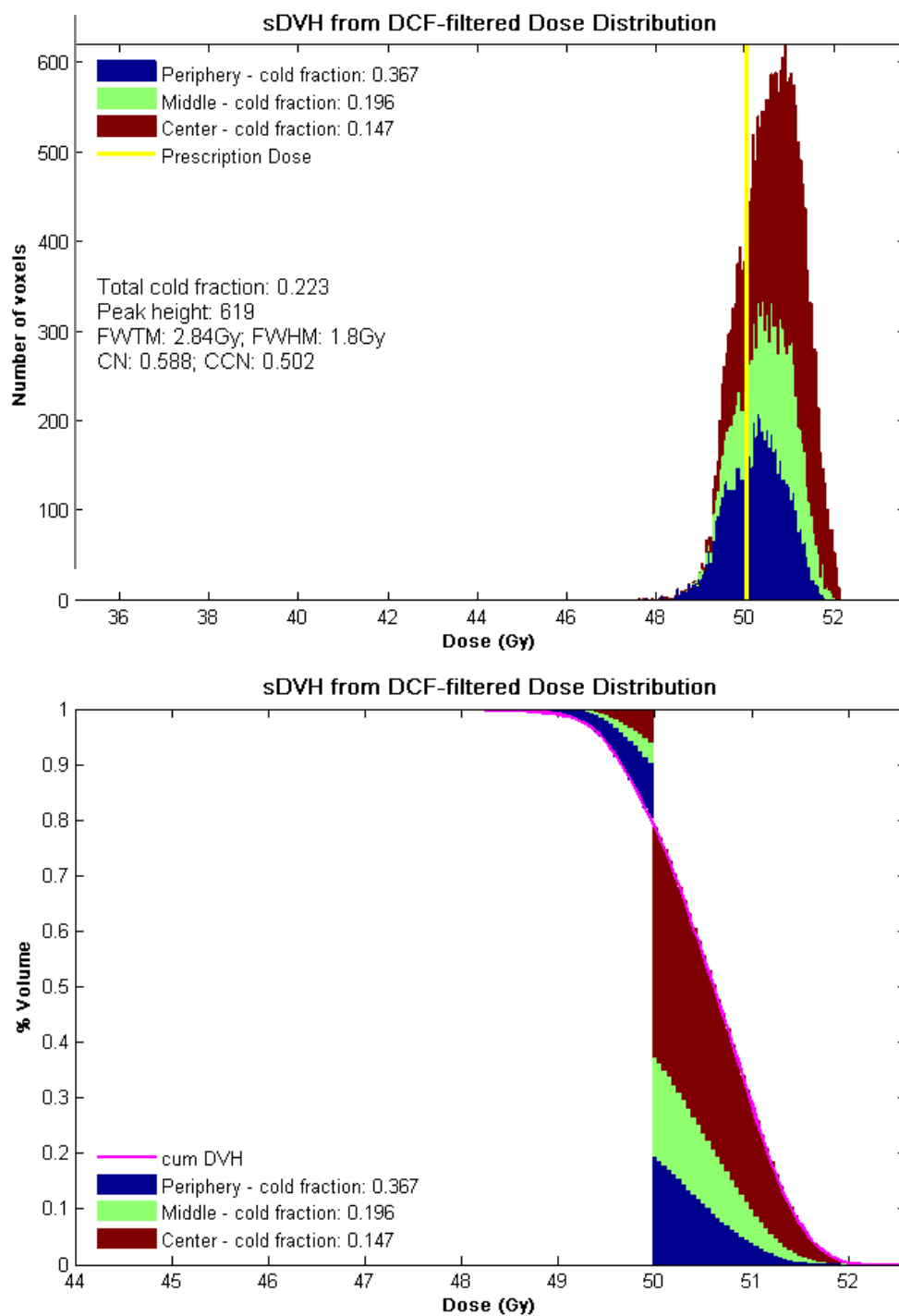


Figure 27: Typical sDVH. Top: differential sDVH; bottom: cumulative sDVH.

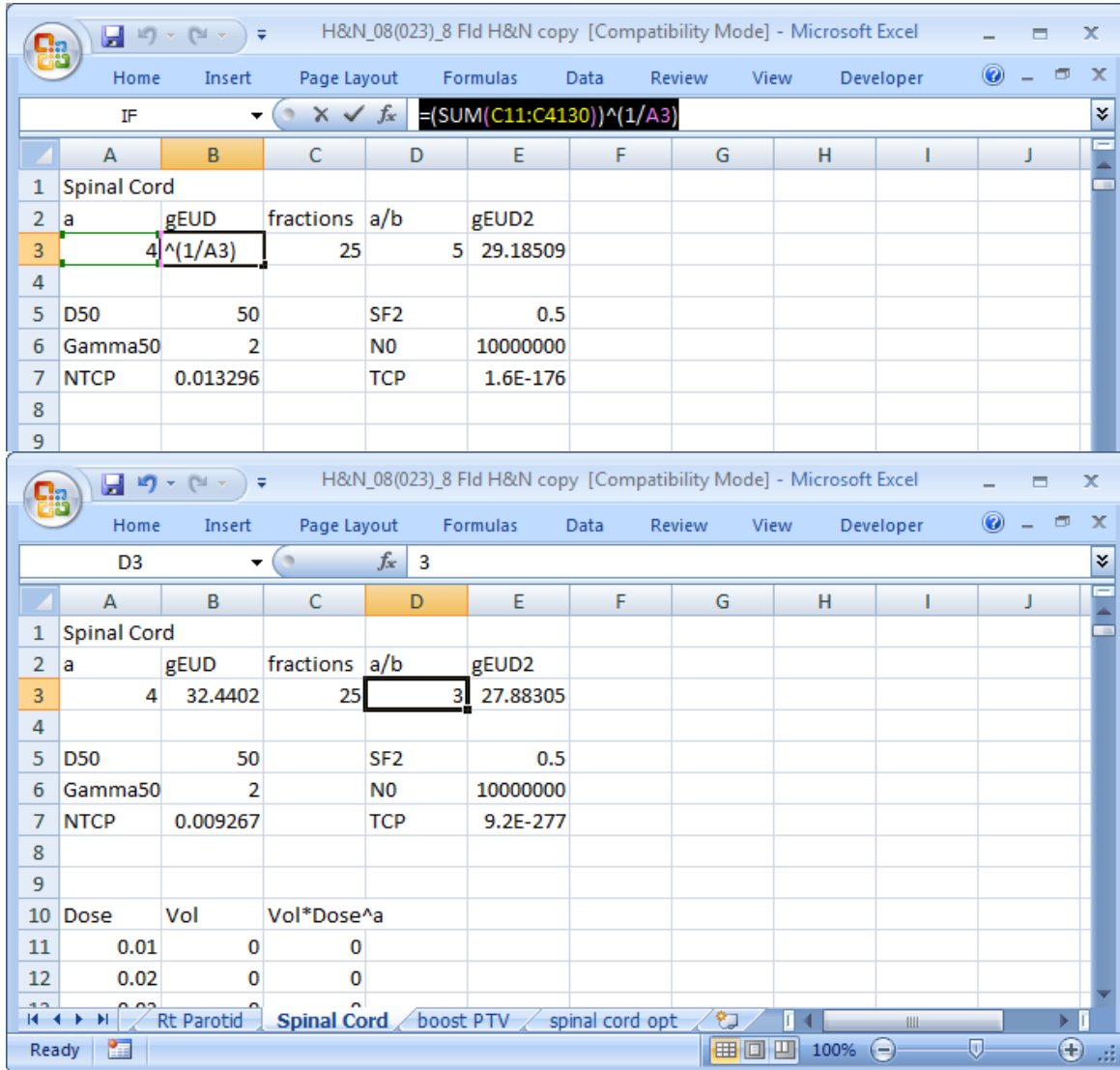


Figure 28: Excel BioEval function demonstration. The Excel workbook is created in several second by the SABER software. All equations are programmed by SABER. For example, the α/β value for spinal cord was changed from 5 to 3. All results were instantly updated.

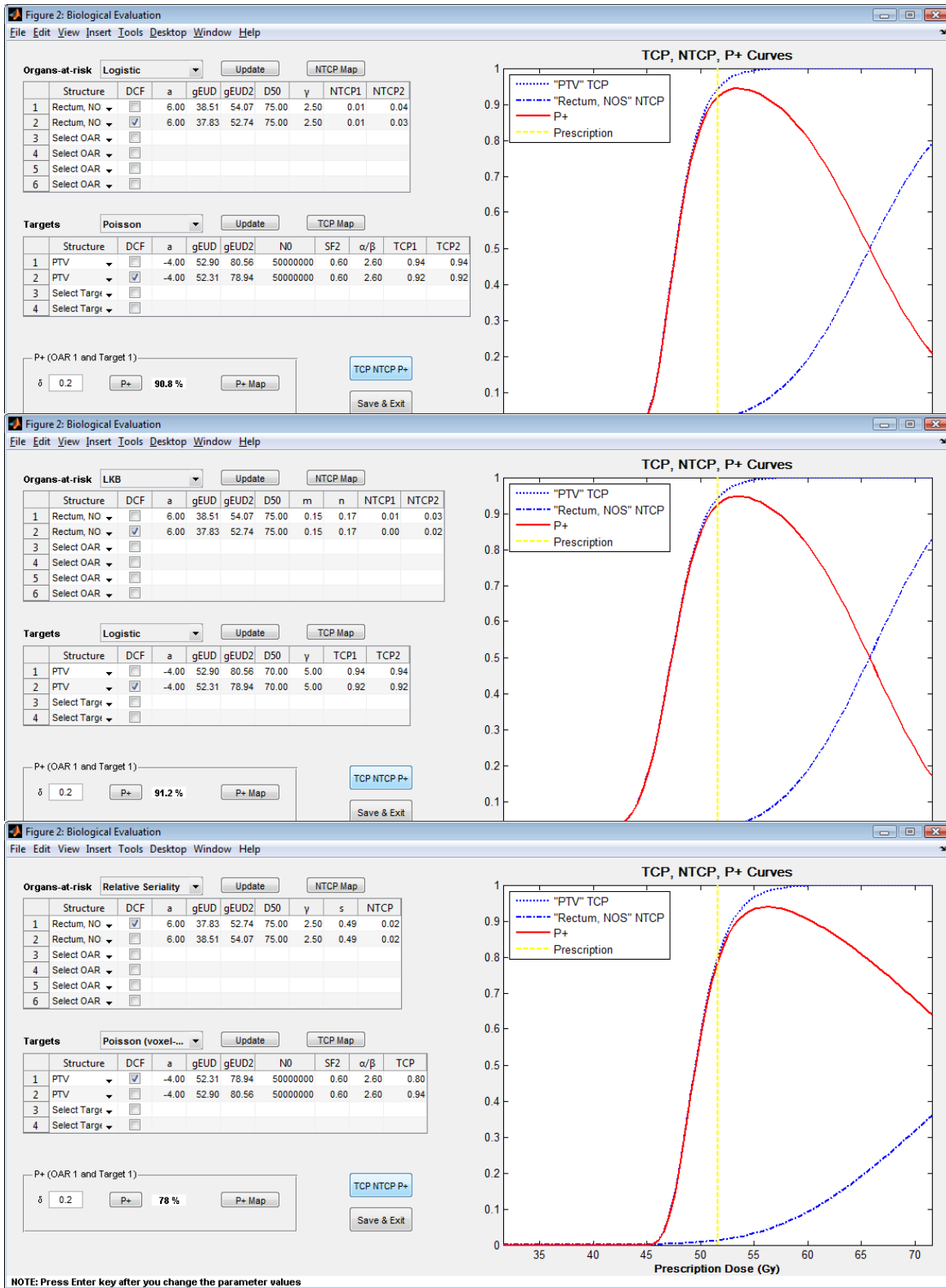


Figure 29: SABER's "Biological Evaluation" module. The screenshots shown here are just three examples of different combinations of existing TCP and NTCP models.

LDHRS

Please provide all parameters for the structures listed below
- based on Induced Repair (IR) model

	Structure	α_r	β_{ir}	$\alpha_s (>= \alpha_r)$	d_c
1	Bladder, NOS				
2	Body				
3	Body_opt				
4	CTV				
5	PTV				
6	PTV-2Voxels				
7	PTV_SmallM...				
8	Rectum, NOS				
9					
10					

OK Cancel

Figure 30:Parameter input window for low dose hypersensitivity (HRS) using the IR model, which replaces the LQ model for converting physical dose to EQD₂.

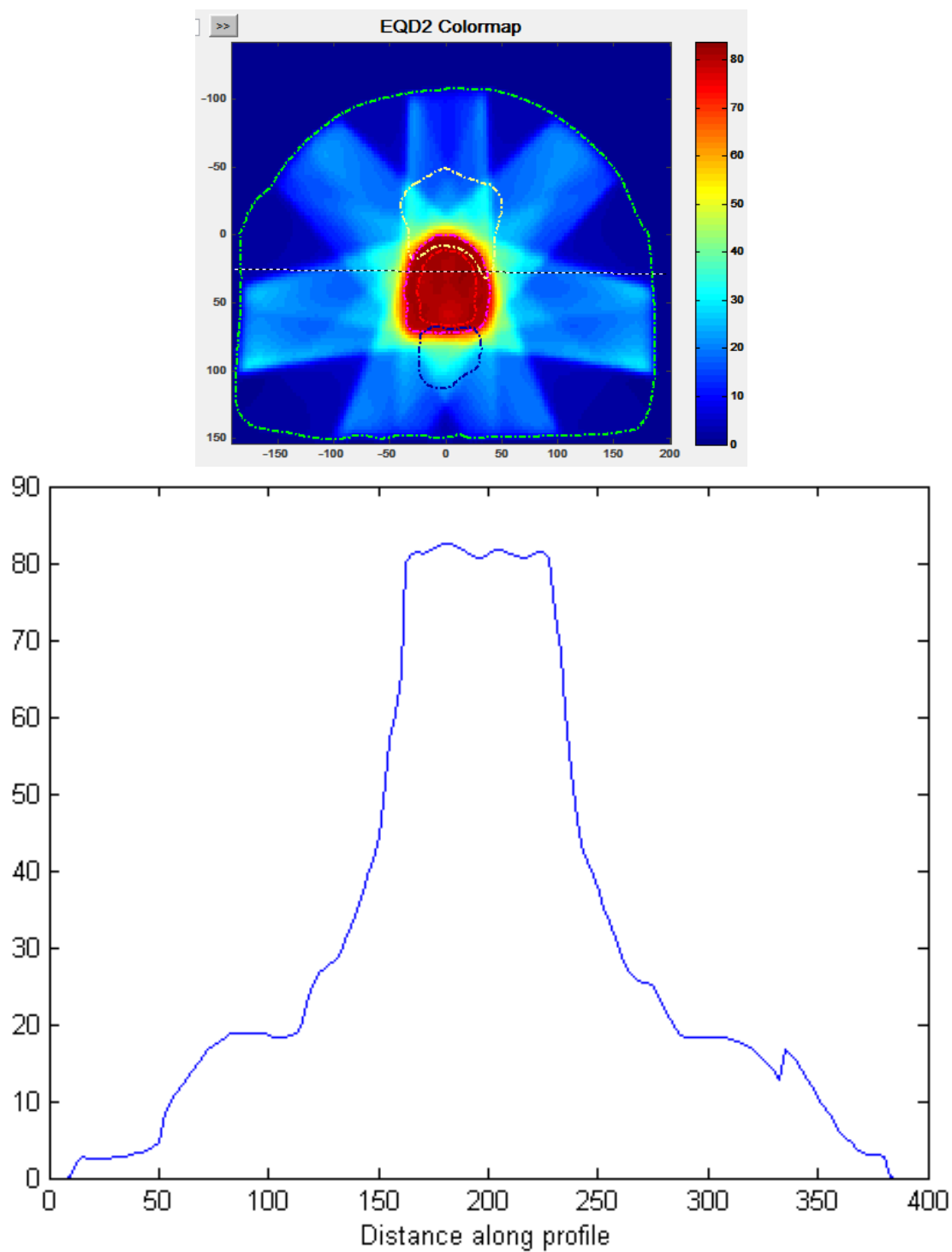


Figure 31: Example of using the dose profile function. The profile can be measured from a physical dose colorwash figure or an EQD2 colorwash figure.

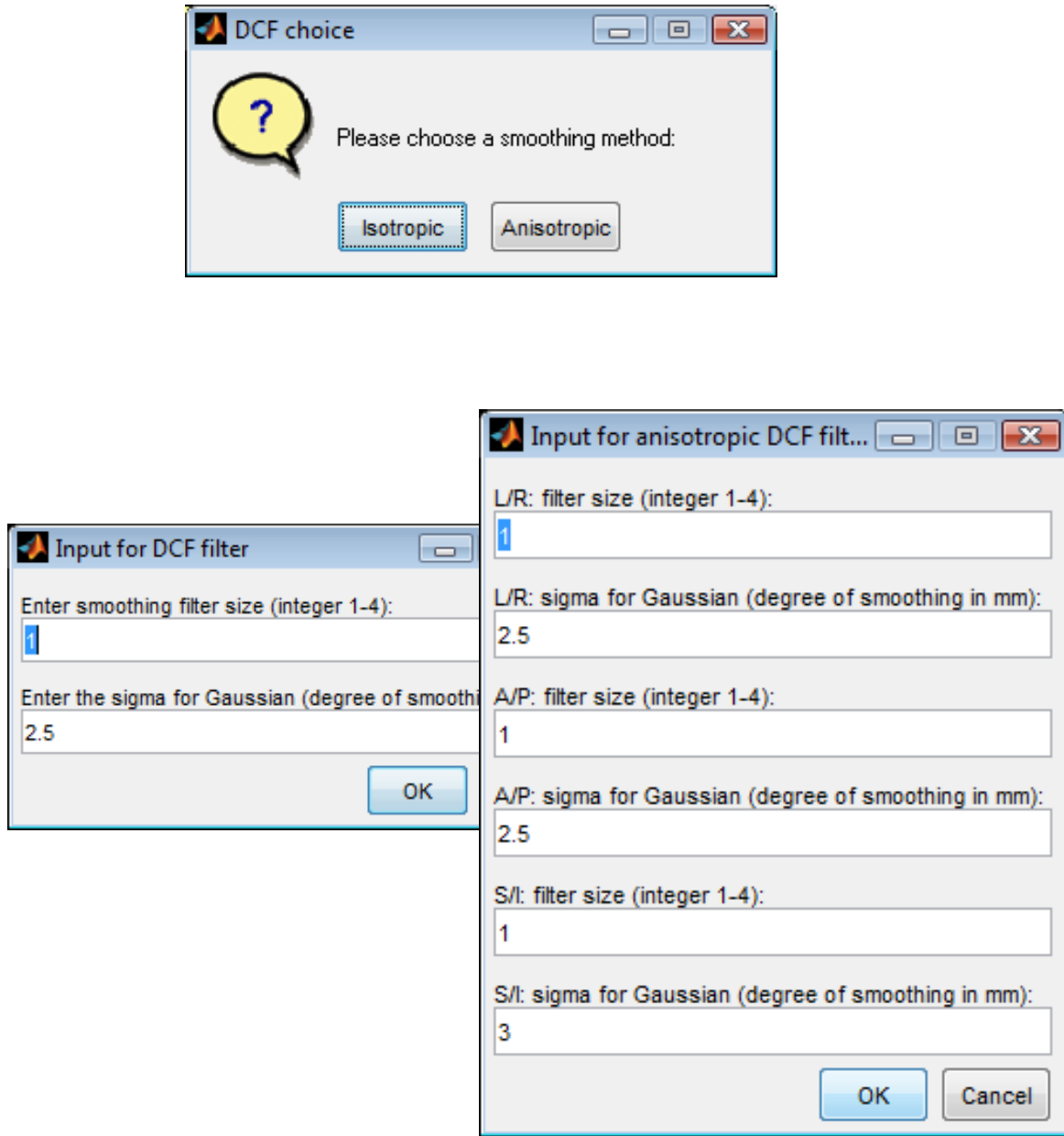


Figure 32: Window for changing DCF preference – isotropic DCF or anisotropic DCF. User is able to define/change filter size and σ value.

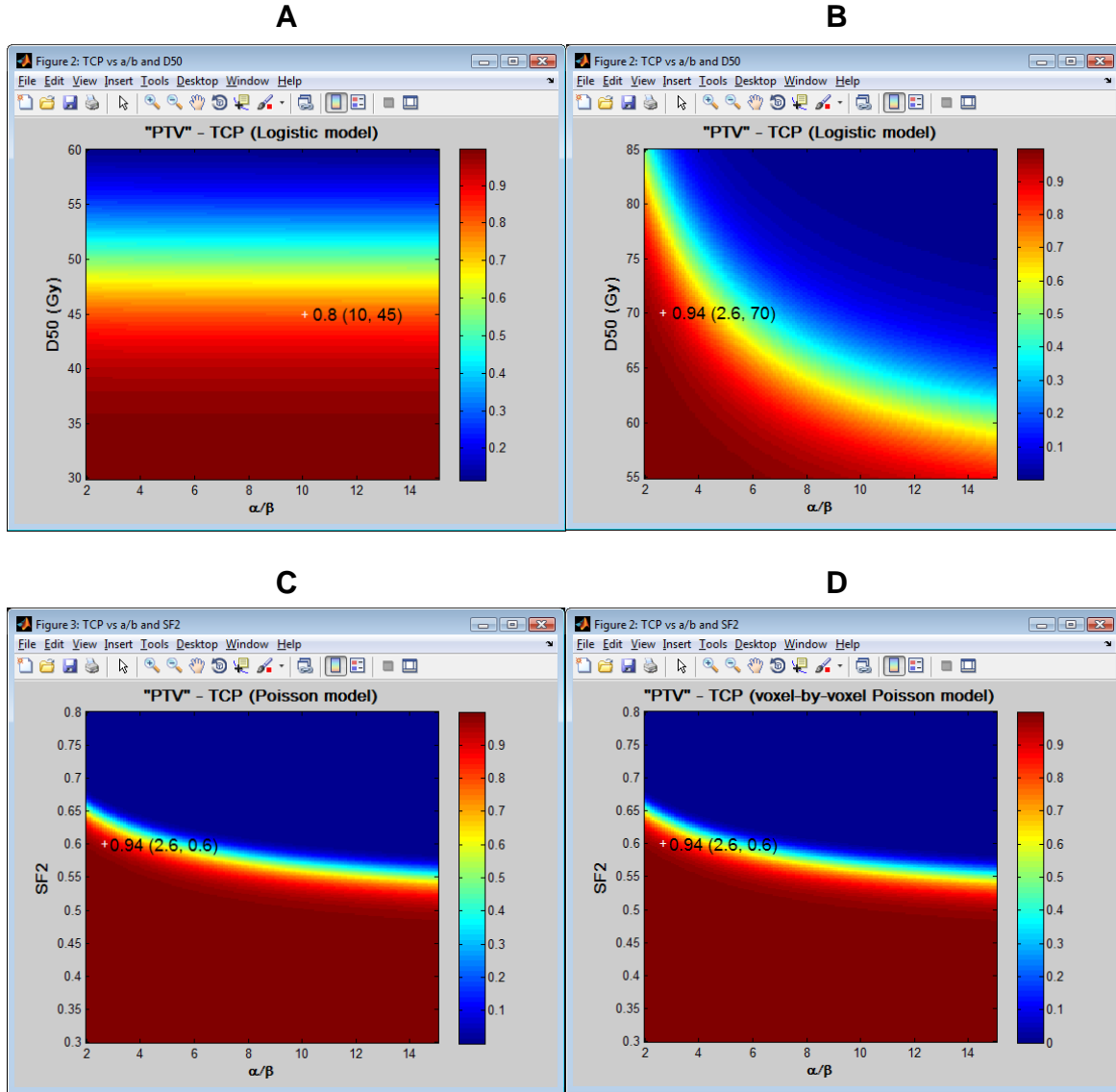


Figure 33: Multi-variable TCP figures. Color scale represents TCP values. A) Logistic TCP as a function of D₅₀ and α/β for a 2Gy/fraction treatment. TCP values do not change with respect to α/β values. B) Logistic TCP as a function of D₅₀ and α/β for a hypofractionated treatment (>2Gy/fraction). C) Poisson TCP as a function of SF2 and α/β for the same treatment as in B. D) Voxel-by-voxel Poisson TCP as a function of SF2 and α/β for the same treatment as in B.

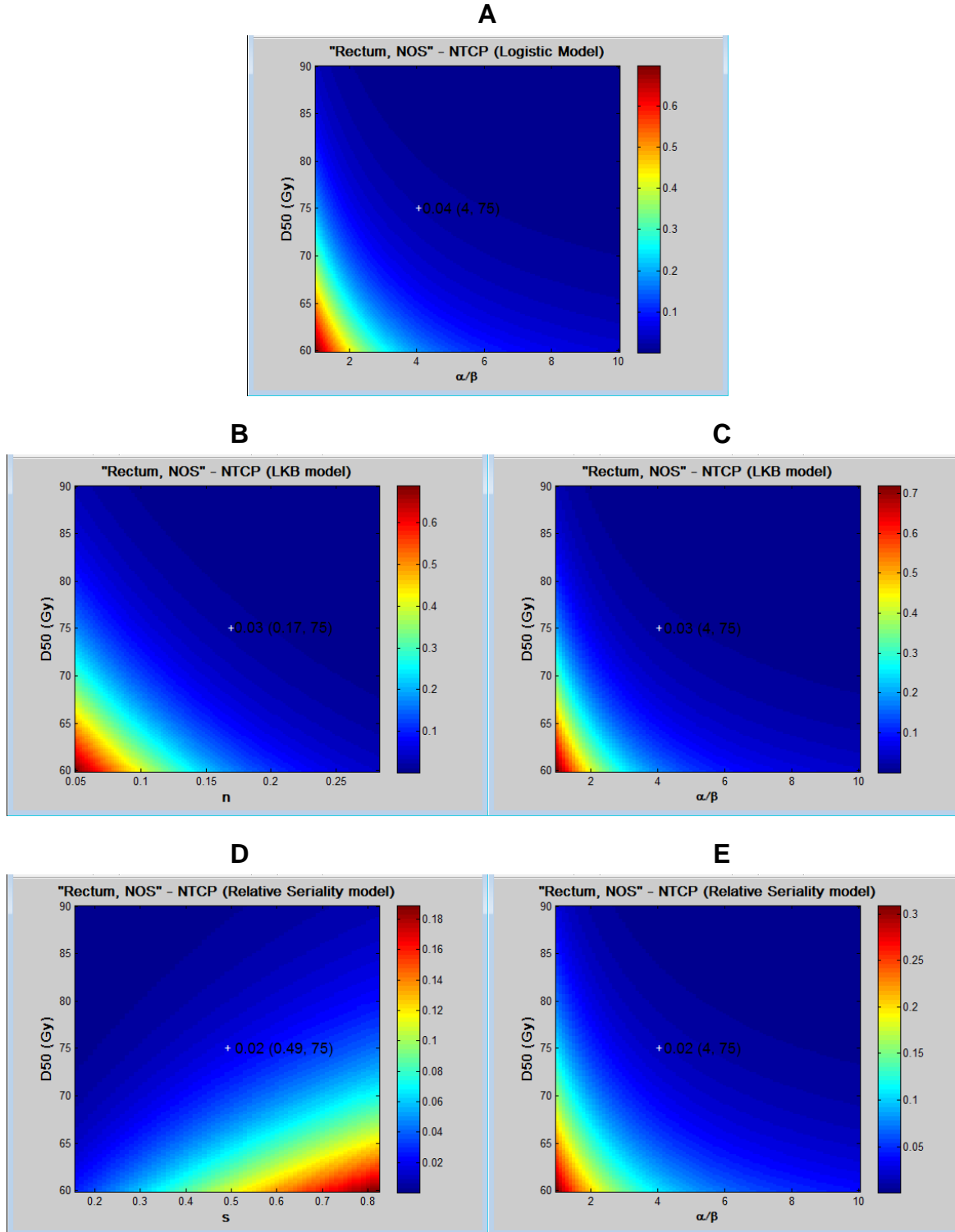


Figure 34: Multi-variable NTCP figures. Color scale represents NTCP values. A) Logistic NTCP as a function of D_{50} and α/β . B) LKB NTCP as a function of D_{50} and n . C) LKB NTCP as a function of D_{50} and α/β . D) relative seriality NTCP as a function of D_{50} and s . E) relative seriality NTCP as a function of D_{50} and α/β . All figures are generated from one hypo-fractionated prostate treatment plan.

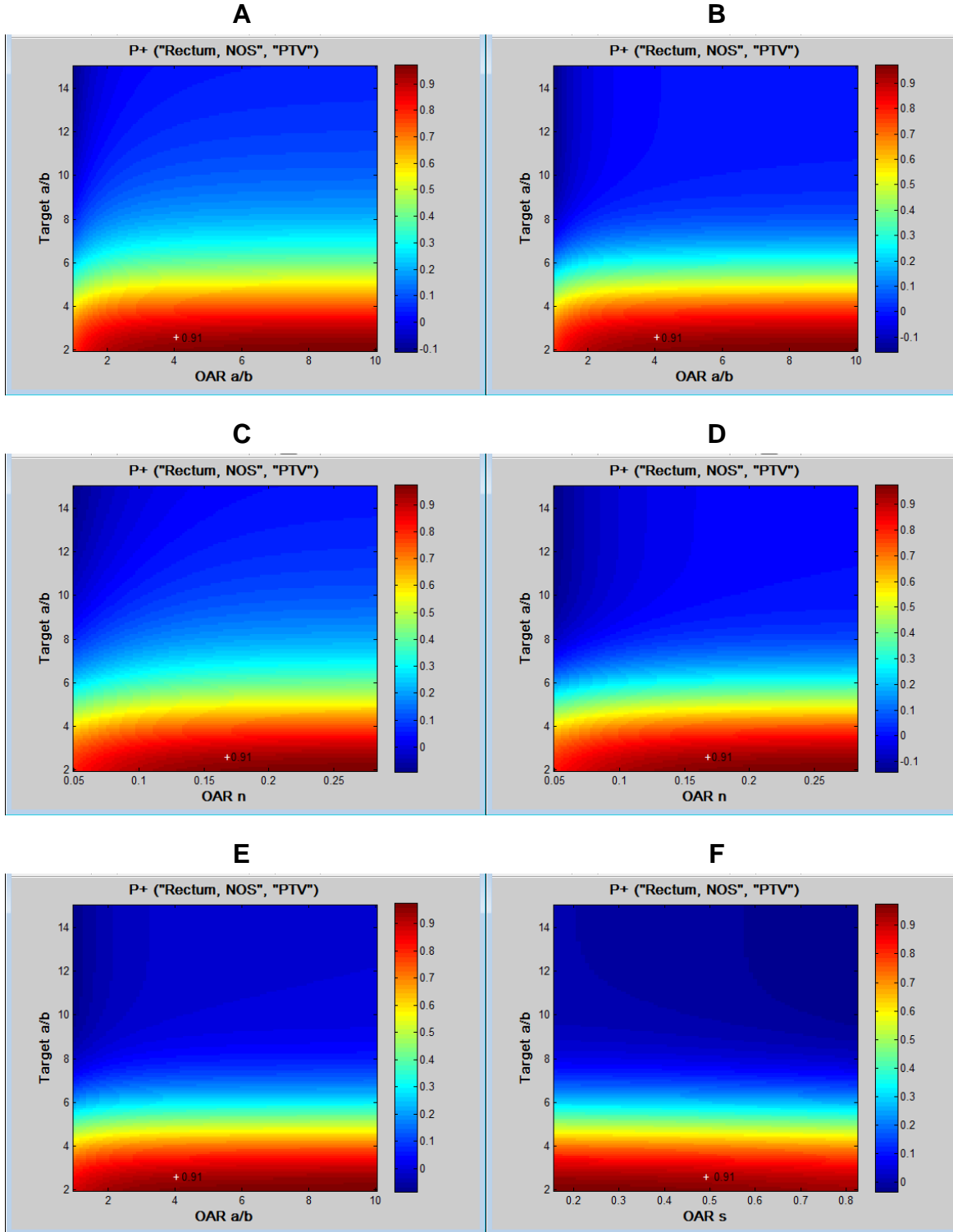


Figure 35: Multi-variable P^+ figures. Color scale represents P^+ values. As shown are examples of P^+ as a result of A) Logistic NTCP (α/β) and logistic TCP (α/β); B) Logistic NTCP (α/β) and Poisson TCP (α/β); C) LKB NTCP (n) and logistic TCP (α/β); D) LKB NTCP (n) and Poisson TCP (α/β); E) relative seriality NTCP (α/β) and voxel-by-voxel Poisson TCP (α/β); F) relative seriality NTCP (s) and voxel-by-voxel Poisson TCP (α/β).

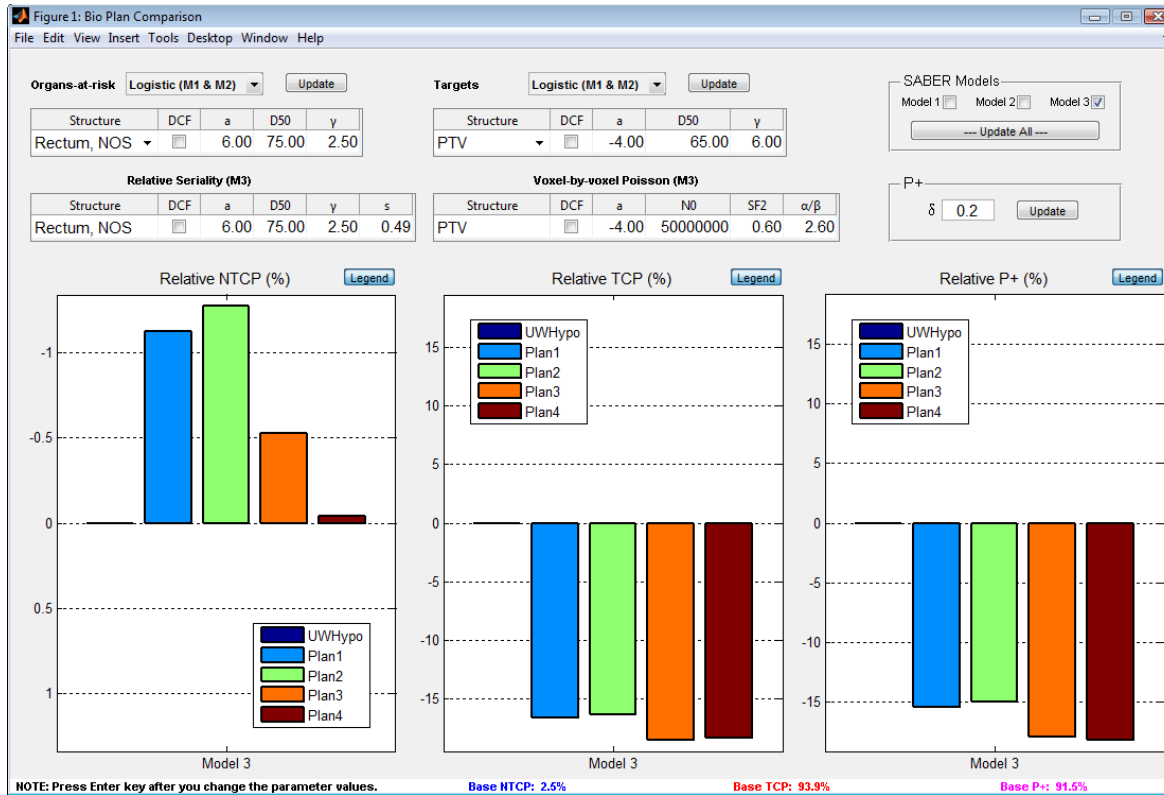


Figure 36: "Bio Plan Comparison" module. By default, only SABER Model 3 is selected for simplicity. Absolute NTCP, TCP and P+ values for the base plan are provided at the bottom.

CHAPTER 4

Discussion and Conclusions

In Model 1, gEUD is calculated first and then the LQ model is applied to normalize the gEUD to 2Gy fractions which becomes gEUD₂. While in Model 2, the order is switched. We first apply the LQ model to convert physical voxel doses to 2Gy fractions and then calculate gEUD which is actually the gEUD₂ because all voxel doses have been normalized to 2Gy fractions. The change of the order would result in different results of gEUD₂. To illustrate that, let us look at a simple mock example. Suppose half an organ receives 60 Gy and the other half receives 30 Gy in a 30 fraction course of treatment. Assume $\alpha/\beta = 3$ Gy and $a = 2$. By using Model 1, gEUD can be calculated:

$$\text{gEUD} = \left(\frac{1}{2} (60^2 + 30^2) \right)^{1/2} = 47.43\text{Gy}$$

Normalize it to 2Gy fractions:

$$\text{gEUD}_2 = 47.43 \left(\frac{47.43/30 + 3}{2 + 3} \right) = 43.46\text{Gy}$$

Now if we apply the Model 2, the physical voxel doses are converted to 2Gy fractions first. So the half of organ that receives 60Gy remains 60Gy, but the other half of the organ that receives 30Gy becomes $30 \left(\frac{30/30+3}{2+3} \right) = 24\text{Gy}$. Then we can derive gEUD₂ from the EQD₂ values:

$$\text{gEUD}_2 = \left(\frac{1}{2} (60^2 + 24^2) \right)^{1/2} = 45.69\text{Gy}$$

In the above example, the gEUD₂ results have over 2Gy difference between the two models. One can then apply NTCP models to calculate complication probability. For example using the LKB model and assuming D₅₀ is 60Gy and m is 0.25, we can get

$$\text{NTCP}_{\text{Model 1}} = \frac{1}{2\pi} \int_{-\infty}^{\frac{43.46-60}{0.25 \times 60}} e^{-\frac{x^2}{2}} dx = 13.5\%$$

$$\text{NTCP}_{\text{Model 2}} = \frac{1}{2\pi} \int_{-\infty}^{\frac{45.69-60}{0.25 \times 60}} e^{-\frac{x^2}{2}} dx = 17.0\%$$

We can do a similar mock example for target volumes. Suppose the target has 1000 voxels and 950 voxels receive 70Gy in a 35 fraction course of treatment and the rest of the target receives 50Gy. Assuming $\alpha/\beta = 10\text{Gy}$ and $a = -10$, the gEUD2 calculated from Model 1 and Model 2 would be 63.3Gy and 62.1Gy, respectively. The results can then translate into different TCPs.

Depending on the nature of the spatial dose distribution, the relative effect of the DCF will vary. For cases in which dose distributions are homogeneous DCF may have only minor effects or may even be negligible, while for cases in which dose distributions are very inhomogeneous the effect of DCF may be significant. Moreover, the effect and its direction (whether it increases or decreases gEUD and thus TCP or NTCP), depends on the volume, the dose level, and the spatial distributions of cold/hot spots (Figure 37 and Figure 38). Plans that have similar DVHs may respond to the application of DCF differently (Figure 38), thus resulting in substantially different predictions for TCP and NTCP and associated changes in relative plan ranking.

The sDVH is a simple and intuitive way to restore spatial information back into the DVH format. From the sDVH, we can immediately see the distributions of under-dosed voxels across chosen regions and whether and how many of such voxels exist in regions where gross disease has been identified or is more likely to reside. For the example shown in Figure 26 and Figure 27, the three regions are arbitrarily selected for illustrative purposes. If, for example, we have clinical bases for assuming that the center region of a

tumor is likely to have higher malignant cell density than the periphery, use of the sDVH will enable us to easily select a plan with a preferable spatial dose distribution. In cases such as Bijl's *split-field irradiation*⁴⁵ on the rat cervical spinal cord where same total length of cord was irradiated but with different spacings between the split fields, the sDVH alone cannot differentiate between different plans. However, the application of the DCF concept prior to calculation of the sDVH will allow differentiation.³⁴

In addition to its application for plan evaluation purposes, the sDVH also has potential applications for plan optimization. Figure 39 shows two plans with virtually identical target and OAR DVHs. Significant differences in either target or OAR DVHs would make the clinical decision relatively straightforward however, in the absence of such differences, an investigation of the spatial distribution of the calculated absorbed dose is warranted. For the example in Figure 39, Plan 3 is an IMRT plan optimized using regular dose volume constraints. Plan 4 is then further optimized manually using the sDVH concept. From sDVH results (Figure 40), we readily observe differences in the number of under-dosed voxels in critical regions (under-dosed fraction in center region: 5% in Plan 3 versus 0.05% in Plan 4) and can choose the plan that is more favorable with respect to the spatial dose distribution. DVH-based optimization lacks objectives that regulate the location of under-dosed voxels in the target. However, optimization incorporating sDVH has the capability of reorganizing an inhomogeneous dose distribution in an attempt to improve the spatial dose distribution. One might question whether such changes are clinically relevant. This question is not easily answered and is similar to many of the current questions regarding actual realized clinical advantages from any IMRT optimization techniques. However, even if only a relatively small difference is observed,

we would like to push the plan in an apparently favorable direction – this is the process of "optimization". Application of sDVH requires only the target contours which are already available in the current optimization algorithm in the Eclipse TPS, and the creation of the different regions can be easily automated in most cases.

In the workbook created by the “Excel BioEval” function, all structures have both TCP and NTCP programmed. When looking at one specific structure, the user would then ignore either TCP or NTCP depending on whether the structure is an OAR or target. While we could require the user to specify the structure type so that only TCP or NTCP is generated, we prefer not to require any input from the user since the original motivation for this function is to provide simple and quick results. For the same reason, we choose the Excel format because it is accessible, programmable and universally available.

The more comprehensive “Biological Evaluation” module provides additional options. The user can choose any of the different models from the drop-down lists. The DCF can be turned on or off with a simple mouse click, making it extremely useful for visually evaluating the effect of DCF application. The voxel-by-voxel TCP model makes it feasible to incorporate spatial variations of clonogen densities (n), radiosensitivities ($SF2$), and fractionation sensitivities (α/β) when those data are available. SABER is capable of retaining the spatial variations as the dose information is processed at the voxel level rather than using dose information that has been distilled into simpler forms. This framework provides the potential to improve our understanding and prediction of the effects of radiation dose distributions with the biological information we have now but will also allow even further improvement if additional biological information such as clonogen density, hypoxia, and spatial variations in biological parameters become known.

The multi-variable TCP, NTCP, or P+ figure covers large parameter ranges and provides information on how sensitive the probability is to the assumed parameters. A wealth of biological data describing the effects of radiation on normal tissues has recently become available in the form of the QUANTEC report (**QU**antitative **A**nalyses of **N**ormal **T**issue **E**ffects in the **C**linic) and this data is being incorporated into the software's build-in library to provide more clinically relevant results.⁸⁵ In Figure 35, only six P+ figures are presented. In fact, SABER can provide such P+ figures as a result of any TCP (Figure 33) and NTCP (Figure 34) combination.

In spite of that there are large uncertainties associated with the biological parameters in TCP, NTCP and P+ predictions, the relative magnitudes are valuable for plan comparison purposes. The “Bio Plan Comparison” module provides capabilities to analyze and compare multiple treatment plans for the same patient (Figure 36). The module integrates all three SABER models and deploys all existing TCP/NTCP/P+ models as presented in the “Biological Evaluation” module. For simplicity, only the voxel-by-voxel Model 3 is selected by default (Figure 36). Users are free to select any or any combination of the three SABER models for plan comparison. For example in Figure 36, all three models are selected. The voxel-by-voxel Model 3 tends to predict a lower TCP which is expected assuming individual voxel TCPs are multiplicative. This is in comparison to gEUD methods which calculate TCP over multiple voxels.

An important result in the example of Figure 41 is that the plan rankings changed from Model 1 to Model 2 or 3 if we sort plans based on the NTCPs of the rectum. Based on SABER Model 1 (voxel dose \rightarrow structure gEUD \rightarrow structure gEUD₂ \rightarrow NTCP), the UWHypo plan yields the least NTCP. However, if one sorts the plans using either Model 2

(voxel dose \rightarrow voxel EQD₂ \rightarrow structure gEUD₂ \rightarrow NTCP) or Model 3 (voxel dose \rightarrow voxel EQD₂ \rightarrow NTCP), the plan rankings are altered. The Plan 2 turns to yield the least NTCP and UWHypo becomes the worst. Although the NTCP differences between the plans are relatively small in this example (<2%), it proves that the choice of biological models can change the biological results. If we compare the results from the top figure (without DCF) with the bottom one (with DCF) in Figure 41, we found another important result, which confirms our discussion about the effect of DCF in the beginning of this section. The DCF does alter the plan ranking in this example. So the effect of cell migration, setup uncertainty, inter- and intra-fraction motions should be carefully examined and be taken into account when making clinical decisions based on predictors such as gEUD, TCP, NTCP and P+. The biological plan evaluation is much more complex than evaluations based solely on physical dose. And one should be cautious when making clinical decisions based on one radiobiological model.

We have developed a software tool named SABER which provides the treatment planner with significantly more information to evaluate radiotherapy plans. The DCF concept can be used to simulate the effect of random or systematic motions and thus integrate such effects into the evaluation. The sDVH concept incorporates spatial information back into the DVH format. Multiple biological functions and models are provided to facilitate greater understanding of the effects of planned and delivered dose distributions as well as the ability to better predict outcome. SABER incorporates both spatial and biological information into plan evaluation and provides a framework for incorporating additional biological information into the plan comparison and optimization process when this information is available. This may significantly alter the predicted

outcome and thus the choice of treatment plan. Thus SABER can help create more optimum radiotherapy treatment plans and more accurately predict treatment outcome.

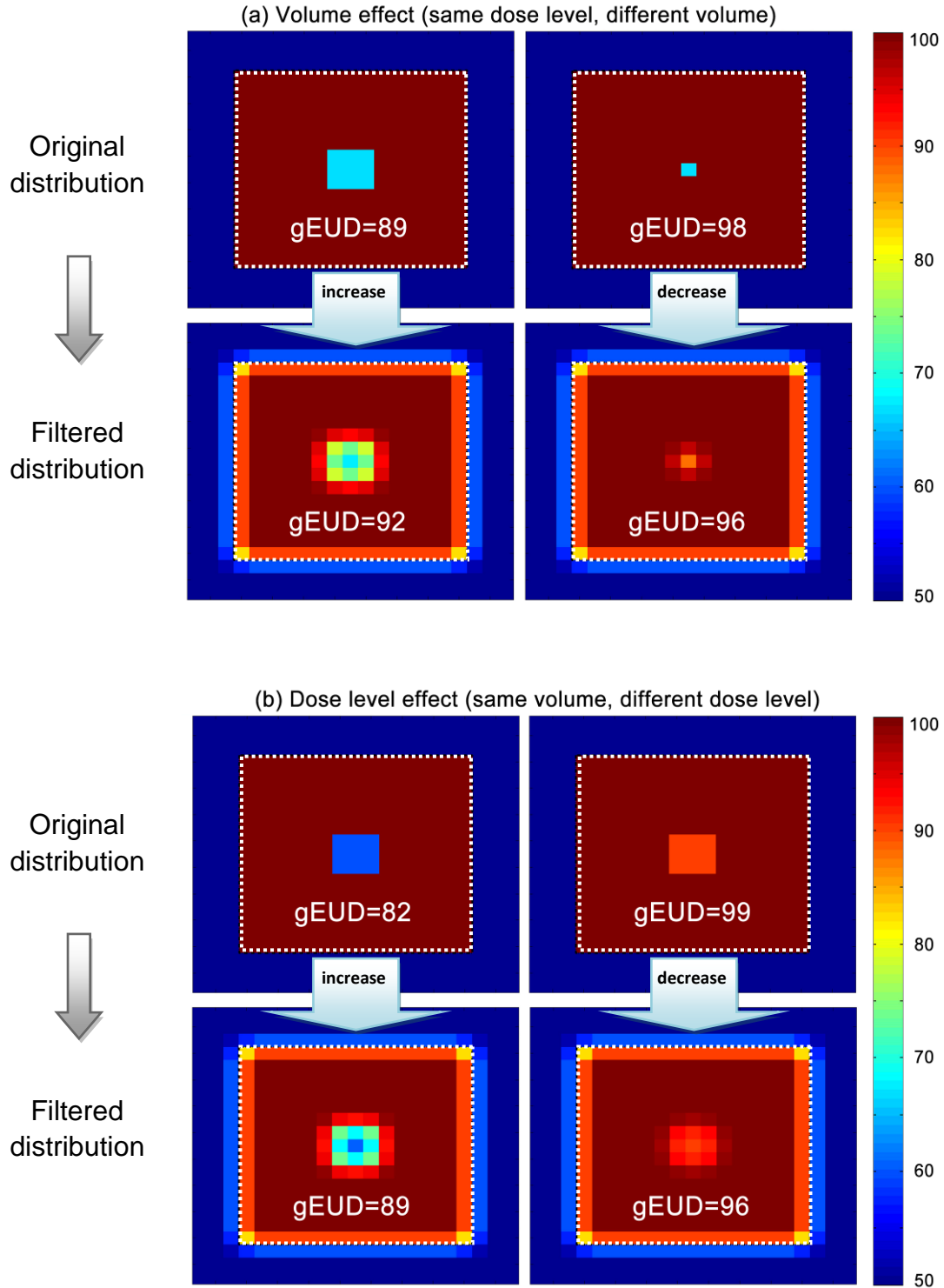


Figure 37: Illustration of DCF effect on different static dose distributions. The dotted white boxes are the target contours. Inside the contour, dose is 100% except the under-dosed regions. Outside, dose is 50%. The σ is chosen as one pixel. (a) Volume effect: cold spots have same level of dose but different volume (b) Dose level effect: cold spots have same volume but different level of dose. DCF could lower a target's gEUD if the dose falls sharply at the edges of the target.

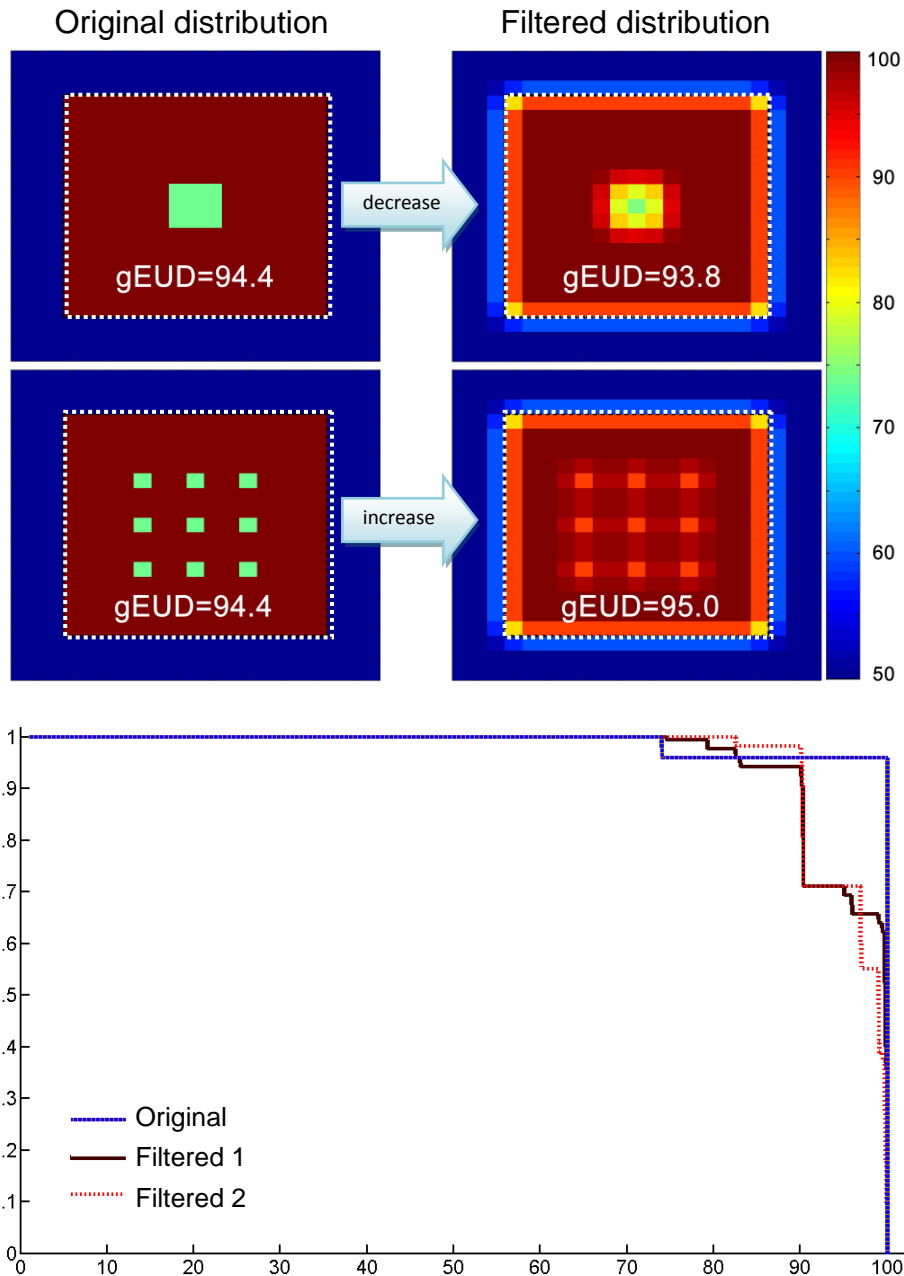


Figure 38: Illustration of DCF effect on static dose. Top: on the left are static doses with the same DVH but different spatial dose distribution; on the right are DCF filtered dose distributions. Bottom: DVHs of the original dose distribution and the filtered dose distributions.

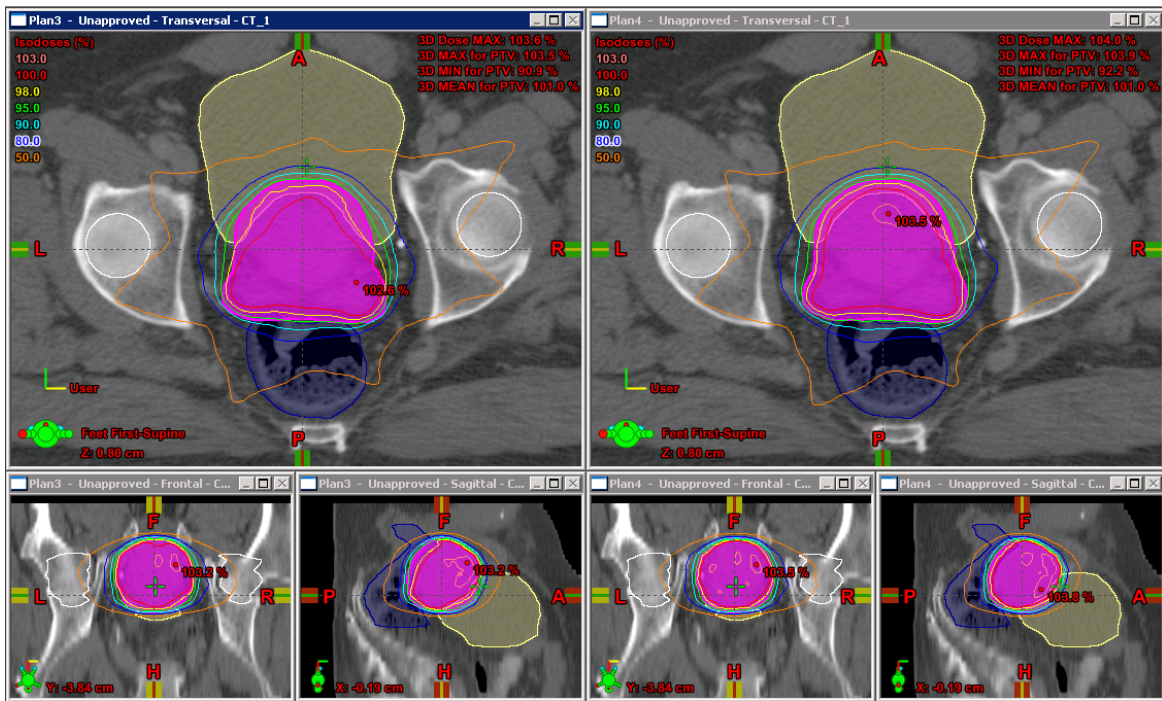
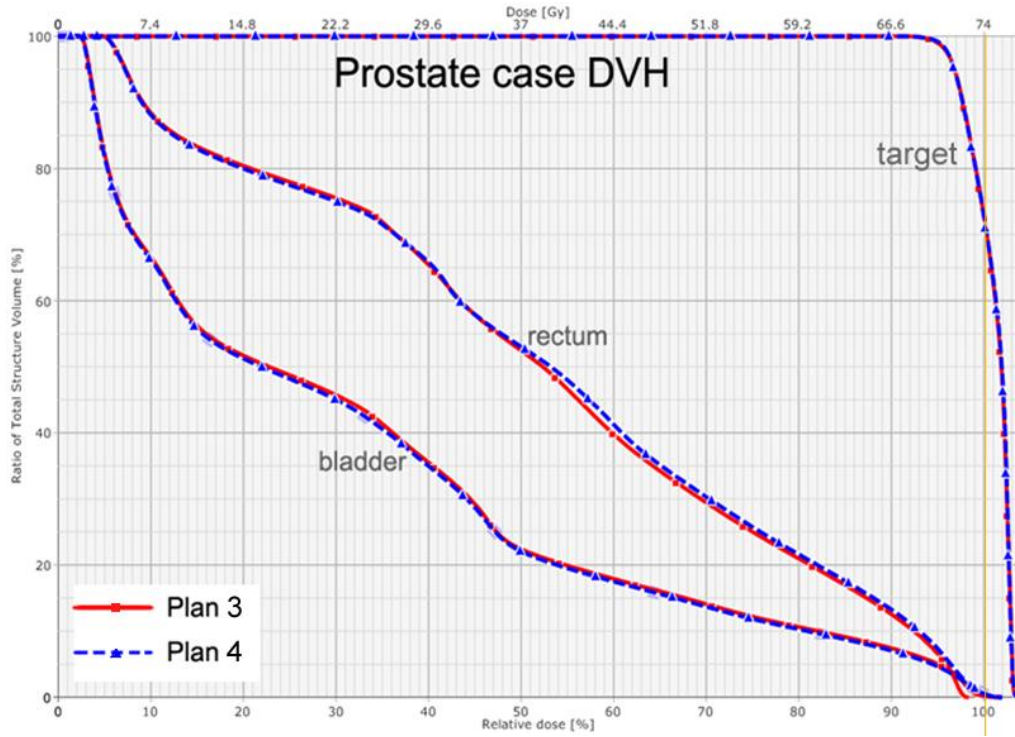
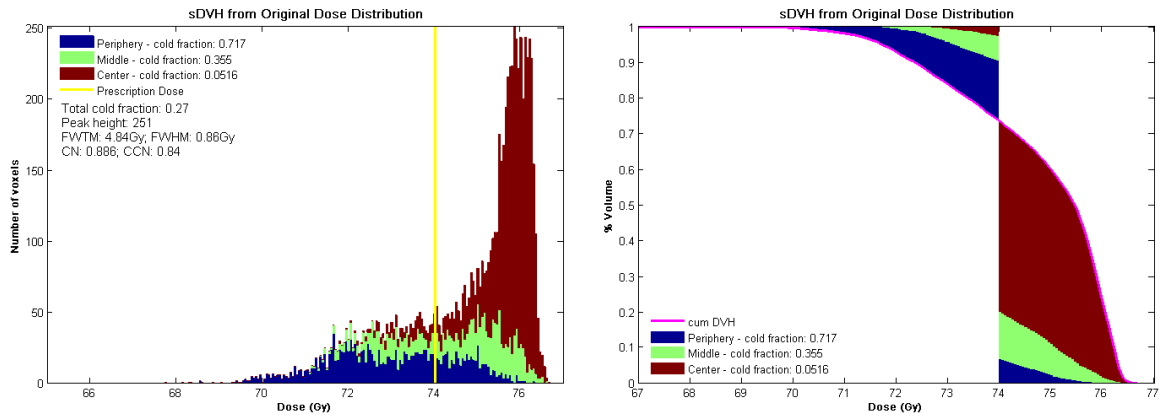


Figure 39: Two treatment plans from a prostate case. Top: DVHs. Two treatment plans have virtually identical target DVHs and very close OAR DVHs. Bottom: Dose distribution comparison.

Plan 3 sDVH



Plan 4 sDVH

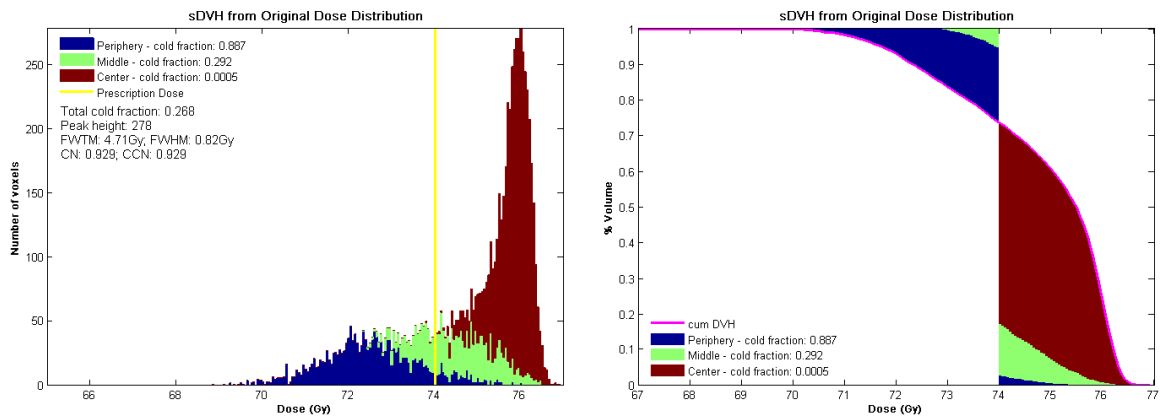


Figure 40: The sDVH for the two prostate treatment plans (Figure 39). Top: differential sDVH and cumulative sDVH for Plan 3. Bottom: differential sDVH and cumulative sDVH for Plan 4.

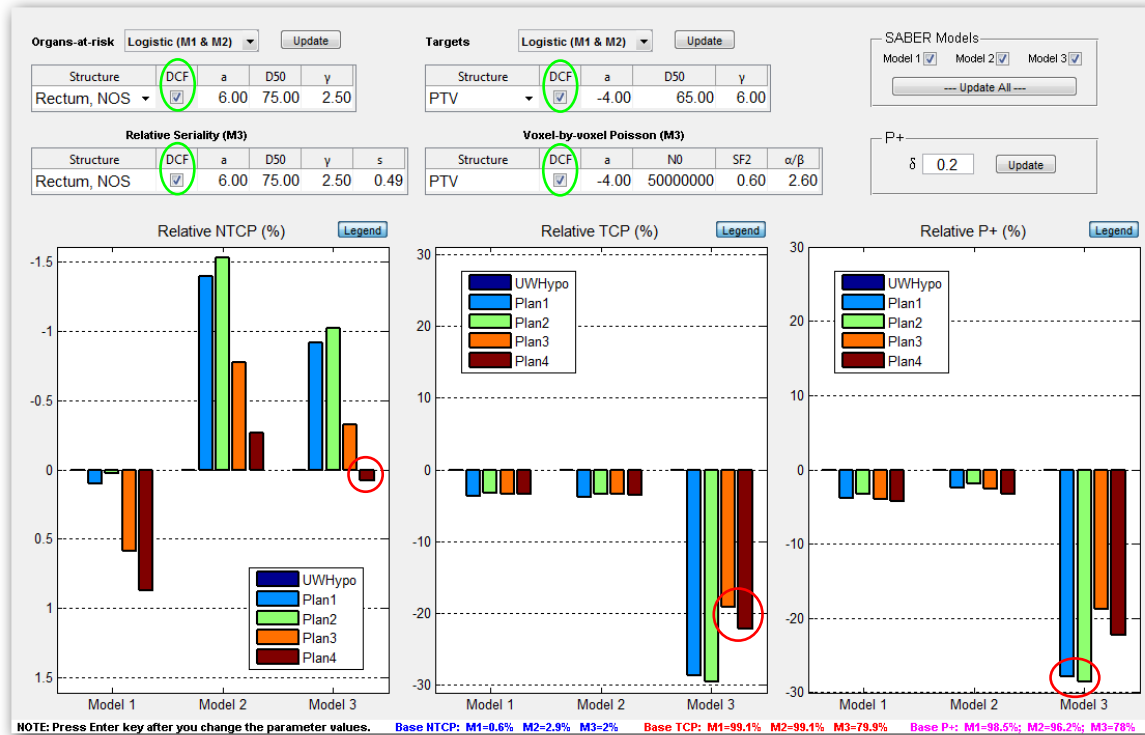
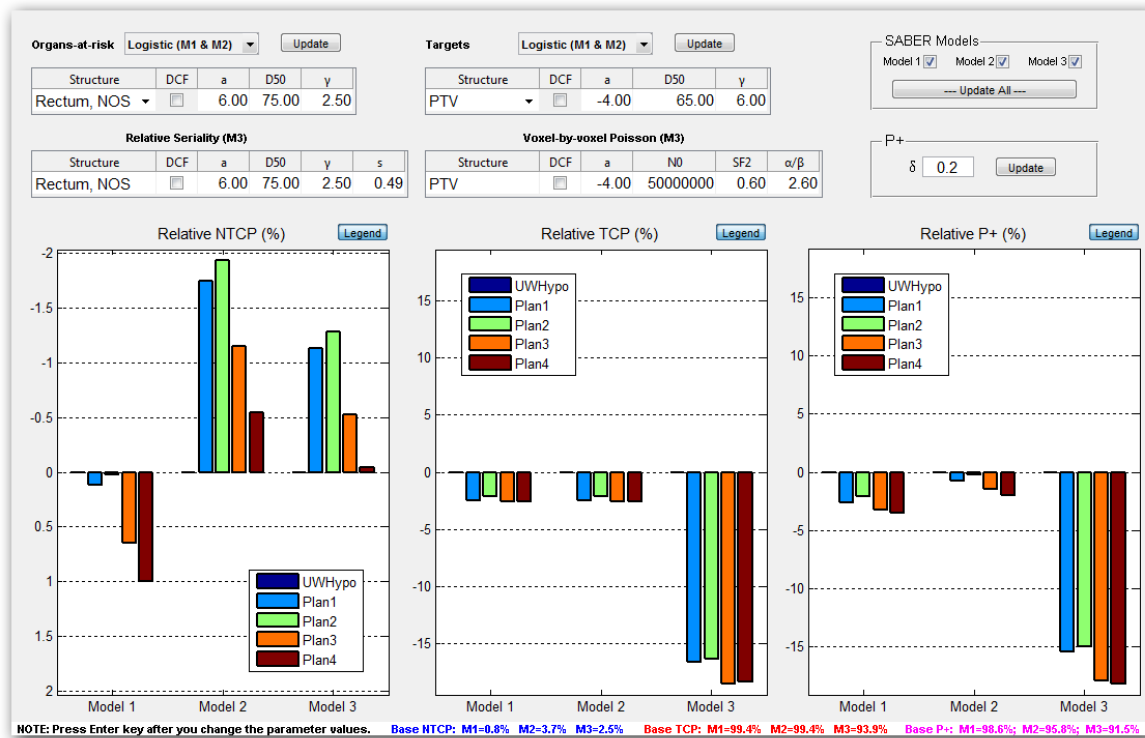


Figure 41: “Bio Plan Comparison module”: Top: DCF is OFF; bottom: DCF is ON. All three SABER models are selected. Base values in each SABER model are the absolute NTCP/TCP/P+ values of the first plan, i.e. the “UWHypo” as in this example. In this example, the plan rankings based on NTCP are different from the three models, and application of DCF also alters the plan rankings.

CHAPTER 5

Future Work - Technology versus Biology

As we discussed in the introduction, the physical aspects have been continuously improved, which results in more and more complex radiotherapy treatment machines. However, the discussion in the previous chapter suggests that the biological aspects are needed in order to create better optimized treatment plans. To continue the discussion, I start this new chapter of “Technology versus Biology” because the biological aspects are so important and should not be overlooked.

Radiotherapy has traditionally participated in a steady march toward incorporating more and more complex technology and treatment techniques in an attempt to improve local control and hence survival. The pace of this march has increased dramatically over the past decade. This steady progression is in the name of improving the quality of radiotherapy treatment but the metrics used to characterize this improvement are not always clearly defined. It is very common to assess the quality of a treatment by looking at the dose distribution, the limited dose escalation in target and dose reduction in normal tissue^{3, 12, 86-89}. However, improvement of these metrics does not necessarily translate into better local control of tumors and patient survival^{24, 90}. Furthermore, we know that with increased complexity comes increased risk for error and often increased uncertainty in the delivered dose distribution. Thus, even given clearly defined quantitative metrics, it is not always easy to define the circumstances under which increased complexity is justified for the sake of improvements in radiotherapy plan quality.

The progression of treatment technologies from 3D conformal radiotherapy (3D CRT) to static-field intensity-modulated radiotherapy (S-IMRT) to arc-based or rotational IMRT

(R-IMRT) to proton therapy and other particle beam therapy has significantly widened our options and improved our ability to shape the physical absorbed dose distribution⁹¹⁻⁹⁶. Better plan statistics generated within more powerful treatment planning systems are generally assumed *a priori* to signify better plan quality. However, radiotherapy is more than a pretty picture on a treatment planning system screen. Overall treatment effectiveness will be affected by a number of factors and while the quality of the dose distribution is clearly an important metric, it is not the only relevant one. A number of physical and biological factors are related to treatment outcome and changes in these factors are often affected by the level of complexity of the treatment technique. The aim of this paper is to discuss some of these factors which are not necessarily always considered prior to employing highly complex technology for radiotherapy.

5.1 Dose distribution capability

The primary endpoint of much of the technology development in radiotherapy today is the improvement of the physical absorbed dose distribution. Indeed, since the goal of radiotherapy is to deliver full dose to the tumor and minimum dose to normal tissues, the dose distribution is the most obvious indicator of treatment quality. The implementation of inverse planning systems and S-IMRT delivery techniques has resulted in significant reductions in absorbed dose to organs-at-risk (OARs) compared to 3D CRT³⁻⁶. Many studies have been reported that, compared to 3D CRT, S-IMRT treatment leads to lower normal tissue complication probability (NTCP)^{7-10,97}. This increased conformity can also be exploited by escalating the dose to the target to achieve higher tumor control probability (TCP) while maintaining OAR doses below their tolerance¹¹⁻¹³. It should also be noted that changes in the delivery technique can significantly change the absorbed dose

throughout the patient, and not just in the vicinity of the target structure(s). For example, in the study reported by Mansur *et al*¹⁴, the authors found that compared to 3D CRT, S-IMRT treatment resulted in lower peripheral dose in regions closer to the target. However, at distant points, S-IMRT deposited more dose than 3D CRT presumably due to S-IMRT's higher monitor units and increased head leakage.

A more recent addition to IMRT technology is rotational IMRT or arc therapy (R-IMRT) such as TomoTherapy (Tomotherapy, Inc., Madison, WI), RapidArc (Varian Medical Systems, Palo Alto, CA), and VMAT (Elekta, Stockholm, Sweden). Many studies have shown that R-IMRT can achieve a more conformal dose distribution and reduce normal tissue "hot spots" compared to S-IMRT as well as delivering treatment faster^{92, 95-96, 98}. Generally speaking, R-IMRT treatment spreads the dose to normal tissues over a larger volume than S-IMRT. However, theoretically the dose distribution achieved by R-IMRT delivery should also be achievable by S-IMRT plans containing more fields at different beam angles⁹⁹. However whether it is better to dispose of the integral dose by delivering a relatively lower dose over a larger volume than a relatively higher dose over a smaller volume has not been proven clinically¹⁰⁰. An animal study by Semenenko *et al* suggests that for lung cancer treatment, R-IMRT may be at a disadvantage as it deposits the dose to a larger volume¹⁰¹.

Proton therapy and intensity modulated proton therapy (IMPT) have also been gaining momentum, most notably in the United States. Because of the finite range of proton beams and the delivery of increased dose within the Bragg peak, the absorbed dose distribution can be made exceptionally conformal. Many studies have shown that the integral dose to normal tissues can be significantly reduced without compromise to target coverage^{89, 93, 102-}

¹⁰⁴. As a result of the highly conformal dose distributions and the absence of exit dose, proton therapy could allow dose escalation to a new level but at a significantly increased infrastructural complexity and financial outlay.

Better image guidance technology allows clinicians to potentially reduce PTV margins which then provides increased latitude within which to capitalize on the more conformal dose distributions offered by more sophisticated delivery techniques. However, as we mentioned in the first chapter, reduced margins result in the potential hazard of a geographical miss and the ionizing radiation from image guidance could make the radiotherapy biologically less effective.^{24-25, 27, 105}

5.2 Delivery mechanism

A variety of techniques are used to deliver IMRT treatments. For most of these procedures, the treatment time ranges from 3 to 15 min. However, variations in machine type, delivery method, plan complexity, and fraction size can increase delivery time to up to 20–40 min. Use of stereotactic technique and respiratory gating can increase this time even further¹⁰⁶⁻¹⁰⁷. The increase in treatment delivery time could affect the therapeutic balance between the desired effect on the target volume and the unwanted normal-tissue toxicity^{105, 108-114}.

Modeling studies suggests that a significant loss of biological effectiveness could be expected if the fraction delivery time is longer than 15–30 min¹⁰⁸⁻¹⁰⁹. This has been confirmed by experimental studies which show that the protraction of dose accumulation over a longer duration reduces cell kill due to the repair of DNA damage^{105, 113-114}. Compared to a conventional 2-6 min treatment, the *in vitro* study confirms an increased cell survival when the cells are irradiated with an IMRT protocol that is delivered in 20

min.¹¹⁵ Moreover, the temporal pattern also affects the cell survival.^{105, 112} The *in vitro* experiments reported by Yang *et al* results suggest that the survival fraction appears to vary with the temporal pattern of dose delivery.¹⁰⁵ The modeling study by Altman *et al*¹¹² showed that it is biologically superior to deliver the dose in a “triangular” shaped temporal pattern than in a “v-shaped” pattern presumably due to the fact that the “triangular” pattern delivers a larger portion of the dose to the volume element over a shorter period of time. In the work by Shaikh *et al*¹¹⁶, the delivery time to individual volume elements of the target was analyzed for different types of IMRT delivery techniques. This study predicted greater than 5% biologically effective dose loss for 8–10 minute delivery times in the worst case scenario. For treatment delivered in less than 2 minutes, the biological effective dose (BED) loss is insignificant (<1%). So although S-IMRT has dose distribution advantages over 3D CRT, the longer time to deliver dose to a volume element associated with S-IMRT delivery results in a loss of biologically effective dose (BED) compared to 3D CRT.

Both modeling and experimental studies agree that the delivery mechanism has an impact on BED. Longer delivery times can result in a loss of BED. Although such BED loss could be compensated theoretically, it would be limited by large uncertainties associated with the biological parameters necessary to calculate such compensation. And because late-reacting normal tissues usually repair DNA damage more slowly than tumor cells, a simple increase in dose would likely lead to worse late complications in order to maintain tumor effectiveness in protracted delivery¹¹¹. Thus it is ideal to deliver dose as rapidly as possible.

5.3 Reliability of Technology

Another important factor influenced by the level of complexity of radiotherapy

equipment is reliability. Conventional wisdom would suggest that the more complex the piece of equipment, the more likely it is that one component or process of that equipment will fail and this wisdom is supported upon examination of internal downtime data for complex equipment. Such “breakdowns” do not necessarily imply physical or mechanical failure but could simply represent the failure to communicate the appropriate information to other components within the appropriate time period. A myriad of interlocks are generally necessary to provide a failsafe environment within which to operate extremely complex equipment. The consequence of this is increased machine downtime resulting in un-planned treatment gaps or extended treatment length assuming only one fraction is delivered each day and no treatment during weekends. Thus for the same treatment course, an extended time period will be needed to complete the treatment using less reliable equipment and highly complex equipment is often less reliable. Prolongation of treatment allows tumors to repopulate and may be related to significant differences in treatment outcome. Numerous studies have been published and can be found in section 1.3 in Chapter 1. These studies indicate that dose escalation would be needed to compensate for the dose loss due to accelerated tumor cell proliferation. However, dose escalation would also increase the dose to normal tissues which results in higher complication rates. Thus the treatment schedule should not be extended and thus the importance of machine reliability in treating tumors in all sites is evident.

5.4 Technology versus Biology

Although more complex technology can provide the ability to achieve more conformal dose distributions, this potential benefit could be lost due to other factors related to this complexity, such as prolongation of individual treatment fractions or prolongation of the

entire course of radiotherapy^{46, 116}. To put this in context, let us compare dose escalation with dose lost from treatment prolongation. Let us assume that modality *A* is very reliable with an uptime of ~99.9% and is used to deliver 70Gy treatment (35 x 2Gy). This treatment course will be at least 47 days assuming one fraction per day and no treatment during weekends. Suppose that competing modality *B* can increase the target dose to 74Gy while maintaining the same OAR doses as modality *A*. The treatment course using modality *B* will be at least 51 days. However, suppose modality *B* is relatively unreliable with an uptime of 95%. On average, this will add 2 days to the treatment course (overall 53 days). If we apply the result from Withers *et al* which states that in head and neck cancers treated beyond 4 weeks the effect of cell proliferation is equivalent to a loss of radiation dose of about 0.6Gy/day⁴⁶, one can calculate the effective dose for both modalities:

$$A: 70\text{Gy} - (47-28) \text{ days} \times 0.6\text{Gy/day} = 58.6\text{Gy}$$

$$B: 74\text{Gy} - (53-28) \text{ days} \times 0.6\text{Gy/day} = 59.0\text{Gy}$$

So the difference between the effective dose delivered by these two modalities is not significant (0.4Gy). The potential benefit of dose escalation using modality *B* resulting from its superior dose distribution conformity is substantially lost due to its relative unreliability and the additional cost of making modality *B* available is wasted. If modality *B* also requires a longer time to deliver each dose fraction to a given volume element of the target, there would be additional biological loss. For example, let us assume that modality *B* causes only an additional 1% BED loss (0.74Gy) than modality *A*, a very conservative assumption given existing predictions in the literature^{108-109, 116}. Now the target BED resulting from modality *A* is actually higher than that from modality *B*. The biological

effects related to the complexity of the technology could therefore totally offset or even reverse the dose escalation gain from using technologies with better dose distribution conformity. The take home message is that radiotherapy is more than a pretty picture on a TPS screen. A nice looking dose distribution on the static set of CT simulation images does not alone predict a better outcome.

The example above illustrates the importance of other radiotherapy delivery factors besides the dose distribution capabilities and one should not become singularly focused on this parameter as the quintessential element in predicting outcome. It is also unfortunately not uncommon for patients to miss scheduled treatments ¹¹⁷. In addition, national holidays during which the clinic is not open often arise during the treatment course. Taken together, these issues could extend the treatment course by over one week. Significant losses in effective dose can occur in such situations which raises serious concerns about the predicted treatment outcome. The issue of machine reliability has quietly become a larger factor over the years as equipment has gradually increased in complexity and could potentially threaten to numb the radiation oncologist into accepting that missed treatments are an unavoidable consequence of the complex technology required for high quality radiotherapy. However, such highly complex procedures were not developed with the intention that they would be administered to all patients regardless of disease, and furthermore, the decision to allow a patient to miss a treatment due to equipment failure should not be made lightly.

In order to achieve better dose distribution conformity using IMRT, the fluence map of each field has to be more complex for a limited set of beam angles. Thus the degree of complexity is usually increased. This may include more monitor units, smaller segment

sizes, more segments, and more complex segment shapes. Studies have reported a tradeoff between complexity and treatment quality as well as delivery accuracy ¹¹⁸⁻¹²¹. Highly complex plans typically result in greater uncertainty in both the dose calculation accuracy and the delivery accuracy and thus clinicians are often required to make a decision as to whether they will choose the plan that looks better on paper but carries greater uncertainty in terms of what is actually delivered to the patient.

Furthermore, increased complexity is generally associated with greater risk for error. Several of the radiotherapy errors recently publicized in the media are evidence of the potential dangers of increased complexity in radiotherapy procedures. Moreover, the results of the head and neck phantom credentialing test from the Radiological Physics Center are clear evidence of the increased probability for error when employing complex technology ¹²². The recent trend in radiotherapy of a rapid adoption of sophisticated technology is certainly in part driven by factors other than the evidence-based improvement in outcome, for example, the desire of facilities to keep up with their competitors in terms of technological capabilities. Unfortunately, this trend seems to emphasize technology over human resources ¹²³. There has been a major push in the field of radiation oncology physics to assure appropriate training of those entering the practice of clinical radiation oncology physics, however, we are at the same time rapidly expanding the complexity of the landscape that these personnel practice in. It is estimated that more people die each year as a result of medical errors than from breast cancer ¹²⁴, and complexity is generally a key contributor to failures in the human-machine interface ¹²⁵. Therefore, complexity should be minimized wherever possible and highly complex techniques should be used only where there could be expected to be a distinct advantage

that outweighs potential negative consequences and complex treatments are not intended to be administered to every patient.

In summary, advanced technologies can produce very conformal radiotherapy treatment plans and allow more accurate target localization and more rapid dose delivery. As a result, normal tissues can be better spared to reduce complications and the target dose can be escalated to achieve higher control rates. While such clinical advantages are widely publicized, we must consider other factors associated with increased complexity that could influence the treatment effectiveness and patient safety. The overall treatment effectiveness depends on not only the dose distribution capabilities offered by the technology but also on other key factors including the fraction delivery time, machine reliability, delivery accuracy, and additional imaging dose administered before or during treatment. The potential effects of these factors are discussed here but there may be other biological factors associated with increased complexity as well. Furthermore, the cost of complex technology can potentially hinder the facility's capacity to invest in the personnel to effectively and safely utilize this technology. When considering the application of highly complex technology, one needs to consider more than just the specification sheet.

5.5 Future Work

The SABER software incorporates biological and spatial information that are not available in commercial systems. However, just like the technological development, the biological evaluation and optimization also have a long way to go. For the immediate future, I would like to investigate the following components.

5.5.1 LQ-L; LQC

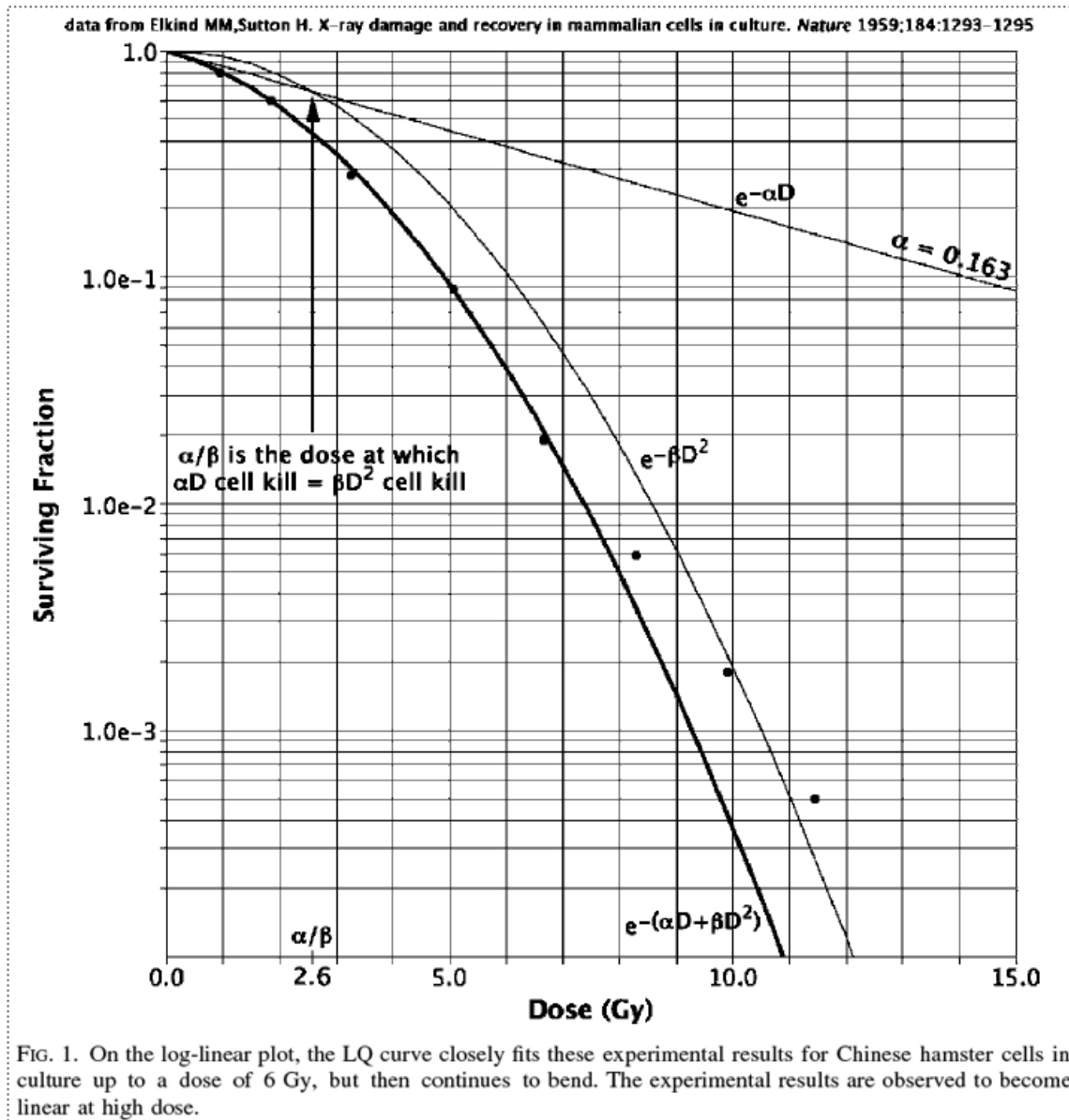


Figure 42: Experimental data showing that the LQ model over-estimates the cell survival at higher doses (Ref. 127).

The LQ model works well in most clinical cases and at low doses we may apply the IR model to include the effect of HRS. As fraction doses become very large (hypofractionation), the LQ model is also unable to predict the cell survival accurately (Figure 42). At such large fraction doses, the response becomes more linear while the

prediction based on the LQ model continues bending down which over-estimates the cell killing. In such cases, we can apply the linear-quadratic-linear (LQ-L) or linear-quadratic-cubic (LQC) model (Figure 43) to convert physical dose to EQD₂.^{44, 126}

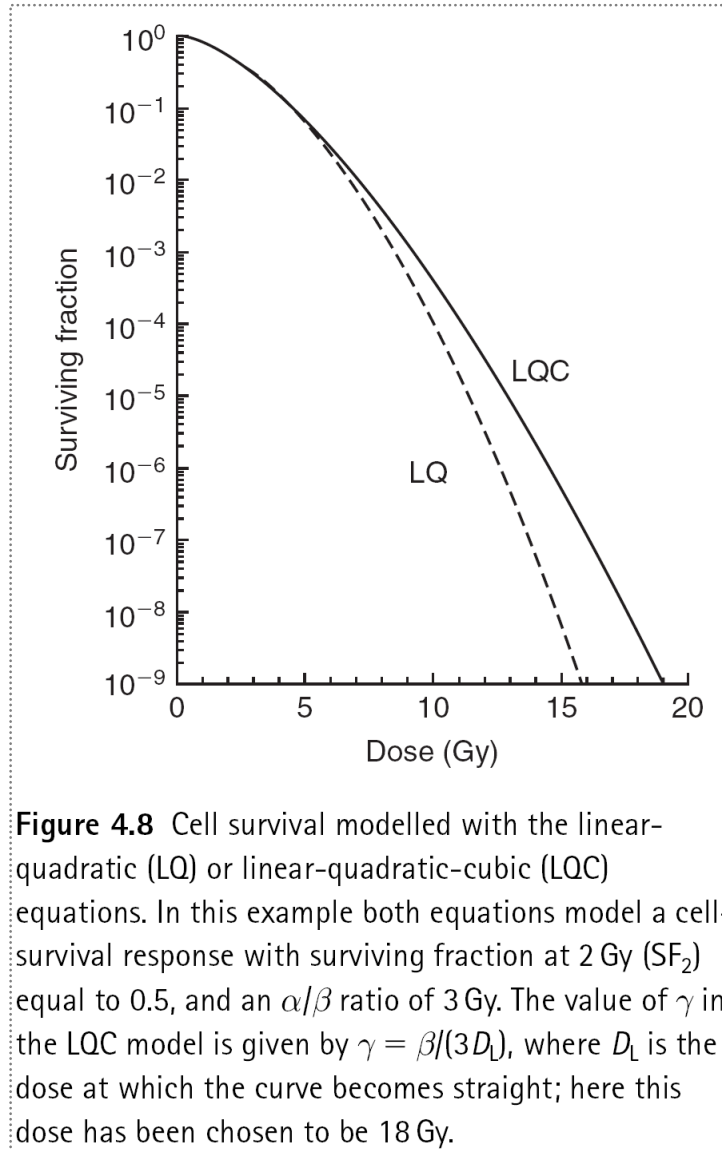


Figure 43: Linear-quadratic (LQ) versus linear-quadratic-cubic (LQC) model (Ref. 44).

It should be relatively straight forward to incorporate the LQ-L or the LQC model. For the LQ-L model, we need one threshold dose at which the survival curve becomes linear. For the LQC model, we just need to replace the linear-quadratic equation with the

linear-quadratic-cubic equation.

5.5.2 Time parameter

A radiotherapy treatment usually takes weeks. As we discussed in Chapter 1, tumor cells can re-populate during the treatment and thus the effective dose becomes less than the prescription dose. We can add the overall treatment time factor into the outcome predictions.¹²⁷

$$\text{TCP} = \exp\left(-\sum_{i=1}^n N_{0,i} \text{SF}_i\right)$$

$$\text{and } \text{SF}_i = \prod_{j=1}^{n_f} \exp(-\alpha d_{ij} - \beta d_{ij}^2) \cdot \exp\left(\frac{\ln 2}{T_{d,ij}} \Delta T\right)$$

where $N_{0,i}$ is the initial number of cells in compartment i before the delivery of the first treatment fraction; d_{ij} is the prescribed fraction dose to voxel i at fraction j , and n_f is the number of fractions; $T_{d,ij}$ is the potential doubling time of the cells in voxel i at fraction j and ΔT is the average time between fractions. ΔT is equal to T/n_f , where T is the overall treatment time.

We can implement this time parameter into the SABER software in the Poisson model. For simplicity in the first step, we can assume that the potential doubling time of the cells is constant over all voxels during the entire treatment, i.e. $T_{d,ij}$ is constant. So the surviving fraction of cells in voxel i becomes:

$$\text{SF}_i = \prod_{j=1}^{n_f} \exp(-\alpha d_i - \beta d_i^2) \cdot \exp\left(\frac{\ln 2}{T_d} \Delta T\right)$$

Compared to the Poisson model presented in Chapter 2, here we only have an extra

constant $\exp\left(\frac{\ln 2}{T_d} \Delta T\right)$, which is the overall treatment time factor. Thus the time parameter can be incorporated into the SABER software.

5.5.3 Validation of Models with Clinical Data

Many models are used in this work including DCF, gEUD (and gEUD₂), TCP, NTCP, P+, and finally the three SABER models. While some models have been applied to clinical data or at least a subset of clinical data, many remain to be validated. Because of the large uncertainties associated with the parameters used in these models, the validation will not be an easy task. It is possible that no model is absolutely right, but we would like to know which model gives a closer match to the real world data.

The DCF has proved to be useful in predicting the dose wash-out effect for small non-uniform field irradiation presumably due to cell migration.³⁴ We have applied the DCF in this work to simulate the dose wash-out effect due to various types of motion. The parameter σ could depend on the specific treatment technique, for example, IMRT, Stereotactic Body Radiotherapy or Stereotactic Radiosurgery. To predict the σ value, we need not only the response data (e.g. TCP versus prescription dose), but also the planned dose distribution (e.g. DICOM RT files). Then we can use the method described in the DCF article³⁴ to estimate σ .

A distinguishing feature in this work is that we provide three different methods (i.e. the three SABER models) to predict the outcomes. As mentioned earlier, to validate which model is the right one is difficult because of the large error bars associated with the radiobiological models. However, we can fix the parameter values and compare which model better predicts the clinical data. Again we need the clinical response data and the

planned dose distribution in order to do this.

5.5.4 Spatial and Biological Optimization

The current work focuses on spatial and biological evaluation. We would like to explore methods and/or algorithms to implement the spatial and biological metrics, such as sDVH, DCF, and EQD₂ or gEUD, into the optimization process.

EQD₂ – Biological Optimization 1

EQD₂ formula converts physical dose to biological dose by taking into account the fractionation sensitivity. The SABER software can perform such conversion at the voxel level. An intuitive way to biologically optimize the dose distribution is to replace the DVHs in the current optimizer with the eqDVHs which is the equivalent DVH normalized to 2Gy fractions. Currently, we can investigate this at the structure level. When the biological information becomes available at the voxel level, we can easily adapt the optimization to voxel basis.

gEUD – Biological Optimization 2

In the gEUD formula, the parameter a defines how relevant the level of underdosing/overdosing is in a target/OAR. Thus gEUD could potentially be used to reduce the under-dosed/over-dosed voxels in the target/OAR. For example, a possible method is to limit the maximum dose allowed in a target and meanwhile optimize the dose to achieve a minimum gEUD. Decreasing the a value (negative) will emphasize the weighting of cold spots in calculating the gEUD and thus could reduce the level of underdosing using the minimum gEUD.

DCF – Spatial Optimization 1

DCF is a smoothing filter. As a result, small clots of cold spots could be smeared out while big clots of cold spots could still exist after smoothing. Thus applying DCF prior to gEUD optimization could potentially push the optimization toward the direction of dispersed smaller clots of cold spots instead of big clots.

sDVH – Spatial Optimization 2

The sDVH is developed to evaluate the cold spot distributions across the defined regions. In the discussion section in Chapter 4, I have demonstrated that it could be used to further optimize dose distributions spatially, i.e. pushing the cold spots away from the regions where we do not want cold spots. If the sDVH could be integrated into Eclipse, it would be fairly easy to automate the additional optimization based on the sDVH concept.

APPENDIX

Introduction to DICOM RT

In this work, DICOM RT files are used to transfer data from Eclipse TPS to SABER software. DICOM stands for **D**igital **I**maging and **C**ommunications in **M**edicine and DICOM RT is the radiotherapy extension that has been added to DICOM standard since 1997. It is difficult for one that has no DICOM experience to get started, which is the situation I went through. Some information regarding processing DICOM files in Matlab is presented here to help future researchers adapt more quickly to this environment.

Matlab has built-in commands to process DICOM files. The commands include “dicomread”, “dicominfo” and “dicomwrite”. More information of these commands can be found in the Matlab Help.

a) DICOM RT Dose

For a DICOM RT dose file, the head information can be read using the command “dicominfo”. For example:

```
rdinfo = dicominfo('RD123456.dcm');    % RD123456.dcm is the file of interest
```

The returned data “*rdinfo*” is a structure that contains many fields. One can double click the variable “*rdinfo*” to see all the fields. To view a specific field, one can double click the specific field in the Matlab “Variable Editor” window. Alternatively, one can use commands to read the fields. Here is an example to read the field “NumberOfFrames”:

```
TotalFrames=rdinfo.NumberOfFrames;
```

The answer returned is the total number of frames of the dose grid.

The command “dicominfo” only reads the headers. It won’t read the actual dose grid. To do that, one needs to use the command “dicomread”. For example:

```
DoseGrid = dicomread('RD123456.dcm')
```

The returned value in “*DoseGrid*” is 4D uint32 (unsigned 32-bit integer) data. But we know that the actual dose values won’t be all integers. If we look into the 4D uint32 data, we will also notice that the dose values are very large. So the values must be scaled and magnified. Now if we go back and look at the headers in “*rdinfo*”, we can find one field called “DoseGridScaling”, which is the scaling factor that when multiplied by the dose grid data, yields grid doses in the dose units as specified by the attribute “Dose Units”. The “DoseGridScaling” is a very small number, typically at 10^{-5} or 10^{-6} . A note here is that before scaling the 4D uint32 data, one needs to convert the data from uint32 to double. Otherwise, the scaled data would only have integers, such as 70, 71, 72, etc.

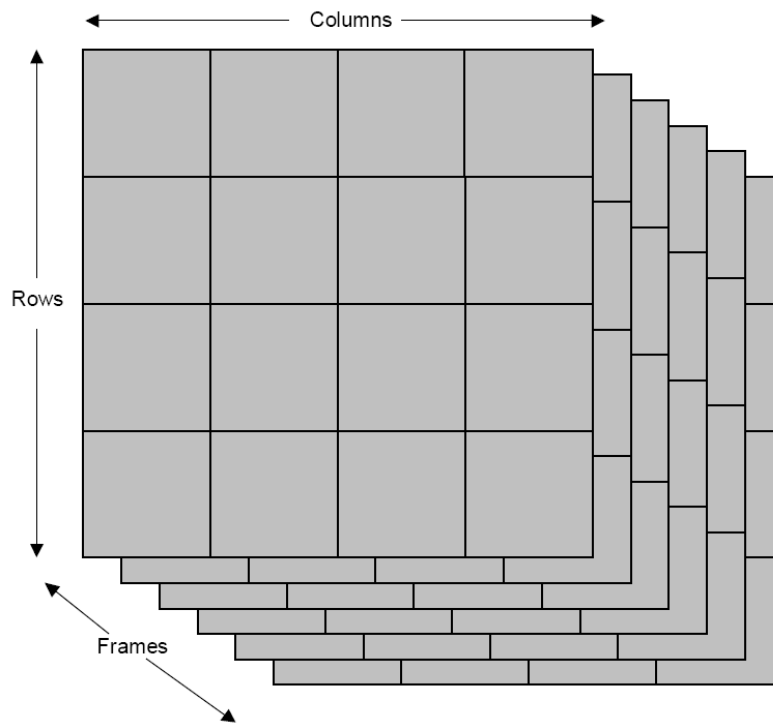


Figure 44: Architecture of DICOM RT dose grid.

Another question one would ask is why the dose is stored in 4D. The actual dose should be just a 3D matrix. A closer inspection reveals that the third dimension is only 1

value, i.e., the 4D data is $l \times m \times l \times n$, where l is the number of rows and m is the numbers of columns within one frame, and n is the number of frames along the axial direction (Figure 44). The third dimension could be an indicator that specifies the type of the stored matrix, i.e. grey value or true color, but I did not find any reference to confirm this. Anyway, for this study it is irrelevant since it will not influence our results. To convert the 4D data to a 3D matrix, try the following commands:

```
rd3D=zeros(rdinfo.Rows, rdinfo.Columns, TotalFrames);
for i=1: TotalFrames
    rd3D(:,:,i)=dicomread('RD123456.dcm', 'frames', i);
end
```

A note here is that `rdinfo.Rows` and `rdinfo.Columns` specify the size of one frame. Now the dose information has been stored in the variable “*rd3D*”, which makes it easy to manipulate the dose grid.

b) DICOM RT Structure Set

Next let us take a look at the DICOM RT structure set. Suppose the file of interest is `RS123456.dcm`. We can use the command “`dicominfo`” to read the file:

```
rsinfo = dicominfo('RS123456.dcm');
```

Similar to the “*rdinfo*”, the returned value “*rsinfo*” is also a structure that contains many fields. The contour information is stored under the field “`ROIContourSequence`” (Figure 45). There will be one item for each stored structure. For example, the first structure will be “`Item_1`”, and the second will be “`Item_2`”, and so on. Open any of the items and you will see the following three attributes:

- `ROIDisplayColor`: the color of contours used in the planning system for the

structure;

- ContourSequence: the contour information of that structure;
- ReferencedROINumber: used to identify which structure the contours belong to.

A tip here about the “ReferencedROINumber” is that it does not always the same as the item number. For example, for the structure of “Item_2”, the ReferencedROINumber may be “3”. In such cases, one need to check what structure the “ReferencedROINumber” “3” corresponds to. To do that, one need to open the “rsinfo.StructureSetROISequence” and find out which item has “ROINumber” of “3”.

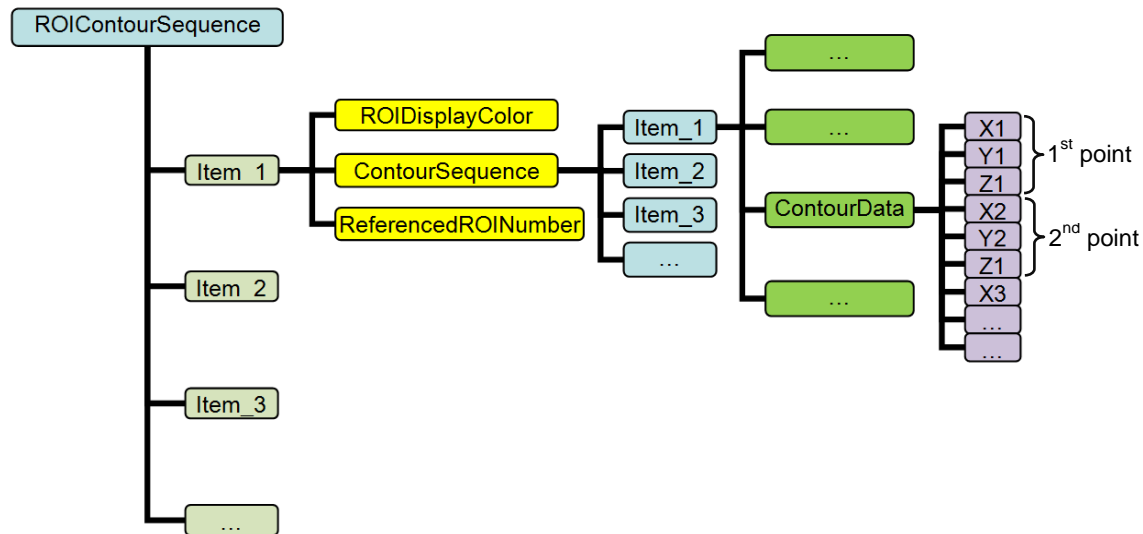


Figure 45: DICOM RT structure set contours.

Now let us look into the “ContourSequence”. Usually the “ContourSequence” contains many items and each item stores the contours point of one frame. So if the structure occupies 10 frames in the axial direction, there will be 10 items under “ContourSequence” named “Item_1”, “Item_2”... “Item_10”. In each item there is “ContourData” which consist of an array of values. The values are the actual coordinates in a Cartesian coordinates in three dimensions.

The big question is that the structure contour points are defined in a real spatial coordinate system, but the dose grid is defined as an indexed 3D matrix. How does one correlate the relative location of a 3D dose grid to the structure contour points? To answer this question, we must know at least the location of one voxel of the 3D matrix in a real Cartesian coordinates in three dimensions. Then by knowing the voxel size in all three dimensions, we can build the dose grid based on the known location of one voxel. Fortunately, there is one voxel's location stored in the DICOM RT Dose file under the field "ImagePositionPatient". The values are the X, Y and Z coordinates of the first dose voxel and are in the same Cartesian system as the structure set contours. The first dose voxel is the top left corner of the first frame. The voxel size can also be found in the DICOM files. Within one frame, the pixel size is given in the field "PixelSpacing" in DICOM RT Dose file. To find the spacing of frames, one can calculate from the Z coordinates of the contour points in two adjacent frames. Be sure to check the patient set-up orientation (stored in "ImageOrientationPatient" in DICOM RT dose), i.e. head first supine or foot first prone, etc., so that the structure contours won't be rotated or flipped relative to the dose grid.

c) DICOM RT Plan

DICOM RT Plan is relatively simple in this study since I did not deal with the beam sequence and the MLC control point. It is fairly straight forward to use the command "dicominfo" to get the essential information such as prescription dose, number of fractions, plan name, etc.

REFERENCES

1. UCSD Radiation Oncology, San Diego, CA, "History of Radiation Therapy," Available from "<http://radonc.ucsd.edu/PatientInformation/history.asp>" [Accessed February 12, 2010]
2. J. F. Heron, Caen University Faculty of Medicine, Caen, France, "Cancer Radiotherapy," Available from "http://www.oncoprof.net/Generale2000/g08_Radiotherapie/Index/g08-gb_idx02.html" [Accessed February 12, 2010]
3. P. Xia, K. K. Fu, G. W. Wong, C. Akazawa and L. J. Verhey, "Comparison of treatment plans involving intensity-modulated radiotherapy for nasopharyngeal carcinoma," *Int. J. Radiat. Oncol., Biol., Phys.* **48**, 329-337 (2000).
4. P. Fenoglietto, B. Laliberte, A. Allaw, N. Ailleres, K. Idri, M. H. Hay, C. L. Moscardo, S. Gourgou, J. B. Dubois and D. Azria, "Persistently better treatment planning results of intensity-modulated (IMRT) over conformal radiotherapy (3D-CRT) in prostate cancer patients with significant variation of clinical target volume and/or organs-at-risk," *Radiother. Oncol.* **88**, 77-87 (2008).
5. B. Longobardi, E. De Martin, C. Fiorino, I. Dell'oca, S. Broggi, G. M. Cattaneo and R. Calandrino, "Comparing 3DCRT and inversely optimized IMRT planning for head and neck cancer: equivalence between step-and-shoot and sliding window techniques," *Radiother. Oncol.* **77**, 148-156 (2005).
6. M. T. Vlachaki, T. N. Teslow, C. Amosson, N. W. Uy and S. Ahmad, "IMRT versus conventional 3DCRT on prostate and normal tissue dosimetry using an endorectal balloon for prostate immobilization," *Med. Dosim.* **30**, 69-75 (2005).

7. M. J. Zelefsky, Z. Fuks, L. Happersett, H. J. Lee, C. C. Ling, C. M. Burman, M. Hunt, T. Wolfe, E. S. Venkatraman, A. Jackson, M. Skwarchuk and S. A. Leibel, "Clinical experience with intensity modulated radiation therapy (IMRT) in prostate cancer," *Radiother. Oncol.* **55**, 241-249 (2000).
8. A. J. Mundt, A. E. Lujan, J. Rotmensch, S. E. Waggoner, S. D. Yamada, G. Fleming and J. C. Roeske, "Intensity-modulated whole pelvic radiotherapy in women with gynecologic malignancies," *Int. J. Radiat. Oncol., Biol., Phys.* **52**, 1330-1337 (2002).
9. J. C. Landry, G. Y. Yang, J. Y. Ting, C. A. Staley, W. Torres, N. Esiashvili and L. W. Davis, "Treatment of pancreatic cancer tumors with intensity-modulated radiation therapy (IMRT) using the volume at risk approach (VARA): employing dose-volume histogram (DVH) and normal tissue complication probability (NTCP) to evaluate small bowel toxicity," *Med. Dosim.* **27**, 121-129 (2002).
10. B. Mittal, A. Kepka, A. Mahadevan, M. Kies, H. Pelzer, M. List, A. Rademaker and J. Logemann, "Use of IMRT to reduce toxicity from concomitant radiation and chemotherapy for advanced head and neck cancers," *Int. J. Radiat. Oncol., Biol., Phys.* **51**, 82-83 (2001).
11. D. A. Kuban, S. L. Tucker, L. Dong, G. Starkschall, E. H. Huang, M. R. Cheung, A. K. Lee and A. Pollack, "Long-term results of the M. D. Anderson randomized dose-escalation trial for prostate cancer," *Int. J. Radiat. Oncol., Biol., Phys.* **70**, 67-74 (2008).
12. A. Pirzkall, M. Carol, F. Lohr, A. Hoss, M. Wannenmacher and J. Debus, "Comparison of intensity-modulated radiotherapy with conventional conformal

- radiotherapy for complex-shaped tumors," *Int. J. Radiat. Oncol., Biol., Phys.* **48**, 1371-1380 (2000).
13. Q. Wu, M. Manning, R. Schmidt-Ullrich and R. Mohan, "The potential for sparing of parotids and escalation of biologically effective dose with intensity-modulated radiation treatments of head and neck cancers: a treatment design study," *Int. J. Radiat. Oncol., Biol., Phys.* **46**, 195-205 (2000).
 14. D. B. Mansur, E. E. Klein and B. P. Maserang, "Measured peripheral dose in pediatric radiation therapy: a comparison of intensity-modulated and conformal techniques," *Radiother. Oncol.* **82**, 179-184 (2007).
 15. B. Kihlen and B. I. Ruden, "Reproducibility of field alignment in radiation therapy. A large-scale clinical experience," *Acta. Oncol.* **28**, 689-692 (1989).
 16. I. Rabinowitz, J. Broomberg, M. Goitein, K. McCarthy and J. Leong, "Accuracy of radiation field alignment in clinical practice," *Int. J. Radiat. Oncol., Biol., Phys.* **11**, 1857-1867 (1985).
 17. S. A. Rosenthal, J. M. Galvin, J. W. Goldwein, A. R. Smith and P. H. Blitzer, "Improved methods for determination of variability in patient positioning for radiation therapy using simulation and serial portal film measurements," *Int. J. Radiat. Oncol., Biol., Phys.* **23**, 621-625 (1992).
 18. P. Jain, T. Marchant, M. Green, G. Watkins, J. Davies, C. McCarthy, J. Loncaster, A. Stewart, B. Magee, C. Moore and P. Price, "Inter-fraction motion and dosimetric consequences during breast intensity-modulated radiotherapy (IMRT)," *Radiother. Oncol.* **90**, 93-98 (2009).

19. T. Bortfeld, K. Jokivarsi, M. Goitein, J. Kung and S. B. Jiang, "Effects of intra-fraction motion on IMRT dose delivery: statistical analysis and simulation," *Phys. Med. Biol.* **47**, 2203-2220 (2002).
20. H. S. Li, I. J. Chetty, C. A. Enke, R. D. Foster, T. R. Willoughby, P. A. Kupellian and T. D. Solberg, "Dosimetric consequences of intrafraction prostate motion," *Int. J. Radiat. Oncol., Biol., Phys.* **71**, 801-812 (2008).
21. T. Rosewall, P. Chung, A. Bayley, G. Lockwood, H. Alasti, R. Bristow, V. Kong, M. Milosevic and C. Catton, "A randomized comparison of interfraction and intrafraction prostate motion with and without abdominal compression," *Radiother. Oncol.* **88**, 88-94 (2008).
22. J. M. Balter, R. K. Ten Haken, T. S. Lawrence, K. L. Lam and J. M. Robertson, "Uncertainties in CT-based radiation therapy treatment planning associated with patient breathing," *Int. J. Radiat. Oncol., Biol., Phys.* **36**, 167-174 (1996).
23. J. Mechalakos, E. Yorke, G. S. Mageras, A. Hertanto, A. Jackson, C. Obcemea, K. Rosenzweig and C. Clifton Ling, "Dosimetric effect of respiratory motion in external beam radiotherapy of the lung," *Radiother. Oncol.* **71**, 191-200 (2004).
24. B. Engels, G. Soete, D. Verellen and G. Storme, "Conformal arc radiotherapy for prostate cancer: increased biochemical failure in patients with distended rectum on the planning computed tomogram despite image guidance by implanted markers," *Int. J. Radiat. Oncol., Biol., Phys.* **74**, 388-391 (2009).
25. G. X. Ding and C. W. Coffey, "Radiation dose from kilovoltage cone beam computed tomography in an image-guided radiotherapy procedure," *Int. J. Radiat. Oncol., Biol., Phys.* **73**, 610-617 (2009).

26. W. Yang, L. Wang, P. Read, J. Larner and K. Sheng, "Increased Tumor Radioresistance by Imaging Doses From Volumetric Image Guided Radiation Therapy [abstract]," *Med. Phys.* **36**, 2808-2808 (2009).
27. H. P. Bijl, P. van Luijk, R. P. Coppes, J. M. Schippers, A. W. Konings and A. J. van der Kogel, "Unexpected changes of rat cervical spinal cord tolerance caused by inhomogeneous dose distributions," *Int. J. Radiat. Oncol., Biol., Phys.* **57**, 274-281 (2003).
28. R. J. M. Franklin, J. M. Gilson and W. F. Blakemore, "Local recruitment of remyelinating cells in the repair of demyelination in the central nervous system," *J. Neurosci. Res.* **50**, 337-344 (1997).
29. E. E. Klein, J. Hanley, J. Bayouth, F.-F. Yin, W. Simon, S. Dresser, C. Serago, F. Aguirre, L. Ma, B. Arjomandy, C. Liu, C. Sandin and T. Holmes, "Task Group 142 report: Quality assurance of medical accelerators," *Med. Phys.* **36**, 4197-4212 (2009).
30. S. H. Benedict, F. J. Bova, B. Clark, S. J. Goetsch, W. H. Hinson, D. D. Leavitt, D. J. Schlesinger and K. M. Yenice, "Anniversary Paper: the role of medical physicists in developing stereotactic radiosurgery," *Med. Phys.* **35**, 4262-4277 (2008).
31. T. Takakura, T. Mizowaki, M. Nakata, S. Yano, T. Fujimoto, Y. Miyabe, M. Nakamura and M. Hiraoka, "The geometric accuracy of frameless stereotactic radiosurgery using a 6D robotic couch system," *Phys. Med. Biol.* **55**, 1-10 (2010).
32. S. Yoo, Q. J. Wu, D. Godfrey, H. Yan, L. Ren, S. Das, W. R. Lee and F.-F. Yin, "Clinical Evaluation of Positioning Verification Using Digital Tomosynthesis and

- Bony Anatomy and Soft Tissues for Prostate Image-Guided Radiotherapy," *Int. J. Radiat. Oncol., Biol., Phys.* **73**, 296-305 (2009).
33. G. Jozsef, S. C. Lymberis, K. J. DeWyngaert and S. C. Formenti, "Prospective Study of Cone-beam CT (CBCT) Guidance for Prone Accelerated Partial Breast Irradiation (APBI)," *Int. J. Radiat. Oncol., Biol., Phys.* **75**, S571-S572 (2009).
 34. Y. Huang, M. C. Joiner, B. Zhao, Y. Liao and J. Burmeister, "Dose Convolution Filter: Incorporating spatial dose information into tissue response modelling," *Med. Phys.* **37**, 1068-1074 (2010).
 35. J. Löff, *Development of a general framework for optimization of radiation therapy*, PhD Thesis, Stockholm University, 2000.
 36. H. I. Amols and C. C. Ling, "EUD but not QED," *Int. J. Radiat. Oncol., Biol., Phys.* **52**, 1-2 (2002).
 37. W. A. Tome and J. F. Fowler, "On cold spots in tumor subvolumes," *Med. Phys.* **29**, 1590-1598 (2002).
 38. T. Bortfeld, D. Craft, J. F. Dempsey, T. Halabi and H. E. Romeijn, "Evaluating Target Cold Spots By the use of Tail EUDs," *Int. J. Radiat. Oncol., Biol., Phys.* **71**, 880-889 (2008).
 39. H. D. Thames, M. Zhang, S. L. Tucker, H. H. Liu, L. Dong and R. Mohan, "Cluster models of dose-volume effects," *Int. J. Radiat. Oncol., Biol., Phys.* **59**, 1491-1504 (2004).
 40. G. T. Chen, "Dose volume histograms in treatment planning," *Int. J. Radiat. Oncol., Biol., Phys.* **14**, 1319-1320 (1988).

41. R. E. Drzymala, R. Mohan, L. Brewster, J. Chu, M. Goitein, W. Harms and M. Urie, "Dose-volume histograms," *Int. J. Radiat. Oncol., Biol., Phys.* **21**, 71-78 (1991).
42. L. Pisani, D. Lockman, D. Jaffray, D. Yan, A. Martinez and J. Wong, "Setup error in radiotherapy: on-line correction using electronic kilovoltage and megavoltage radiographs," *Int. J. Radiat. Oncol., Biol., Phys.* **47**, 825-839 (2000).
43. C. Wild-Bode, M. Weller, A. Rimner, J. Dichgans and W. Wick, "Sublethal irradiation promotes migration and invasiveness of glioma cells: implications for radiotherapy of human glioblastoma," *Cancer Res.* **61**, 2744-2750 (2001).
44. M. Joiner and A. v. d. Kogel, *Basic clinical radiobiology*, 4th ed. (Hodder Arnold, London, 2009).
45. H. P. Bijl, P. van Luijk, R. P. Coppes, J. M. Schippers, A. W. Konings and A. J. van der Kogel, "Dose-volume effects in the rat cervical spinal cord after proton irradiation," *Int. J. Radiat. Oncol., Biol., Phys.* **52**, 205-211 (2002).
46. H. R. Withers, J. M. Taylor and B. Maciejewski, "The hazard of accelerated tumor clonogen repopulation during radiotherapy," *Acta. Oncol.* **27**, 131-146 (1988).
47. R. Tarnawski, J. Fowler, K. Skladowski, A. Swierniak, R. Suwinski, B. Maciejewski and A. Wygoda, "How fast is repopulation of tumor cells during the treatment gap?," *Int. J. Radiat. Oncol., Biol., Phys.* **54**, 229-236 (2002).
48. J. Z. Wang, Z. Huang, M. Gao, W. T. C. Yuh and N. A. Mayr, "When Tumor Repopulation Starts? An Outcome Analysis of Radiotherpay for Cervical Cancer (abstract)," *Med. Phys.* **36**, 2637 (2009).
49. R. E. Durand, "Tumor repopulation during radiotherapy: quantitation in two xenografted human tumors," *Int. J. Radiat. Oncol., Biol., Phys.* **39**, 803-808 (1997).

50. M. Machtay, C. Hsu, R. Komaki, W. T. Sause, R. S. Swann, C. J. Langer, R. W. Byhardt and W. J. Curran, "Effect of overall treatment time on outcomes after concurrent chemoradiation for locally advanced non-small-cell lung carcinoma: analysis of the Radiation Therapy Oncology Group (RTOG) experience," *Int. J. Radiat. Oncol., Biol., Phys.* **63**, 667-671 (2005).
51. M. Mehta, R. Scrimger, R. Mackie, B. Paliwal, R. Chappell and J. Fowler, "A new approach to dose escalation in non-small-cell lung cancer," *Int. J. Radiat. Oncol., Biol., Phys.* **49**, 23-33 (2001).
52. D. J. D'Ambrosio, T. Li, E. M. Horwitz, D. Y. Chen, A. Pollack and M. K. Buyyounouski, "Does treatment duration affect outcome after radiotherapy for prostate cancer?," *Int. J. Radiat. Oncol., Biol., Phys.* **72**, 1402-1407 (2008).
53. H. D. Thames, D. Kuban, L. B. Levy, E. M. Horwitz, P. Kupelian, A. Martinez, J. Michalski, T. Pisansky, H. Sandler, W. Shipley, M. Zelefsky and A. Zietman, "The role of overall treatment time in the outcome of radiotherapy of prostate cancer: An analysis of biochemical failure in 4839 men treated between 1987 and 1995," *Radiother. Oncol.* **In Press, Corrected Proof**.
54. P. Kallman, A. Agren and A. Brahme, "Tumour and normal tissue responses to fractionated non-uniform dose delivery," *Int. J. Radiat. Biol.* **62**, 249-262 (1992).
55. V. Y. Kuperman, "General properties of different models used to predict normal tissue complications due to radiation," *Med. Phys.* **35**, 4831-4836 (2008).
56. C. Burman, G. J. Kutcher, B. Emami and M. Goitein, "Fitting of normal tissue tolerance data to an analytic function," *Int. J. Radiat. Oncol., Biol., Phys.* **21**, 123-135 (1991).

57. G. J. Kutcher and C. Burman, "Calculation of complication probability factors for non-uniform normal tissue irradiation: the effective volume method," *Int. J. Radiat. Oncol., Biol., Phys.* **16**, 1623-1630 (1989).
58. J. T. Lyman, "Complication probability as assessed from dose-volume histograms," *Radiat. Res.* **8**, S13-19 (1985).
59. A. Niemierko, "Reporting and analyzing dose distributions: a concept of equivalent uniform dose," *Med. Phys.* **24**, 103-110 (1997).
60. A. Niemierko, "A generalized concept of equivalent uniform dose (EUD) (abstract)," *Med. Phys.* **26**, 1100 (1999).
61. H. A. Gay and A. Niemierko, "A free program for calculating EUD-based NTCP and TCP in external beam radiotherapy," *Phys. Medica* **23**, 115-125 (2007).
62. L. C. Jones and P. W. Hoban, "Treatment plan comparison using equivalent uniform biologically effective dose (EUBED)," *Phys. Med. Biol.* **45**, 159-170 (2000).
63. D. Liu, M. Ajlouni, J. Y. Jin, S. Ryu, F. Siddiqui, A. Patel, B. Movsas and I. J. Chetty, "Analysis of outcomes in radiation oncology: an integrated computational platform," *Med. Phys.* **36**, 1680-1689 (2009).
64. B. Sanchez-Nieto and A. E. Nahum, "BIOPLAN: software for the biological evaluation of radiotherapy treatment plans," *Med. Dosim.* **25**, 71-76 (2000).
65. B. Warkentin, P. Stavrev, N. Stavreva, C. Field and B. G. Fallone, "A TCP-NTCP estimation module using DVHs and known radiobiological models and parameter sets," *J. Appl. Clin. Med. Phys.* **5**, 50-63 (2004).

66. C. W. Cheng and I. J. Das, "Treatment plan evaluation using dose-volume histogram (DVH) and spatial dose-volume histogram (zDVH)," *Int. J. Radiat. Oncol., Biol., Phys.* **43**, 1143-1150 (1999).
67. K. S. Chao, A. I. Blanco and J. F. Dempsey, "A conceptual model integrating spatial information to assess target volume coverage for IMRT treatment planning," *Int. J. Radiat. Oncol., Biol., Phys.* **56**, 1438-1449 (2003).
68. G. P. Chen, E. Ahunbay, C. Schultz and X. A. Li, "Development of an inverse optimization package to plan nonuniform dose distributions based on spatially inhomogeneous radiosensitivity extracted from biological images," *Med. Phys.* **34**, 1198-1205 (2007).
69. J. O. Deasy, A. I. Blanco and V. H. Clark, "CERR: a computational environment for radiotherapy research," *Med. Phys.* **30**, 979-985 (2003).
70. I. El Naqa, G. Suneja, P. E. Lindsay, A. J. Hope, J. R. Alaly, M. Vicic, J. D. Bradley, A. Apte and J. O. Deasy, "Dose response explorer: an integrated open-source tool for exploring and modelling radiotherapy dose-volume outcome relationships," *Phys. Med. Biol.* **51**, 5719-5735 (2006).
71. RaySearch Laboratories AB, "Biological optimization using the equivalent uniform dose (EUD) in Pinnacle³®," *RaySearch White Paper*, Stockholm, Sweden (2003)
72. M. Adamus-Gorka, P. Mavroidis, A. Brahme and B. K. Lind, "The dose--response relation for rat spinal cord paralysis analyzed in terms of the effective size of the functional subunit," *Phys. Med. Biol.* **53**, 6533-6547 (2008).

73. J. Leong, "Implementation of random positioning error in computerised radiation treatment planning systems as a result of fractionation," *Phys. Med. Biol.* **32**, 327-334 (1987).
74. H. D. Thames, Jr., H. R. Withers, L. J. Peters and G. H. Fletcher, "Changes in early and late radiation responses with altered dose fractionation: implications for dose-survival relationships," *Int. J. Radiat. Oncol., Biol., Phys.* **8**, 219-226 (1982).
75. M. C. Joiner, B. Marples, P. Lambin, S. C. Short and I. Turesson, "Low-dose hypersensitivity: current status and possible mechanisms," *Int. J. Radiat. Oncol., Biol., Phys.* **49**, 379-389 (2001).
76. P. Lambin, B. Marples, B. Fertil, E. P. Malaise and M. C. Joiner, "Hypersensitivity of a human tumour cell line to very low radiation doses," *Int. J. Radiat. Biol.* **63**, 639-650 (1993).
77. B. Marples and S. J. Collis, "Low-dose hyper-radiosensitivity: past, present, and future," *Int. J. Radiat. Oncol., Biol., Phys.* **70**, 1310-1318 (2008).
78. Q. Wu, R. Mohan, A. Niemierko and R. Schmidt-Ullrich, "Optimization of intensity-modulated radiotherapy plans based on the equivalent uniform dose," *Int. J. Radiat. Oncol., Biol., Phys.* **52**, 224-235 (2002).
79. Y. Liao, M. Joiner, Y. Huang and J. Burmeister, "Hypofractionation: what does it mean for prostate cancer treatment?," *Int. J. Radiat. Oncol., Biol., Phys.* **76**, 260-268 (2010).
80. S. M. Bentzen and S. L. Tucker, "Quantifying the position and steepness of radiation dose-response curves," *Int. J. Radiat. Biol.* **71**, 531-542 (1997).

81. T. R. Munro and C. W. Gilbert, "The relation between tumour lethal doses and the radiosensitivity of tumour cells," *Br. J. Radiol.* **34**, 246-251 (1961).
82. A. Agren, A. Brahme and I. Turesson, "Optimization of uncomplicated control for head and neck tumors," *Int. J. Radiat. Oncol., Biol., Phys.* **19**, 1077-1085 (1990).
83. M. C. Joiner, B. Marples and H. Johns, "The response of tissues to very low doses per fraction: a reflection of induced repair?," *Recent Results Cancer Res.* **130**, 27-40 (1993).
84. P. Lambin, E. P. Malaise and M. C. Joiner, "Might intrinsic radioresistance of human tumour cells be induced by radiation?," *Int. J. Radiat. Biol.* **69**, 279-290 (1996).
85. L. Marks, R. Ten Haken and M. Martel, eds., "Quantitative Analyses of Normal Tissue Effects in the Clinic," *Int. J. Radiat. Oncol., Biol., Phys.* **76**, S1-S160 (2010).
86. A. Bertelsen, C. R. Hansen, J. Johansen and C. Brink, "Single Arc Volumetric Modulated Arc Therapy of head and neck cancer," *Radiother. Oncol.* **95**, 142-148 (2010).
87. W. Crijns, T. Budiharto, G. Defraene, J. Verstraete, T. Depuydt, K. Haustermans and F. Van den Heuvel, "IMRT-based optimization approaches for volumetric modulated single arc radiotherapy planning," *Radiother. Oncol.* **95**, 149-152 (2010).
88. S. D. McGrath, M. M. Matuszak, D. Yan, L. L. Kestin, A. A. Martinez and I. S. Grills, "Volumetric modulated arc therapy for delivery of hypofractionated stereotactic lung radiotherapy: A dosimetric and treatment efficiency analysis," *Radiother. Oncol.* **95**, 153-157 (2010).

89. W. H. St Clair, J. A. Adams, M. Bues, B. C. Fullerton, S. La Shell, H. M. Kooy, J. S. Loeffler and N. J. Tarbell, "Advantage of protons compared to conventional X-ray or IMRT in the treatment of a pediatric patient with medulloblastoma," *Int. J. Radiat. Oncol., Biol., Phys.* **58**, 727-734 (2004).
90. M. Van Herk, "Will IGRT live up to its promise?," *Acta. Oncol.* **47**, 1186-1187 (2008).
91. J. Y. Chang, X. Zhang, X. Wang, Y. Kang, B. Riley, S. Bilton, R. Mohan, R. Komaki and J. D. Cox, "Significant reduction of normal tissue dose by proton radiotherapy compared with three-dimensional conformal or intensity-modulated radiation therapy in Stage I or Stage III non-small-cell lung cancer," *Int. J. Radiat. Oncol., Biol., Phys.* **65**, 1087-1096 (2006).
92. L. Cozzi, K. A. Dinshaw, S. K. Shrivastava, U. Mahantshetty, R. Engineer, D. D. Deshpande, S. V. Jamema, E. Vanetti, A. Clivio, G. Nicolini and A. Fogliata, "A treatment planning study comparing volumetric arc modulation with RapidArc and fixed field IMRT for cervix uteri radiotherapy," *Radiother. Oncol.* **89**, 180-191 (2008).
93. U. Mock, D. Georg, J. Bogner, T. Auberger and R. Potter, "Treatment planning comparison of conventional, 3D conformal, and intensity-modulated photon (IMRT) and proton therapy for paranasal sinus carcinoma," *Int. J. Radiat. Oncol., Biol., Phys.* **58**, 147-154 (2004).
94. M. Oliver, W. Ansbacher and W. A. Beckham, "Comparing planning time, delivery time and plan quality for IMRT, RapidArc and Tomotherapy," *J. Appl. Clin. Med. Phys.* **10**, 3068 (2009).

95. K. Sheng, J. A. Molloy and P. W. Read, "Intensity-modulated radiation therapy (IMRT) dosimetry of the head and neck: a comparison of treatment plans using linear accelerator-based IMRT and helical tomotherapy," *Int. J. Radiat. Oncol., Biol., Phys.* **65**, 917-923 (2006).
96. C. X. Yu, X. A. Li, L. Ma, D. Chen, S. Naqvi, D. Shepard, M. Sarfaraz, T. W. Holmes, M. Suntharalingam and C. M. Mansfield, "Clinical implementation of intensity-modulated arc therapy," *Int. J. Radiat. Oncol., Biol., Phys.* **53**, 453-463 (2002).
97. M. W. McDonald, K. D. Godette, E. K. Butker, L. W. Davis and P. A. Johnstone, "Long-term outcomes of IMRT for breast cancer: a single-institution cohort analysis," *Int. J. Radiat. Oncol., Biol., Phys.* **72**, 1031-1040 (2008).
98. A. P. Shah, S. S. Chen, J. B. Strauss, M. C. Kirk, J. L. Coleman, A. B. Coon, C. Miller and A. Dickler, "A Dosimetric Analysis Comparing Treatment of Low-Risk Prostate Cancer With TomoTherapy Versus Static Field Intensity Modulated Radiation Therapy," *Am. J. Clin. Oncol.* (2009).
99. T. Bortfeld and S. Webb, "Single-Arc IMRT?," *Phys. Med. Biol.* **54**, N9-20 (2009).
100. M. Goitein, "How best to dispose of extra-tumoral dose: a cautionary note for intensity-modulated radiation therapy," *Int. J. Radiat. Oncol., Biol., Phys.* **75**, 1-3 (2009).
101. V. A. Semenenko, R. C. Molthen, C. Li, N. V. Morrow, R. Li, S. N. Ghosh, M. M. Medhora and X. A. Li, "Irradiation of varying volumes of rat lung to same mean lung dose: a little to a lot or a lot to a little?," *Int. J. Radiat. Oncol., Biol., Phys.* **71**, 838-847 (2008).

102. W. P. Levin, H. Kooy, J. S. Loeffler and T. F. DeLaney, "Proton beam therapy," *Br. J. Cancer* **93**, 849-854 (2005).
103. A. Trofimov, P. L. Nguyen, J. J. Coen, K. P. Doppke, R. J. Schneider, J. A. Adams, T. R. Bortfeld, A. L. Zietman, T. F. Delaney and W. U. Shipley, "Radiotherapy treatment of early-stage prostate cancer with IMRT and protons: a treatment planning comparison," *Int. J. Radiat. Oncol., Biol., Phys.* **69**, 444-453 (2007).
104. A. Fogliata, S. Yartsev, G. Nicolini, A. Clivio, E. Vanetti, R. Wyttenbach, G. Bauman and L. Cozzi, "On the performances of Intensity Modulated Protons, RapidArc and Helical Tomotherapy for selected paediatric cases," *Radiat. Oncol.* **4**, 2 (2009).
105. W. Yang, L. Wang, J. Larner, P. Read, S. Benedict and K. Sheng, "Tumor cell survival dependence on helical tomotherapy, continuous arc and segmented dose delivery," *Phys. Med. Biol.* **54**, 6635-6643 (2009).
106. A. Schweikard, H. Shiomi and J. Adler, "Respiration tracking in radiosurgery," *Med. Phys.* **31**, 2738-2741 (2004).
107. M. Dahele, S. Pearson, T. Purdie, J. P. Bissonnette, K. Franks, A. Brade, J. Cho, A. Sun, A. Hope, A. Marshall, J. Higgins and A. Bezjak, "Practical considerations arising from the implementation of lung stereotactic body radiation therapy (SBRT) at a comprehensive cancer center," *J. Thorac. Oncol.* **3**, 1332-1341 (2008).
108. J. Z. Wang, X. A. Li, W. D. D'Souza and R. D. Stewart, "Impact of prolonged fraction delivery times on tumor control: a note of caution for intensity-modulated radiation therapy (IMRT)," *Int. J. Radiat. Oncol., Biol., Phys.* **57**, 543-552 (2003).

109. J. F. Fowler, J. S. Welsh and S. P. Howard, "Loss of biological effect in prolonged fraction delivery," *Int. J. Radiat. Oncol., Biol., Phys.* **59**, 242-249 (2004).
110. X. Mu, P. O. Lofroth, M. Karlsson and B. Zackrisson, "The effect of fraction time in intensity modulated radiotherapy: theoretical and experimental evaluation of an optimisation problem," *Radiother. Oncol.* **68**, 181-187 (2003).
111. M. C. Joiner, N. Mogili, B. Marples and J. Burmeister, "Significant dose can be lost by extended delivery times in IMRT with x rays but not high-LET radiations," *Med. Phys.* **37**, 2457-2465 (2010).
112. M. B. Altman, S. J. Chmura, J. O. Deasy and J. C. Roeske, "Optimization of the temporal pattern of radiation: an IMRT based study," *Int. J. Radiat. Oncol., Biol., Phys.* **66**, 898-905 (2006).
113. J. M. Bewes, N. Suchowerska, M. Jackson, M. Zhang and D. R. McKenzie, "The radiobiological effect of intra-fraction dose-rate modulation in intensity modulated radiation therapy (IMRT)," *Phys. Med. Biol.* **53**, 3567-3578 (2008).
114. V. Moiseenko, C. Duzenli and R. E. Durand, "In vitro study of cell survival following dynamic MLC intensity-modulated radiation therapy dose delivery," *Med. Phys.* **34**, 1514-1520 (2007).
115. W. F. Morgan, S. A. Naqvi, C. Yu, L. E. Smith and M. Bose, "Does the time required to deliver IMRT reduce its biological effectiveness," *Int. J. Radiat. Oncol., Biol., Phys.* **54**, 222-222 (2002).
116. M. Shaikh, J. Burmeister, M. Joiner, S. Pandya, B. Zhao and Q. Liu, "Biological Effect of Different IMRT Delivery Techniques: SMLC, DMLC and Helical Tomotherapy," *Med. Phys.* **37**, 762-771 (2010).

117. R. D. Lindberg, K. Jones, H. H. Garner, B. Jose, W. J. Spanos, Jr. and D. Bhatnagar, "Evaluation of unplanned interruptions in radiotherapy treatment schedules," Int. J. Radiat. Oncol., Biol., Phys. **14**, 811-815 (1988).
118. D. Craft, P. Suss and T. Bortfeld, "The tradeoff between treatment plan quality and required number of monitor units in intensity-modulated radiotherapy," Int. J. Radiat. Oncol., Biol., Phys. **67**, 1596-1605 (2007).
119. M. Broderick, M. Leech and M. Coffey, "Direct aperture optimization as a means of reducing the complexity of Intensity Modulated Radiation Therapy plans," Radiat. Oncol. **4**, 8 (2009).
120. S. Pandya and J. Burmeister, "Effect of Fluence Smoothing On Plan Quality and Delivery Accuracy in Intensity Modulated Radiotherapy (*abstract*)," Med. Phys. **35**, 2755 (2008).
121. N. Giorgia, F. Antonella, V. Eugenio, C. Alessandro, A. Filippo and C. Luca, "What is an acceptably smoothed fluence? Dosimetric and delivery considerations for dynamic sliding window IMRT," Radiat. Oncol. **2**, 42 (2007).
122. G. S. Ibbott, D. S. Followill, H. A. Molineu, J. R. Lowenstein, P. E. Alvarez and J. E. Roll, "Challenges in credentialing institutions and participants in advanced technology multi-institutional clinical trials," Int. J. Radiat. Oncol., Biol., Phys. **71**, S71-75 (2008).
123. J. Burmeister, "Radiotherapy Treatment Errors: Of Man and Machine," in *Enterprise Imaging & Therapeutic Radiology Management*, (2009), pp. 21-22.

124. L. T. Kohn, J. Corrigan, D. M. S., I. o. Medicine and C. o. Q. o. H. C. i. America, *To Err Is Human: Building a Safer Health System*, 1 ed. (National Academies Press, Washington, D.C., 2000).
125. C. Perrow, *Normal Accidents: Living with High Risk Technologies*. (Princeton University Press, Princeton, New Jersey, 1999).
126. M. Astrahan, "Some implications of linear-quadratic-linear radiation dose-response with regard to hypofractionation," *Med. Phys.* **35**, 4161-4172 (2008).
127. A. Sovik, E. Malinen, O. S. Bruland, S. M. Bentzen and D. R. Olsen, "Optimization of tumour control probability in hypoxic tumours by radiation dose redistribution: a modelling study," *Phys. Med. Biol.* **52**, 499-513 (2007).

ABSTRACT**BEYOND THE DVH
--- SPATIAL AND BIOLOGICAL
RADIOTHERAPY TREATMENT PLANNING**

by

BO ZHAO**August 2010****Advisor:** Dr. Jay Burmeister**Co-Advisor:** Dr. Michael C. Joiner**Major:** Medical Physics**Degree:** Doctor of Philosophy

Purpose: Both spatial and biological information are necessary in order to perform true optimization of a treatment plan and for predicting clinical outcome. The goal of this work is to develop an enhanced treatment plan evaluation tool which incorporates biological parameters and retains spatial dose information.

Methods: A software system named SABER (Spatial And Biological Evaluation for Radiotherapy) is developed which provides biological plan evaluation with a novel combination of features. It incorporates hyperradiosensitivity using the induced-repair model and applies the new concept of Dose Convolution Filter (DCF) to simulate dose wash-out effects due to cell migration, bystander effect, and tissue motion during treatment. Further, the concept of Spatial DVH (sDVH) is introduced to evaluate and potentially optimize the spatial dose distribution in the target volume. Finally, generalized equivalent uniform dose is derived from both physical dose distribution (gEUD) and EQD₂ distribution (gEUD₂), and the software provides three models for calculation of Tumor

Control Probability (TCP), Normal Tissue Complication Probability (NTCP), and Complication-free TCP (P+). TCP, NTCP and P+ are provided as a function of prescribed dose and multi-variable TCP, NTCP and P+ plots are provided to illustrate the dependence upon individual parameters used to calculate these quantities.

Results: By retaining both spatial and biological information about the dose distribution, SABER is able to distinguish features of radiotherapy treatment plans not discernible using commercial systems. Plans that have similar DVHs may have different spatial and biological characteristics, and the application of novel tools such as sDVH and DCF within SABER and the choice of radiobiological models may substantially change the predicted plan metrics such as TCP and NTCP, and thus change the relative plan ranking. The voxel-by-voxel TCP model makes it feasible to incorporate spatial variations of clonogen densities, radiosensitivities, and fractionation sensitivities as those data become available.

Conclusions: The SABER software incorporates both spatial and biological information into the treatment planning process. This may significantly alter the predicted TCP and NTCP and thus the choice of treatment plan. Thus SABER can help the planner compare and choose more biologically optimal treatment plans and potentially predict treatment outcome more accurately.

AUTOBIOGRAPHICAL STATEMENT

BO ZHAO

EDUCATION

2005 - 2010	Ph.D.	Medical Physics	Wayne State University, Detroit, MI, USA
2003 - 2005	M.A.	Physics	Wayne State University, Detroit, MI, USA
1999 - 2003	B.Sc.	Applied Physics	Southeast University, Nanjing, Jiangsu, China

PROFESSIONAL ASSOCIATIONS

- 2005 - , Member, the American Association of Physicists in Medicine
- 2005 - , Member, the Great Lakes Chapter of the AAPM

AWARDS

- 2000 - 2003, Scholarship for Outstanding Students Third Prize, Southeast University
- 2006 - 2007, Rumble Fellowship, Wayne State University
- 2008, Second place, the Great Lakes Chapter - AAPM Young Investigator's Symposium
- 2008 - 2010, Graduate Student Professional Travel Award, Wayne State University

PUBLICATIONS & PRESENTATIONS

- B. Zhao**, M.C. Joiner, C.G. Orton and J. Burmeister, "SABER': A new software tool for radiotherapy treatment plan evaluation", Med. Phys., (submitted).
- B. Zhao**, M.C. Joiner, Q. Liu, A. Konski and J. Burmeister, "Technology versus Biology", (in preparation).
- B. Zhao**, J. Burmeister and Q. Liu, "Comparison of Radiotherapy Treatment Plan Dose Statistics in the TomoTherapy and Varian Eclipse Treatment Planning Systems", (in preparation)
- Y. Huang, M.C. Joiner, **B. Zhao**, Y. Liao and J. Burmeister, "Dose Convolution Filter: Incorporating Spatial Dose Information into Tissue Response Modeling", Med. Phys. 37, 1068-1074 (2010).
- S. Kumar, J. Rakowski, **B. Zhao**, M. Alkhafaji, J. Burmeister, T. Austin and M. Vlachaki "Helical tomotherapy versus stereotactic gamma knife radiosurgery in the treatment of single and multiple brain tumors: a dosimetric comparison", J Appl Clin Med. Phys., (2010) (in press).
- M. Shaikh, J. Burmeister, M.C. Joiner, S. Pandya, **B. Zhao** and Q. Liu, "Biological Effect of Different IMRT Delivery Techniques: SMLC, DMLC and Helical Tomotherapy", Med. Phys. 37, 762-771 (2010).
- B. Zhao**, M.C. Joiner, Y. Huang, Y. Liao and J. Burmeister, "Treatment plan evaluation incorporating structure radiosensitivity and a spatial Dose Convolution Filter (DCF)," presented at the 3rd Varian Research Partners Symposium, Austin, TX, Apr 28 - May 1, 2008.
- B. Zhao**, M.C. Joiner and J. Burmeister, "A new software tool for radiotherapy treatment plan evaluation incorporating radiobiological and spatial information," presented at the Great Lakes Chapter of the AAPM Young Investigators and Licensure Symposium, Brighton, MI, Nov 6, 2008.
- B. Zhao**, M.C. Joiner and J. Burmeister, "Spatial Dose-Volume Histogram (sDVH) - incorporating spatial dose information back into the DVH," presented at the 51th Annual Meeting of the AAPM, Anaheim, CA, Jul 26-30, 2009.